Scale-resolving modeling of heat and mass transfer in IC engine-relevant impinging flow configurations

Sensitized RANS-RSM-based turbulence anisotropy characterization
Zur Erlangung des akademischen Grades Doktor-Ingenieur (Dr.-Ing.)
Genehmigte Dissertation von Maximilian Christof Bopp aus Groß-Gerau
Tag der Einreichung: 23. Oktober 2023, Tag der Prüfung: 23. Januar 2024, Jahr der Veröffentlichung der Dissertation auf TUprints: 2024

Review: apl. Prof. Dr.-Ing. Suad Jakirlic
Review: Prof. Dr.-Ing. Jeanette Hussong
Review: Prof. Dr.-Ing Christian Hasse
Darmstadt, Technische Universität Darmstadt

TECHNISCHE
UNIVERSITÄT
DARMSTADT

Mechanical Engineering
Department

Scale-resolving modeling of heat and mass transfer in IC engine-relevant impinging flow configurations
Sensitized RANS-RSM-based turbulence anisotropy characterization

Accepted doctoral thesis by Maximilian Christof Bopp

Review: apl. Prof. Dr.-Ing. Suad Jakirlic
Review: Prof. Dr.-Ing. Jeanette Hussong
Review: Prof. Dr.-Ing Christian Hasse

Date of submission: 23. Oktober 2023
Date of thesis defense: 23. Januar 2024
Year of publication of the thesis on TUprints: 2024

Darmstadt, Technische Universität Darmstadt

Bitte zitieren Sie dieses Dokument als:
URN: urn:nbn:de:tuda-tuprints-273992
URL: http://tuprints.ulb.tu-darmstadt.de/27399

Dieses Dokument wird bereitgestellt von tuprints,
E-Publishing-Service der TU Darmstadt
http://tuprints.ulb.tu-darmstadt.de
tuprints@ulb.tu-darmstadt.de

With all my love and gratitude, I dedicate this doctoral thesis to my beloved parents, Monika & Peter Bopp, whose unwavering love, encouragement, and sacrifices have been the driving forces behind my pursuit of knowledge and achievement. Your boundless love and support has been my foundation, allowing me to overcome all challenges in my life. This thesis stands as a testament to your enduring belief in my abilities and your constant presence in my life. Thank you for instilling the values of diligence, determination, and perseverance in me and creating my opportunity to aim for greatness.

Erklärungen laut Promotionsordnung

§8 Abs. 1 lit. c PromO

Ich versichere hiermit, dass die elektronische Version meiner Dissertation mit der schriftlichen Version übereinstimmt.

§8 Abs. 1 lit. d PromO

Ich versichere hiermit, dass zu einem vorherigen Zeitpunkt noch keine Promotion versucht wurde. In diesem Fall sind nähere Angaben über Zeitpunkt, Hochschule, Dissertationsthema und Ergebnis dieses Versuchs mitzuteilen.

§9 Abs. 1 PromO

Ich versichere hiermit, dass die vorliegende Dissertation selbstständig und nur unter Verwendung der angegebenen Quellen verfasst wurde.

§9 Abs. 2 PromO

Die Arbeit hat bisher noch nicht zu Prüfungszwecken gedient.

Darmstadt, 23. Oktober 2023

M. Bopp

Abstract

The present work provides insights into momentum, heat and species transport phenomena occurring under highly anisotropic turbulent conditions, such as those encountered in conventional, wall-parallel channel flows, variously designed wall-perpendicular flow impingements, and complex internal combustion (IC) engine intake flow configuration.

The main focus of the present thesis is to investigate the predictive performance of a baseline second-moment closure Reynolds-Averaged Navier-Stokes Reynolds-Stress Model (RANS-RSM) and its scale-resolving extension, the Improved Instability-Sensitive Reynolds-Stress Model (IISRSM) (Jakirlić and Maduta, 2015), employed within a sensitized RANS concept in conjunction with first- and second-order modeling approaches for the turbulent heat and species flux.

A comparative assessment of the predictive performance of the two RANS-RSM related models in terms of their ability to correctly predict coupled, simultaneously occurring momentum, heat and species transport processes is performed for a turbulent channel, slot-jet impingement, axisymmetric-jet impingement, double-slot-jet impingement and IC intake flow configuration. As an important step in model development, all respective flow configurations are compared with corresponding reference Direct Numerical Simulations (DNS) and Large Eddy Simulations (LES).

To evaluate the general physical realizability of the momentum transport, the turbulence anisotropy is characterized by utilizing the invariant maps of Lumley and Newman (1977) and Choi and Lumley (2001) as well as the related barycentric map suggested by Banerjee, Krahl, Durst, and Zenger (2007). To further represent the second-order Reynolds stress anisotropy tensor field within the computational domain, a barycentric coloring approach (Emory and Iaccarino, 2014) is applied to all numerical datasets.

The modeling of the turbulent heat and species flux within the corresponding temperature and species transport equation is realized by the isotropic simple gradient diffusion (SGDH) and anisotropic modeling approaches, such as the generalized gradient diffusion (GGDH) or the higher order quadratic gradient diffusion hypothesis (HOGGDH) originally proposed by Abe and Suga (2001). The baseline RSM in combination with the considered heat flux models provided a reasonable prediction for temperature and species transfer and the corresponding distribution of some relevant integral properties, such as the Nusselt number.

The scale-resolving IISRSM provided significantly better predictions for velocity, Reynolds stress components as well as temperature and concentration profiles, closely following the respective DNS and LES references.
To accurately predict the near-wall behavior of thermal and species fields, a RANS-based model, whether in the conventional or sensitized RANS framework, must not only correctly capture the velocity field but also the underlying anisotropic Reynolds stress tensor field. Sensitizing a second-order Reynolds stress model to adequately resolve the fluctuating turbulence can significantly improve the prediction of the flow structure in terms of all dependent flow properties, such as velocity, Reynolds stress, species and thermal fields, considering that a significant fraction of the turbulent spectrum has been resolved.

Remark: Parts of the computational investigations within the present thesis are published by the author of the present work (Bopp, Wegt, Krüger, Secchi, Frohnapfel, and Jakirlić, 2024).

Zusammenfassung

Die vorliegende Arbeit liefert Einblicke in die Quantifizierung von Impuls, Wärme und Stofftransportprozessen unter stark anisotropen, turbulenten Strömungsbedingungen, wie sie sowohl in generischen Strömungskonfigurationen als auch komplexen Ansaugströmungen eines Verbrennungsmotors auftreten.
Der Schwerpunkt der vorliegenden Dissertation liegt auf der Untersuchung der Vorhersagegenauigkeit eines Reynolds-Averaged Navier-Stokes Reynolds-Spannungsmodells (RANS-RSM) und dessen skalenauflösenden Erweiterung, des Improved-Instability-Sensitive Reynolds-Spannungsmodells (IISRSM) (Jakirlić und Maduta, 2015), welches in Verbindung mit verschiedenen Modellansätzen zur Erfassung des turbulenten Wärme- und Stofftransport untersucht wird.
Eine Bewertung der Vorhersagegenauigkeit beider RANS-Reynoldsspannungsmodelle in Bezug auf ihre Fähigkeit, simultan auftretende Transportprozesse von Impuls, Wärme und Stoff korrekt vorherzusagen, wird für eine turbulente Kanalströmung, wandnormale Schachtprallströmung, achsensymmetrische Prallströmung, Doppelschachtprallströmung sowie die Ansaugströmung eines Verbrennungsmotors durchgeführt. Die Ergebnisse dieser numerischen Studien werden zur genauen Quantifizierung mit entsprechenden Referenzdaten unterschiedlicher Direkter Numerischer Simulationen (DNS) und Grobstruktursimulationen (LES) verglichen.
Um die allgemeine physikalische Realisierbarkeit des Impulstransports zu bewerten, wird die Turbulenzanisotropie anhand der Invariantenkarten von Lumley und Newman (1977) und Choi und Lumley (2001) sowie dem damit zusammenhängenden baryzentrischen Turbulenzdreieck nach Banerjee, Krahl, Durst und Zenger (2007) charakterisiert. Um den anisotropen Charakter des Reynoldsspannungs-Tensorfelds zweiter Ordnung im Rechengebiet darzustellen, wird ein baryzentrischer Färbungsansatz nach Emory und Iaccarino (2014) auf alle numerischen Datensätze angewandt. Dies liefert eine klare und verständliche Darstellung anisotroper Impulstransportprozesse. Die Modellierung des turbulenten Wärme- und Stofftransports in der entsprechenden Temperatur- und Stofftransportgleichung erfolgt sowohl durch einfache, isotrope Gradientendiffusion (SGDH) als auch anisotrope Modellierungsansätze wie die generalisierte Gradientendiffusion (GGDH) oder die Hypothese der quadratischen Gradientendiffusion höherer Ordnung (HOGGDH) nach Abe und Suga (2001). Hierbei liefert das Standard-RSM in Kombination mit den betrachteten turbulenten Flussmodellen sinnvolle Vorhersagen für die Temperatur- und Stoffübertragung sowie die

entsprechende Verteilung einiger relevanter integraler Eigenschaften wie der Nusselt-Zahl. Das skalenauflösende IISRSM liefert hierbei jedoch im Vergleich nochmals signifikant verbesserte Vorhersagen für Geschwindigkeit, Reynolds-Spannungskomponenten sowie Temperatur- und Konzentrationsprofile, welche in sehr guter Übereinstimmung mit den jeweiligen DNS- und LES-Referenzen liegen.

Zusammenfassend lässt sich erkennen, dass ein RANS-basiertes Modell, sei es im Rahmen konventioneller oder sensibilisierter RANS-Modellierungsstrategien, nicht nur das zugrunde liegende Geschwindigkeitsfeld, sondern auch den anisotropen Reynolds-Spannungstensor korrekt erfassen muss um das wandnahe Verhalten der Temperatur- und Stoffgrenzschichten genau vorherzusagen. Die Sensibilisierung eines Reynolds-Spannungsmodells zweiter Ordnung zur angemessenen Auflösung der fluktuierenden Turbulenz kann die Vorhersagegenauigkeit der Strömungsstruktur in Bezug auf alle abhängigen Strömungseigenschaften erheblich verbessern. Hierbei wird ein überwiegender Anteil der fluktuierenden Geschwindigkeits-, Reynolds-Spannungs-, Stoff- und Temperaturfelder aufgelöst, was direkt zu einer signifikaten Verbesserung der Vorhersagegenauigkeit führt.

Vermerk: Auszüge der numerischen Untersuchung sowie deren Auswertungen sind durch den Autor der vorliegenden Thesis als wissenschaftiches Paper veröffentlicht (Bopp, Wegt, Krüger, Secchi, Frohnapfel und Jakirlić, 2024).

Acknowledgement

The present work was conducted during my time as a research assistant at the Institute of Fluid Mechanics and Aerodynamics (SLA), Technical University of Darmstadt, from February 2019 to July 2023. I extend my deepest gratitude to Prof. Dr.-Ing. Jeanette Hussong and apl. Prof. Dr.-Ing. habil. Suad Jakirlić for affording me the invaluable opportunity to pursue my doctorate amidst both favorable and challenging circumstances. I extend a special thanks to my supervisor, apl. Prof. Dr.-Ing. habil. Suad Jakirlić, for providing consistent guidance and support whenever needed. I am further particularly thankful to my Post-Doc mentor, Dr.-Ing. Sebastian Wegt, whose generous assistance and dedicated efforts have been pivotal in creating this thesis. Thank you to Dr.-Ing. Louis Reitter, Dr.-Ing. Mark Gloerfeld, Dr.-Ing. Benjamin Krumbein, Dr.-Ing. Felix Gerlach, Dr.-Ing. Markus Schremb, Louis Krüger, Steffen Gröninger, and Dr.-Ing. Ivan Joksimovic, whose collaborative and encouraging work environment has significantly contributed to the success of this doctoral journey. My sincere appreciation also extends to Birgit Neuthe for her consistent support and counsel in various administrative matters.

Furthermore, I wish to express my gratitude to the Collaborative Research Center TRR 150, granted by the German Research Foundation DFG, for their financial support and to the Lichtenberg High Performance Computer of TU Darmstadt for providing the essential computational resources.

Contents

Abstract xi

Acknowledgement xi

1. Introduction 1
- 1.1. Background and motivation . . . 1
- 1.2. Objectives and outline of this thesis . . . 3

2. Theoretical background 7
- 2.1. Governing equations of continuum mechanics . . . 8
- 2.2. Reference dimensionless numbers . . . 10
- 2.3. Fundamental concepts of turbulence . . . 11
- 2.4. Reynolds-Averaged equations . . . 13
  - 2.4.1. Eddy viscosity models . . . 14
  - 2.4.2. Second moment closure (SMC) models . . . 15
  - 2.4.3. Modeling of turbulent scalar fluxes . . . 20
- 2.5. Large Eddy Simulation (LES) . . . 24
  - 2.5.1. Wall-Adapting Local Eddy-viscosity (WALE) Subgrid-Scale (SGS) model . . . 25
- 2.6. Finite-Volume Method (FVM) . . . 26
  - 2.6.1. Spatial & Temporal Discretization . . . 26

3. Characterization of turbulence anisotropy 31
- 3.1. Visualization of Turbulence Anisotropy . . . 32

4. Preliminary investigations 41
- 4.1. Turbulent channel flow with heat transfer . . . 42
- 4.2. Slot-jet impingement onto a heated wall . . . 47

5. Leading configurations 63
- 5.1. TUDa Flowbench - IC engine intake flow . . . 63
- 5.2. Axis-symmetric Impining Jet (ASIJ) . . . 79
- 5.3. Double-Slot Impinging Jet (DSIJ) . . . 94

6. Conclusions and outlook 111

Bibliography **113**

A. Appendix **121**
A.1. Reynolds stress model 121
A.2. Improved-Instability-Sensitive-Reynolds stress model 123

Nomenclature **133**

1. Introduction

1.1. Background and motivation

The flow pattern within internal combustion engines plays a critical role in the internal combustion process and therefore, has a direct impact on engine efficiency and emissions. Even in the absence of combustion or heat transfer processes, the flow within a complex piston-cylinder assembly, as a part of an internal combustion engine is significantly influenced by the interaction of various simultaneously occurring flow phenomena. The flow complexity arises from phenomena such as interacting injector jets, tumbling and swirling motion, wall shear stress variation as well as stretching and squeezing effects on the working fluid during expansion and compression modes of engine operation (Stone, 1999).An adequate description of the flow characteristics include complex flow straining caused by the collision of multiple intake jets and their subsequent impingement on the cylinder walls and piston surface, as well as multiple wall-bounded and free separation events (Ferguson and Kirkpatrick, 2015).

Furthermore, it is important to notice that the flow phenomena occurring within an internal combustion engine, such as wall-perpendicular flow impingement and the resulting convective heat and species transfer, are also critical for many other industrial applications that require correspondingly high rates of heat and species transfer (Bergman, 2011). Among further these applications include film drying (Avcı, Can, and Etemoğlu, 2001), cooling of gas turbine blades after combustion (Han, Dutta, and Ekkad, 2012) or injection processes within combustion chambers. Various parameters exert influence on these flows and their corresponding heat and species transfer rates. Prominent factors include characteristic length of nozzle-to-wall distances, Reynolds number, Prandtl number and Schmidt number. Many studies, both numerical and experimental, have delved into these parameters' effects on various wall-normal impingement processes onto flat surfaces (Martin, 1977, Jambunathan, Lai, Moss, and Button, 1992, Ho and Nosseir, 1981). Numerical investigations have particularly examined the impact of turbulence models on the accuracy of momentum, heat and species transfer predictions in wall-perpendicular flow configurations. Craft, Graham, and Launder (1993) highlighted that Reynolds-averaged turbulence models struggle to provide satisfactory results for wall-perpendicular impinging jet flows. Behnia, Parneix, Shabany, and Durbin (1999) emphasized the significance of near-wall modeling for

achieving reasonable outcomes in turbulent jet impingement scenarios. However, even simulative results obtained in conjunction with RANS models which account for near-wall turbulence do not guarantee optimal results. Many heat transfer models still fall short in accurately capturing heat and species transport across diffusive sublayers, mixing layers, and associated buffer layers (Šarić and Basara, 2018). The interplay between the turbulence model and the model for turbulent heat and species fluxes, denoted as $\overline{u\prime_j\theta\prime}$ and $\overline{u\prime_j c\prime}$ in RANS simulations, remains of great interest. Even in simpler flow configurations involving only gaseous media, studies employing near-wall turbulence models often yield Nusselt number predictions that diverge from corresponding experimental data (Chang and Shyu, 2000). Notably, a recurrent challenge in wall-perpendicular flow configurations is the substantial overestimation of turbulence kinetic energy driven by streamline curvature, as well as the resultant deviation in the turbulent Prandtl number Pr_t in vicinity to the wall. These issues are closely linked to how turbulent momentum and heat fluxes are modeled, as well as the chosen time-averaged or time-accurate framework that underpins the numerical modeling approach.

A significant limitation of the traditional eddy viscosity modeling approach, employed for closing the turbulent momentum flux $\overline{u\prime_i u\prime_j}$ in the Reynolds-averaged momentum equation, is its assumption of isotropic turbulence. This approach, originally proposed by Boussinesq (1877), employs the anisotropy–blind scalar turbulent viscosity ν_t to model additional turbulent momentum transfer:

$$\overline{u\prime_i u\prime_j} = -2\nu_\mathrm{t}\overline{S}_{ij} + \frac{2}{3}k\delta_{ij} \tag{1.1}$$

However, this isotropic assumption falls short for many turbulent flows where momentum transport exhibits pronounced anisotropy. In contrast, second-moment closure (SMC) models inherently consider the anisotropic nature of turbulent fluctuations. By solving a transport equation for the second-order moments of the Reynolds stress tensor $\overline{u\prime_i u\prime_j}$, SMC models are capable of accounting for fully-modelled i.e. unresolved turbulence anisotropy, depending on the used computational framework. In this context, the present thesis utilizes a second-moment RANS model and its sensitized, scale-resolving extension (Jakirlić and Maduta, 2015) to achieve an enhanced prediction of turbulent momentum and the subsequent heat and species transport. The corresponding model is further described in chapter 2.

For typical heat and mass transfer problems additionally to the turbulent momentum transport, a corresponding modeling of the respective turbulent heat and species transport has to be introduced. The most-widely used model formulation for the turbulent heat or species flux ($\overline{u\prime_j\theta\prime}$ or $\overline{u\prime_j c\prime}$), the so-called simple gradient diffusion approach - representing the straightforward proportionality to the mean scalar field ($\overline{C}$, $\overline{\Theta}$) gradient - is formulated in analogy to the Boussinesq

approximation:

$$-\overline{u\prime_j \theta\prime} = \Gamma_\Theta \frac{\partial \overline{\Theta}}{\partial x_j} \qquad \text{with} \qquad \Gamma_\Theta = \frac{\nu_t}{Pr_t} \tag{1.2}$$

$$-\overline{u\prime_j c\prime} = \Gamma_C \frac{\partial \overline{C}}{\partial x_j} \qquad \text{with} \qquad \Gamma_C = \frac{\nu_t}{Sc_t} \tag{1.3}$$

The eddy diffusivity $\Gamma_{\Theta,C}$ of the respective scalar field is commonly expressed in terms of the eddy viscosity ν_t and the constant turbulent Prandtl and Schmidt numbers Sc_t, Pr_t (see Combest, Ramachandran, and Dudukovic, 2011). Simple heat flux models of this type exhibit the major weakness that the scalar fluxes are directly related to the mean scalar-field gradients through a simple scalar turbulent diffusivity. These formulations are not capable of capturing turbulence anisotropy residing in modeled diffusive fluxes due to the scalar nature of the eddy viscosity. The present thesis therefor closely emphasizes the predictive capabilities and usefulness of Second-moment RANS-based closure models in a classical, time-averaged and time-accurate, scale-resolving framework in conjunction with higher order modeling approaches for the corresponding turbulent heat and species flux. Hereby the velocity and the underlying Reynolds stress components are closely investigated by utilizing various techniques for the appropriate anisotropy-related visualization of second order tensors fields.

1.2. Objectives and outline of this thesis

Jet impingement, wall-perpendicular and injection-related flows are significantly contributing to industrial processes that require high heat and species transfer rates. Factors like the characteristic length of the nozzle-to-wall distance, Reynolds, Prandtl and Schmidt numbers crucially impact these flows. Multiple studies explore wall-normal impingements on surfaces and additionally emphasize the coupled heat and species transfer (Martin, 1977, Jambunathan, Lai, Moss, and Button, 1992). Further, various numerical investigations examine the influence of the applied turbulence model and its effects on heat/species predictions for wall-perpendicular flows (Craft, Graham, and Launder, 1993). Subsequently, near-wall turbulence modeling is isolated as an important factor for enhanced predictive capabilities (Behnia, Parneix, Shabany, and Durbin, 1999), but even with it, heat and species transfer modeling tend to fall short to experimental or numerical reference data sets (Šarić and Basara, 2018). RANS models often overestimate the production of turbulence kinetic energy in wall-perpendicular flows due to intense streamline curvature. Since traditional RANS-related eddy viscosity turbulence models assume isotropic turbulence (Boussinesq, 1877), they are not capable of accounting for any modeled turbulence anisotropy. However, within the present thesis two second-moment closure (SMC) Reynolds-stress turbulence models originally suggested by Jakirlić and Maduta (2015) are applied

to address turbulence anisotropy and, in conjunction with higher order modeling approaches for the corresponding turbulent heat and species flux, improve momentum, heat and species transfer predictions.

After the previous chapter, which introduced the description of the physical complexity of the flow configurations to be investigated and illustrated the weaknesses of the existing computational models by citing relevant literature references, chapter 2 delves into the theoretical foundations of simulating heat and species transfer from a fluid mechanics perspective. The primary objective of this chapter is to provide a short overview of the fundamental equations governing fluid mechanics, with a specific emphasis on scalar heat and species transfer. The computational framework assumes an incompressible Newtonian fluid, introducing the conservation equations for momentum, energy, and species transfer essential for the numerical simulation of turbulent flows. Various modeling approaches, including time-averaged and scale-resolving Reynolds-Averaged Navier-Stokes (RANS) closure models and Large Eddy Simulation (LES) closure models, are introduced briefly, alongside corresponding concepts for closing the governing equations. The chapter concludes by addressing the practical implementation of these equations, along with the methodology for their spatial and temporal discretization utilizing the Finite Volume Method (FVM).

Chapter 3 focuses on the methodology for adequate comparative assessment of arbitrary anisotropic Reynolds stress tensor fields which is directly linked to the corresponding overall predictive capabilities of the previously introduced conventional and scale-resolving second moment closure Reynolds stress model RSM and IISRSM (Section 2.4.2 & 2.4.2). This section especially introduces analysis tools for anisotropy-reflecting closure approaches within the underlying RANS and hybrid RANS/LES models.

Chapter 4 contains important preliminary investigations on generic flow configurations, such as turbulent channel and impinging jet flows, in conjunction with passive scalar temperature transport. Further, analytical methods for quantification of anisotropic turbulent behavior are utilized for an extensive evaluation of the predictive capabilities of the steady RANS-based RSM and its scale-resolving extension IISRSM. Subsequently, the performance of the introduced models for the scalar turbulent heat flux in conjunction with both second-moment closure models is evaluated against various DNS reference data.

Chapter 5 contains the leading configurations of the present thesis. The first configuration attends the complex, highly turbulent inflow into an internal combustion engine, the so-called TUDa Flowbench (Sec. 5.1) with a bulk Reynolds number of $Re = 38000$. The second configuration (Sec. 5.2) attends an axisymmetric impinging jet onto a heated wall. The jet structure corresponds to a

fully-developed pipe flow at a diameter-based Reynolds number of $Re = 10000$ for which reference DNS data are made available by Secchi, Häber, Gatti, Schulz, Trimis, Suntz, and Frohnapfel (2022) and Secchi, Gatti, and Frohnapfel (2023). The considered round jet impinges perpendicularly on a partially heated wall located at $2D$ distance from the pipe outlet, with boundary conditions corresponding to a constant wall temperature. The third configuration (Sec. 5.3) addresses a parallel double-slot impingement onto a smooth wall at a diameter-based Reynolds number of $Re = 10000$, in conjunction with scalar species transport. The results obtained by the baseline RANS-RSM and its scale-resolving extension, known as the Improved Instability-Sensitive Reynolds-Stress Model (IISRSM) are held against an additionally performed reference Large Eddy Simulation (LES). The focus of the present leading investigations is the comparison the combined predictive performances of higher order turbulent momentum and scalar flux modeling approaches.

To make it easier to follow the predictive capabilities of the models, Appendix A provides the detailed specification of the two presently used Reynolds Stress models 'at a glance'.

The explicit contribution of the present work is reflected in the extension of the application of the turbulence models used to flows whose complexity refers to a variety of differently structured phenomena, including flows affected by strong streamline curvature, characteristic of impinging flow events and subsequent recirculation motion, thus contributing to the further development of the models. This was followed by an appropriate adaptation of the implemented numerical algorithms. The flow configurations treated include an annular jet formed inside the intake manifold of an internal combustion engine and impinging on the cylinder and piston walls, forming a tumbling vortex structure therein, as well as differently structured jets emerging from round and slotted twin nozzles and impinging perpendicularly on heated walls. In the latter case, species transport is also considered. The comparative evaluation of the results illustrates the correctly predicted instantaneous character of the flow as well as its assembly-averaged pattern. Of particular note is the highlighting of the Reynolds stress anisotropy characterization, which helps to reveal and spatially track differently structured flow regions within the studied flow configurations.

2. Theoretical background

The forthcoming chapter provides a comprehensive insight into the theoretical background of numerical simulations concerning heat and species transfer in configurations relevant to internal combustion engines (IC engines) from a fluid mechanics perspective. The objective of this chapter is to offer a focused yet informative overview of key topics, refraining from elaborate explanations while covering crucial aspects.

The discussion centers on the governing equations of fluid mechanics, tailored to the specific context of wall parallel as well as wall-normal flow configurations with relevance to IC engines. Emphasis is placed on heat and species transfer, elucidating the assumptions applicable to incompressible Newtonian fluids and introducing the conservation equations for momentum, energy, and species transfer. Important dimensionless parameters such as the Reynolds number (Re), Prandtl number (Pr), Schmidt number (Sc), and Nusselt number (Nu) are highlighted as fundamental tools for characterizing momentum and heat transfer characteristics across all considered flow configurations. Acknowledging the turbulent nature of flow fields within the considered flow configurations, the chapter outlines the essential principles of turbulence, encompassing the features of turbulent structures and their consequential influence on heat and species transfer phenomena. Diverse modeling strategies, including Reynolds-Averaged Navier-Stokes (RANS) and Large Eddy Simulation (LES), are briefly introduced and accompanied by concepts for closing the governing Reynolds-averaged or filtered equations. The chapter further addresses the practical viability of the governing equations, outlining the methodology for their spatial and temporal discretization within the Finite Volume Method (FVM). Furthermore, it offers an overall view of relevant techniques aimed at enhancing numerical precision and stabilizing the solution process of the FVM, particularly in the context of simulating heat and species transfer.

2.1. Governing equations of continuum mechanics

Fluid mechanics problems are typically addressed through a set of partial differential equations known as the Navier-Stokes equations (NSE). These equations serve as the foundation for describing the behavior of fluids that adhere to Newtonian behavior. They assume the fluid to be a continuous medium, disregarding individual molecular motion. This permits the application of calculus and mathematical methods to describe fluid behavior at a macroscopic scale.

The continuum hypothesis is central in this context, assuming that a fluid can be treated as a seamless medium with smoothly varying properties in both space x_i and time t. This assumption is valid when the dimensions of the problem greatly surpass the mean free path of fluid molecules, thereby neglecting discrete molecular behavior.

Employing the Eulerian approach, fluid motion is depicted at a fixed spatial point and instant in time. This approach employs field variables like velocity, pressure, and density, which continuously fluctuate in both space and time. The Eulerian approach sidesteps tracking individual fluid particle trajectories, focusing instead on characterizing the fluid's attributes at specific points in space and time.

By amalgamating the continuum hypothesis and the Eulerian approach, the Navier-Stokes equations offer a mathematical framework to model and computationally solve diverse fluid mechanics dilemmas. This encompasses problems ranging from basic flows in channels to more intricate scenarios involving heat and species transport. These equations hold pivotal importance in computational fluid dynamics (CFD), a potent tool used for simulating fluid flow in numerous engineering and scientific contexts (Spurk and Aksel, 1989).

The focus of the present work is solely on fluids which display incompressible and Newtonian behavior. The governing mathematical model employed to describe the transport of mass and momentum is based on the incompressible Navier-Stokes equations, expressed in tensor notation as follows:

$$\frac{\partial U_i}{\partial x_i} = 0 \tag{2.1}$$

$$\frac{\partial U_i}{\partial t} + U_j \frac{\partial U_i}{x_j} = -\frac{1}{\varrho}\frac{\partial p}{\partial x_i} + \frac{\partial}{\partial x_j}\left(\nu \frac{\partial U_i}{\partial x_j}\right) \tag{2.2}$$

Here, $p(x_i, t)$ and $U_i(x_i, t)$ denote the pressure and velocity at a specific spatial location x_i and time t. The fluid's density is represented by ρ, and its kinematic viscosity by ν.

The energy equation, representing the temporal change of internal energy in terms of temperature, is introduced as:

$$\frac{\partial \Theta}{\partial t} + U_j \frac{\partial \Theta}{\partial x_j} = \frac{\tau_{ij}}{\rho} \frac{\partial u_i}{\partial x_j} + \frac{\partial}{\partial x_j} \left(\frac{\nu}{Pr} \frac{\partial \Theta}{\partial x_j} \right) \tag{2.3}$$

Eqn. (2.3) shows the continuum mechanical equivalent of the First Law of classical thermodynamics for an incompressible, low Reynolds number flow without the consideration of radiation (Chang and Shyu, 2000). The given temperature equation describes the evolution of a scalar temperature, denoted as Θ, with respect to time t and spatial coordinates x_j, where U_j represents the velocity in Cartesian coordinates. The Prandtl number Pr describes the influence of variable fluid properties and will be explained in the following section. The left-hand side of the equation represents the temporal change and the convective transport of the temperature field, whereas the right-hand side of the equation represents the the viscous heating and diffusion of the scalar temperature. The symmetric second-order stress tensor τ_{ij} is a key parameter in the relation between a fluid and the thermodynamics of the corresponding flow as its shear components are strongly related to dissipative processes in fluids. The shear components are related to internal friction and subsequently the conversion of mechanical into internal energy. The magnitude of shear stresses and their rate of deformation determine the amount of dissipation that occurs in a fluid. Higher shear stresses or ultimately higher shear rates lead to higher dissipation, as more mechanical energy is converted into internal energy through the process of viscous dissipation. The ratio ν/Pr represents temperature diffusivity, which characterizes the strength of molecular diffusion of the underlying thermal field within a fluid.

The final transport equation introduced in this work is the general passive scalar transport equation, which governs the evolution of a scalar quantity denoted as C within a fluid flow. The scalar transport equation describes the interaction between convection and diffusion of a scalar quantity and can be expressed as:

$$\frac{\partial C}{\partial t} + U_j \frac{\partial C}{\partial x_j} = \frac{\partial}{\partial x_j} \left(\frac{\nu}{Sc} \frac{\partial C}{\partial x_j} \right) \tag{2.4}$$

The convective term on the left-hand side represents the transport of the scalar quantity C by the bulk motion of the velocity field U_j. This term captures how the scalar quantity is advected by the fluid flow, leading to changes in its concentration over time. On the right-hand side, the diffusive term accounts for molecular diffusion

processes. This term describes how the scalar quantity diffuses from regions of high concentration to regions of low concentration, following the direction of the gradient of the scalar field.

2.2. Reference dimensionless numbers

Dimensionless numbers play a crucial role in characterizing fluid flows by enabling comparisons, simplifications, and identification of universal behaviors. They provide a way to analyze and understand complex flow phenomena across different systems, regardless of their size or absolute values.

The Reynolds number (Re) is a dimensionless parameter used to describe the flow regime of a fluid. It compares the relative importance of inertial forces to viscous forces in a fluid flow. Mathematically, it is defined as:

$$\mathrm{Re} = \frac{\mathcal{U}\mathcal{L}}{\nu} \tag{2.5}$$

The Reynolds number is defined as the ratio of the product of the characteristic velocity $\mathcal{U}$ and the characteristic length $\mathcal{L}$ of the flow to the kinematic viscosity ν of the fluid. The Reynolds number is a critical parameter in fluid mechanics as it determines the type of flow that occurs in a given situation. It helps to identify whether the flow is laminar at relatively low values or turbulent at higher values.

The Prandtl number, denoted as Pr, is a dimensionless number used in fluid mechanics and heat transfer to characterize the relative importance of momentum diffusion to thermal diffusion in a fluid. Mathematically, the Prandtl number is defined as the ratio of the momentum diffusivity to the thermal diffusivity of a fluid. It is given by the following formula:

$$\mathrm{Pr} = \frac{c_p \mu}{\lambda} \tag{2.6}$$

In 2.6 the Prandtl number is expressed as the ratio of the product of specific heat at constant pressure c_p and dynamic viscosity μ to the thermal conductivity λ of a fluid. A high Prandtl number indicates that momentum diffusion is relatively slower compared to thermal diffusion, while a low Prandtl number indicates the opposite. Different fluids have different Prandtl numbers which crucially affects their behavior in terms of heat transfer in relation to the underlying fluid motion.

The Nusselt number Nu, is a dimensionless parameter characterizing the convective heat transfer from a solid surface to a fluid flowing over it. It is defined as the ratio of convective heat transfer to conductive heat transfer and can be determined by:

$$\mathrm{Nu} = \frac{\alpha\mathcal{L}}{\lambda} \tag{2.7}$$

Here, the heat transfer coefficient $\alpha(\lambda, \eta, \rho, c_p, \Theta_w/\Theta_\infty, \text{Geometry})$ describes the capability of a fluid to dissipate energy from or to a solid surface. It is a function of the material properties of the fluid, the flow condition and the geometric conditions (Stephan and Mayinger, 2013).
Utilizing Newton's law of cooling, $\dot{q} = \alpha(\Theta_w - \Theta_\infty)$ and the well known Fourier's approach for determination of the heat flux from the wall into the fluid $\dot{q}_w = -\lambda(d\Theta/dy)|_w$ the Nusselt number Nu can be rewritten as:

$$\mathrm{Nu} = -\frac{\frac{d\Theta}{dy}\big|_w \mathcal{L}}{\Theta_w - \Theta_\infty} \tag{2.8}$$

This reformulation is especially important for the numerical calculation of the Nusselt number as it is used in the present work. Since the wall and free stream temperature Θ_w and Θ_∞ as well as the corresponding temperature gradient $d\Theta/dy$ at the wall is easily obtained in computational fluid dynamics simulations, it is possible to determine the heat transfer coefficient at every position, even for complex geometries.

The Schmidt number, denoted as Sc characterizes the ratio between momentum diffusivity to mass diffusivity. It is defined as the ratio of kinematic viscosity ν to mass diffusion coefficient D and is determined by:

$$\mathrm{Sc} = \frac{\nu}{D} \tag{2.9}$$

The Schmidt number is commonly used in the study of mass transfer as well as in the analysis of species transport phenomena in fluid flows. The material dependent diffusion coefficient $D(\Theta, p)$ is a measure of how quickly a specie diffuses through a medium. It determines the rate at which a substance or specie diffuses from an area of high concentration to an area of low concentration due to random molecular motion.

2.3. Fundamental concepts of turbulence

The work of Richardson and Kolmogorov has had a profound impact on the understanding of turbulence and its fundamental mechanisms. Their contributions have laid the groundwork for the development of turbulence theories and models, which are crucial for various fields of science and engineering. Richardson's concept of the energy cascade has provided a framework for understanding how energy is transferred across different scales in turbulent flows. This cascade process is a fundamental aspect of turbulence and is responsible for the dissipation of energy into heat at small scales. Richardson's ideas have been instrumental in shaping the understanding of the dynamics of turbulent flows, and his work has influenced subsequent studies on turbulence modeling and simulation. Kolmogorov's scaling

laws, particularly the well-known Kolmogorov $-5/3$ energy spectrum power law, have provided insights into the statistical properties of turbulent flows in the inertial sub-range. These scaling laws have helped researchers develop turbulence models and characterize the behavior of turbulence in a wide range of applications. Kolmogorov's work also introduced the concept of the Kolmogorov micro-scales, which provide a way to describe the smallest eddies in a turbulent flow based on viscosity and turbulence kinetic energy.

Together, the contributions of Richardson and Kolmogorov have paved the way for the study of turbulence from both theoretical and empirical perspectives. Their insights have been essential in developing models and simulations that enable engineers and scientists to predict and analyze turbulent flows in various practical scenarios, ranging from fluid dynamics and aerodynamics to meteorology and oceanography.

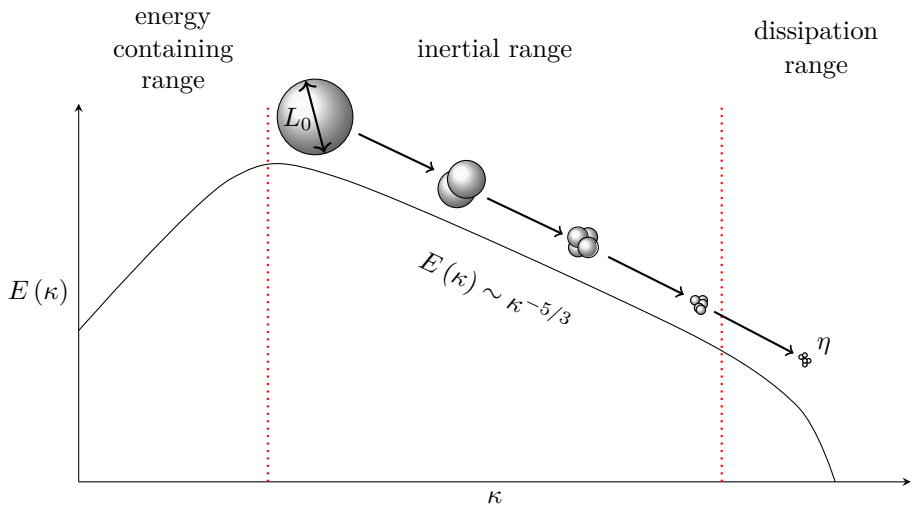

Figure 2.1.: Schematic illustration of the turbulence energy spectrum and eddy decay with the eddy energy $E(\kappa)$ plotted over the eddy wavenumber κ.

Figure 2.1 illustrates the concept of the energy cascade by displaying the energy spectrum for exemplary spherical, isotropic turbulence. The turbulent energy spectrum is displayed as the eddy containing energy $E(\kappa)$ plotted against the associated wavenumber $\kappa = 2\pi/l$. The energy spectrum is divided into three turbulent states: the energy production process or energy-containing range, the decay and energy transfer to smaller eddies or inertial subrange, and the dissipation

of the smallest eddies or dissipation range. Within the inertial range, the energy transfer can be described by a power law $E(\kappa) \sim \kappa^{-5/3}$.

According to the explanations given by Kolmogorov (1941), the tiniest dissipative eddies in a turbulent state are statistically isotropic. The smallest eddies have a universal character, and their length, velocity, and time scale can be described by the kinematic viscosity ν and the viscous dissipation ε. These properties are called the Kolmogorov scales, which include the length scale η, velocity scale u_η, and time scale τ_η of the smallest eddies and are typically given by:

$$\eta = \left(\nu^3/\varepsilon\right)^{1/4} \qquad u_\eta = (\varepsilon\nu)^{1/4} \qquad \tau_\eta = (\nu/\varepsilon)^{1/2} \tag{2.10}$$

When modeling turbulent flows different modeling strategies, which can be classified by the amount of modeled to total turbulent kinetic energy can be considered. The most widely used modeling methodologies are DNS, LES and RANS-based strategies. Within the DNS framework, the Navier-Stokes equations are solved directly without any underlying turbulence model resulting in disproportional computational costs.

Within a DNS all turbulent scales are fully resolved in space and time. It solves the full Navier-Stokes equations without any modeling assumptions. However, DNS is computationally expensive and is usually used only for generic, academic purposes or in simple geometries with low Reynolds numbers. An LES model only resolves the larger, energy-containing scales of turbulence directly and models the smaller, dissipative scales. LES is computationally less expensive than DNS and its use cases are flow configurations where the time accurate resolution of turbulent scales are important, but the computational cost of DNS is prohibitive. RANS models describe the turbulent flow in statistical manner. Since all turbulent fluctuations are modeled RANS is computationally less expensive compared to both DNS and LES and is the most commonly used modeling approach in industrial applications (Pope, 2000). For the present work, only LES and RANS modeling approaches are considered and will be described in the following section.

2.4. Reynolds-Averaged equations

The fundamental concept of Reynolds-Averaged Navier-Stokes (RANS) models is to predict the mean flow behavior of a turbulent fluid flow using time-averaged equations. Turbulent flows are characterized by chaotic and random fluctuations of their velocity and pressure fields, which make it difficult to accurately predict the flow behavior using the Navier-Stokes equations. Therefor Osborne Reynolds (1895) suggested that the turbulent fluctuations of a quantity $\Phi(x_i, t)$ can be decomposed into mean and fluctuating components.

$$\Phi_i(x_i, t) = \overline{\Phi}_i(x_i, t) + \phi\prime_i(x_i, t) \tag{2.11}$$

Applying the decomposition concept of eqn. 2.11 to the velocity $U_i(x_i,t)$, pressure $p(x_i,t)$, temperature $\Theta(x_i,t)$ and concentration $C(x_i,t)$ within the transport equations 2.1, 2.2, 2.3 & 2.4 and subsequent time-averaging results in a time-averaged set of equations for mass, momentum, energy and scalar transport:

$$\frac{\partial \overline{U}_i}{\partial x_i} = 0 \tag{2.12}$$

$$\frac{\partial \overline{U}_i}{\partial t} + \overline{U}_j \frac{\partial \overline{U}_i}{x_j} = -\frac{1}{\varrho}\frac{\partial \overline{p}}{\partial x_i} + \frac{\partial}{\partial x_j}\left(2\nu \overline{S}_{ij} - \overline{u\prime_i u\prime_j}\right) \tag{2.13}$$

$$\frac{\partial \overline{\Theta}}{\partial t} + \overline{U_j}\frac{\partial \overline{\Theta}}{\partial x_j} = \frac{\partial}{\partial x_j}\left(\frac{\nu}{Pr}\frac{\partial \overline{\Theta}}{\partial x_j} - \overline{u\prime_j \theta\prime}\right) \tag{2.14}$$

$$\frac{\partial \overline{C}}{\partial t} + U_j \frac{\partial \overline{C}}{\partial x_j} = \frac{\partial}{\partial x_j}\left(\frac{\nu}{Sc}\frac{\partial \overline{C}}{\partial x_j} - \overline{u\prime_j c\prime}\right) \tag{2.15}$$

The time-, or Reynolds-averaged momentum, temperature and species transport equations (Eqn.(2.13), (2.14), (2.15)) account for the additional correlations $\overline{u\prime_i u\prime_j}$, $\overline{u\prime_j \theta\prime}$, $\overline{u\prime_j c\prime}$ on the right-hand side of the equations which arise as a result of the time-averaging procedure. The so-called Reynolds stress tensor $\overline{u\prime_i u\prime_j}$ is a symmetrical, second order tensor which represents the momentum transfer by the fluctuating velocity field (Pope, 2000), the turbulent heat- and species flux denoted as $\overline{u\prime_j \theta\prime}$, $\overline{u\prime_j c\prime}$ represent the unresolved turbulence-related transport of the scalar temperature $\Theta(x_i,t)$ and species concentration $C(x_i,t)$. Since the set of momentum, mass, temperature and specie transport equations 2.13 contain the unknown mean pressure $\overline{p}(x_i,t)$, the three unknown velocities $\overline{U}_i(x_i,t)$, the six unknown Reynolds stress components $\overline{u\prime_i u\prime_j}$ and the three unknown heat and species flux components respectively, the resulting system is under determined and therefor not solvable without a closure approach. This famous problem is well known as the closure problem of turbulence. The following sections will address the closure problem for the momentum equation and relevant modeling strategies for its closing. The closure of the turbulent heat and species flux $\overline{u\prime_j \theta\prime}$ and $\overline{u\prime_j c\prime}$ will be further discussed in the methodology (Chapter 3).

2.4.1. Eddy viscosity models

Eddy viscosity models as a class of turbulence closure models are widely used in CFD simulations. The approach is based on the assumption that the influence of turbulent eddies can represented by a turbulent viscosity ν_t which acts as a turbulent equivalent to the molecular viscosity ν. This approach assumes that the turbulent eddies have a comparable increasing viscous effect on the fluid flow as molecular viscosity does. A widely used eddy viscosity modeling approach for the closure of the

Reynolds-averaged momentum equations (2.13) was proposed by Boussinesq (1877). The suggested approach models the additional turbulent momentum transfer by utilizing the mean strain rate tensor $S_{ij} = 0.5\left(\partial\overline{U}_i/\partial x_j + \partial\overline{U}_j/\partial x_i\right)$ in conjunction with the turbulent viscosity ν_t:

$$\overline{u\prime_i u\prime_j} = -2\nu_t \overline{S}_{ij} + \frac{2}{3}k\delta_{ij} \tag{2.16}$$

Here the Kronecker delta δ_{ij} returns the value 1 for equal and 0 for unequal indices i and j. Applying equation 2.16 to the Reynolds-averaged momentum equations, the unclosed Reynolds stress tensor $\overline{u\prime_i u\prime_j}$ with its six unknown components is reduced to just one unknown turbulent viscosity. Eddy viscosity models are simple and computationally efficient, they are ideal for large-scale simulations of turbulent flows but lack in accuracy for more specific use cases. Since the present work does not consider eddy viscosity models, the corresponding closure approaches for the turbulent viscosity ν_t will not be further illuminated.

2.4.2. Second moment closure (SMC) models

One of the most important downsides of eddy viscosity models is their assumption that the modeled turbulence is isotropic. This assumption is not accurate for many turbulent flows, where momentum transport is highly anisotropic. In contrast, second moment closure (SMC) models explicitly model the anisotropic behavior of the turbulent fluctuations by solving a transport equation for the second-order moments of the corresponding Reynolds stress tensor $\overline{u\prime_i u\prime_j}$.

The transport equation for the Reynolds stress tensor is derived by utilizing the momentum balance of the Navier-Stokes equation I_i (Eqn. (2.2)) and the momentum balance of the RANS equations $\overline{I}_i$ (Eqn. (2.13)). By inserting the momentum balance of the fluctuations $I\prime_i = I_i - \overline{I}_i$ into the expression $\overline{u_i I\prime_j} + \overline{u_j I\prime_i} = 0$ the transport equation for the Reynolds stress tensor can be derived as:

$$\begin{aligned}
\frac{\partial \overline{u\prime_i u\prime_j}}{\partial t} + \overline{U}_k \frac{\overline{u\prime_i u\prime_j}}{\partial x_k} = & \underbrace{-\overline{u\prime_i u\prime_k}\frac{\partial \overline{U}_j}{\partial x_k} - \overline{u\prime_j u\prime_k}\frac{\partial \overline{U}_i}{\partial x_k}}_{\text{production } P_{ij}} + G_{ij} + Rij + \underbrace{2\nu \overline{\frac{\partial u\prime_i}{\partial x_k}\frac{\partial u\prime_j}{\partial x_k}}}_{\text{dissipation } \epsilon_{ij}} \\
& + \underbrace{\overline{\frac{p\prime}{\varrho}\left(\frac{\partial u\prime_i}{\partial x_j} + \frac{\partial u\prime_j}{\partial x_i}\right)}}_{\text{pressure redistribution } \Phi^R_{ij}} + \underbrace{\frac{\partial}{\partial x_k}\left[\underbrace{-\overline{u\prime_i u\prime_j u\prime_k}}_{D^{u\prime}_{ij}} + \underbrace{\nu\frac{\partial \overline{u\prime_i u\prime_j}}{\partial x_k}}_{D^{\nu}_{ij}} - \underbrace{\overline{\frac{p\prime}{\varrho}\left(\delta_{ki}u\prime_j + \delta_{kj}u\prime_i\right)}}_{D^{p\prime}_{ij}}\right]}_{\text{diffusion } \mathcal{D}_{ij}}
\end{aligned} \tag{2.17}$$

The Reynolds stress production term resulting from the deformation of the mean flow field P_{ij} and the production term related to molecular diffusion D^{ν}_{ij} are exact and do not need further modeling. Since it is important for the present thesis and will be mentioned in the following, it is remarked that the production of turbulent stress due to deformation of the mean flow P_{ij} is closely linked to the mean stream line curvature of the flow field. The production terms related to fluctuating volume forces G_{ij} and to a rotating coordinate system R_{ij} are not taken into account for the further modeling in present thesis. However the transport equation of the Reynolds stress tensor also contains unclosed terms that require further modeling. The four unclosed terms are the pressure redistribution term Φ^{R}_{ij}, the dissipation rate ϵ_{ij}, the pressure diffusion $D^{p\prime}_{ij}$ and the turbulent diffusion $D^{u\prime}_{ij}$ (Pope, 2000).

Reynolds stress model (RSM)

The considered conventional, baseline Reynolds stress model to close the Reynolds-averaged momentum transport equation (Eqn. (2.13)), emerges from the collaborative efforts of Jakirlić (1997), Jakirlić and Hanjalić (2002), Jakirlić and Maduta (2015), and Maduta and Jakirlic (2017). For enhanced comprehension of the present Reynolds stress model, this section will exclusively elucidate the principal modeling approaches for each term. The comprehensive set of equations along with numerical values of relevant model constants can be found in Appendix A. In the following, the modeling of the four unclosed terms Φ^{R}_{ij}, ϵ_{ij}, $D^{p\prime}_{ij}$ and $D^{u\prime}_{ij}$ is illuminated.

The modeling of the turbulent diffusion $D^{u\prime}_{ij}$ and pressure diffusion $D^{p\prime}_{ij}$ adheres to the methodology outlined in Jakirlić (1997). Since a general understanding of the redistribution processes and their modeling is from major importance for the present thesis the modeling of the pressure redistribution term Φ_{ij} is briefly explained in the following. Modeling the redistribution process stands out as one of the most intricate challenges in formulating a Reynolds stress model. This complexity arises from both the intricate physical interpretation of this phenomenon and its strong influence within the transport equations governing Reynolds stresses. Particularly, the fluctuating pressure field plays a decisive role in the redistribution of Reynolds stress components (Jakirlić, 1997). An important detail is that redistribution processes represent only the exchange of turbulence energy among the individual stress components, reducing the differences in the energy content of individual stress components which ideally leads to a state of isotropic turbulence. This means that the process does not affect the balance of the total kinetic energy.

$$\Phi^{R}_{ij} = \Phi^{R}_{ij,1} + \Phi^{R}_{ij,2} + \Phi^{R}_{ij,3} + \Phi^{w}_{ij} \tag{2.18}$$

Since it is important for interpretation and analysis within the result section of the present thesis the respective components of the modeling approach for the redistribution term Φ^{R}_{ij} are briefly introduced in the following. The first

redistribution term $\Phi^R_{\mathrm{ij},1}$ in equation 2.18, the so-called *slow term* stands in close relation to the fluctuating velocity field and acts into the direction of isotropic turbulence. The *rapid term* $\Phi^R_{\mathrm{ij},2}$ defines the stress redistribution as a result of the fluctuating pressure field in relation to the deformation of the mean flow field. The third term $\Phi^R_{\mathrm{ij},3}$ describes the interplay between the fluctuating pressure field and volume-related influences, like gravitation, or magnetic fields. The fourth term, the so-called *wall-reflection term* takes the not yet considered influence of the wall for the *slow term* $\Phi^R_{\mathrm{ij},1}$ and *rapid term* $\Phi^R_{\mathrm{ij},2}$ into account. The *wall-reflection term* captures the phenomenon that unlike the velocity fluctuations, pressure fluctuations do not vanish in immediate wall vicinity and therefor have a significant anisotropic influence on near wall turbulence. A detailed description of related modeling strategies can be found in the work of Jakirlić (1997).

To model the individual constituents of the dissipation rate ϵ_{ij}, the approach introduced by Hanjalić and Launder (1976) is employed. This approach combines the isotropic axiatoric configuration of the dissipation rate tensor ($\epsilon_{ij} = \frac{2}{3}\epsilon\delta_{ij}$) and the low Reynolds number (Re) limit ($\epsilon_{ij} = (\overline{u\prime_i u\prime_j}/k)\,\epsilon$) of the ensuing equation:

$$\epsilon_{ij} = \epsilon \left[(1 - f_s)\,\frac{2}{3}\delta_{ij} + \frac{\overline{u\prime_i u\prime_j}}{k} f_s \right] \tag{2.19}$$

The function f_s controls the respective influence of the individual components. This shifts the modeling of the dissipation rate tensor ϵ_{ij} to the modeling of the weighting function f_s. However, the introduction of the weighting function f_s leads to erroneous values for the tensor components ϵ_{12} and ϵ_{22} of the dissipation rate tensor ϵ_{ij} in the wall region. To avoid using correction approaches, the Reynolds stress model according to Jakirlić and Hanjalić (2002) considers only the homogeneous part ϵ^h_{ij} of the entire dissipation rate tensor instead of the whole tensor. The use of the homogeneous part ϵ^h_{ij} significantly improves the near-wall behavior of the components ϵ_{12} and ϵ_{22} of the dissipation rate tensor. The derivation of the homogeneous part of the dissipation rate tensor is based on the two-point correlation transport equation according to Hanjalić and Launder (1976).

$$\epsilon^h_{ij} = \epsilon_{ij} - \frac{1}{2} D^\nu_{ij} \tag{2.20}$$

The homogeneous part of the dissipation rate tensor is composed of the difference between the entire dissipation rate tensor ϵ_{ij} and half of the viscous diffusion of the Reynolds stress tensor $D^\nu_{ij}/2$ (see Eqn. (2.20)). The approach presented in Equation (2.19) for modeling the dissipation rate tensor is transferred to the homogeneous part of the dissipation rate tensor ϵ^h_{ij} (Eq. 2.21).

$$\epsilon^h_{ij} = \epsilon^h \left[(1 - f_s)\,\frac{2}{3}\delta_{ij} + \frac{\overline{u\prime_i u\prime_j}}{k} f_s \right] \tag{2.21}$$

In Equation (2.21), the homogeneous dissipation rate ϵ^h appears, which must be determined by a transport equation. To do this, Hanjalić and Launder (1976) derived in his work the exact transport equation for the homogeneous dissipation rate ϵ^h, which is composed of the transport equation for the dissipation rate ϵ and half of the viscous diffusion of the dissipation rate D_ϵ^ν (see Eqn. (2.22)).

$$\frac{D\epsilon^h}{Dt} = \frac{D\epsilon}{Dt} - \frac{1}{2}\underbrace{\frac{\partial}{\partial x_k}\left(\nu\frac{\partial k}{\partial x_k}\right)}_{D_\epsilon^\nu} \tag{2.22}$$

The resulting transport equation for ϵ^h contains several unclosed terms again. In the work of Jakirlić and Hanjalić (2002), therefore, the transport equation for the homogeneous dissipation rate is reformulated. With the background of a model extension towards a scale-resolving turbulence model, the transport equation for the homogeneous dissipation rate ϵ^h is transformed into the transport equation for the specific homogeneous dissipation rate ω^h. Here, $\omega^h = \epsilon^h/k$ applies. The transport equation for the specific homogeneous dissipation rate can be formulated according to Equation (2.23) from the transport equation for the homogeneous dissipation rate and the turbulence kinetic energy.

$$\frac{D\omega^h}{Dt} = \frac{1}{k}\frac{D\epsilon^h}{Dt} - \frac{\epsilon^h}{k^2}\frac{Dk}{Dt} \tag{2.23}$$

Using the derived transport equation for ϵ^h according to Jakirlić and Hanjalić (2002) and the equation for determining the specific homogeneous dissipation rate (Eqn. (2.23)), the transport equation for the specific homogeneous dissipation rate ω^h is formulated (Eqn. (2.24)).

$$\begin{aligned}\frac{D\omega^h}{Dt} &= \frac{\partial}{\partial x_k}\left[\left(\frac{1}{2}\nu + \frac{\nu_t}{\sigma_\omega}\right)\frac{\partial\omega^h}{\partial x_k}\right] + C_{\omega,1}\frac{\omega^h}{k}P_k - C_{\omega,2}\left(\omega^h\right)^2 \\ &+\frac{2}{k}\left(C_{cr,1}\frac{1}{2}\nu + C_{cr,2}\frac{\nu_t}{\sigma_\omega}\right)\frac{\partial\omega^h}{\partial x_k}\frac{\partial k}{\partial x_k} + \frac{2}{k}C_{\omega,3}\nu\nu_t\frac{\partial^2 U_i}{\partial x_j\partial x_l}\frac{\partial^2 U_i}{\partial x_j\partial x_l} + S_l\end{aligned} \tag{2.24}$$

Equation (2.24) contains several unchanged terms compared to the original transport equation of the specific homogeneous dissipation rate ω^h. Furthermore, the eddy viscosity ν_t appears in the transport equation. This is represented by the formulation of Basara and Jakirlic (2003) (Eqn. ((2.25))) .

$$\nu_t = 0.144Ak^{1/2}\ \max\left[10\left(\frac{\nu^3}{k\omega^h}\right)^{1/4}, \frac{k^{1/2}}{\omega^h}\right] \tag{2.25}$$

To improve the numerical stability of the RSM, the coupling between the velocity field and the Reynolds stress tensor is extended. In this case, the Reynolds stress tensor that is used in the RANS equations is not set equal to the $\overline{u\prime_i u\prime_j}_{\mathrm{RSM}}$

calculated from the Reynolds stress transport equation, but combined with the Reynolds stress tensor calculated by the Boussinesq hypothesis of eddy viscosity (see Eqn. (2.16)).

$$\overline{u\prime_i u\prime_j} = 0.7 \quad \overline{u\prime_i u\prime_j}_{\mathrm{RSM}} + 0.3 \quad \overline{u\prime_i u\prime_j}_{\mathrm{Boussinesq}} \tag{2.26}$$

Improved Instability-Sensitive Reynolds stress model (IISRSM)

In the ensuing section, the Improved Instability-Sensitive Scale-Resolving Turbulence Model (IISRSM), as formulated by Jakirlić and Maduta (2015), is presented. The IISRSM stands as a scale-resolving turbulence model that roots itself in the framework of the Reynolds stress model (RSM), as delineated in Chapter 2.4.2, and takes shape building upon the principles of Menter and Egorov's k-ω-SST-SAS model. This extension is crafted following the methodology outlined by Jakirlić and Maduta (2015). The requisite equations and constants that encapsulate the intricacies of this turbulence model are itemized in Appendix A. The k-ω-SST-SAS model's distinguishing characteristic lies in its incorporation of an additional production term denoted as P_{SAS} within the ω-transport equation. This augmentation effectively diminishes the proportion of modeled turbulent kinetic energy. Worth noting is the redefined supplementary production term introduced by Maduta and Jakirlic, which bears semblance to the P_{SAS} term intrinsic to the k-ω-SST-SAS model.

$$\left(\frac{D\omega^h}{Dt}\right)_{\mathrm{IISRSM}} = \left(\frac{D\omega^h}{Dt}\right)_{\mathrm{RSM}} + P_{\mathrm{IISRSM}} \tag{2.27}$$

$$P_{\mathrm{IISRSM}} = 0.12 \ \max\left[1.755\kappa\left|\frac{\partial^2 \overline{u_i}}{\partial x_j^2}\right|\sqrt{k} - T_2,\ 0\right] \tag{2.28}$$

Rather than employing the von-Kármán length scale L_{vk}, the modeling of the supplementary production term P_{ISRSM} (as expressed in Eqn. (A.22)) within the ω^h transport equation (as delineated in Eqn. (2.27)) adopts the second derivative of velocity. This choice eliminates any functional reliance on the grid dimensions of the numerical scheme in the formulation of the P_{IISRSM} term (Eqn. (A.22)). This independence from the grid size stands as a marked advantage over most hybrid LES/RANS models. The P_{IISRSM} term itself engenders a localized increase of the specific, homogeneous dissipation rate ω^h. This phenomenon precipitates a reduction in the modeled component of turbulent kinetic energy, thus giving way to an augmented emphasis on turbulence resolution within this specified domain. This characteristic imparts the capacity to resolve intricate vortex structures inherent to turbulent flows.

Analogous to the RSM (Sec. 2.4.2), the coupling of the velocity field and Reynolds stress tensor is extended to improve the numerical robustness of the IISRSM, and the combination described in Eqn. (2.26) is applied (Eqn. (2.29)).

$$\overline{u\prime_i u\prime_j} = 0.7 \quad \overline{u\prime_i u\prime_j}_{\mathrm{RSM}} + 0.3 \quad \overline{u\prime_i u\prime_j}_{\mathrm{Boussinesq}} \tag{2.29}$$

It is remarked that the scale resolving character of the IISRSM results in a major improvement in the prediction of redistribution processes as both, velocity and pressure fluctuations are partially resolved.

2.4.3. Modeling of turbulent scalar fluxes

Undoubtedly, a crucial aspect in achieving accurate modeling of convective heat and species transfer lies not only in the chosen methodology for describing turbulence but also in effectively modeling the turbulence-induced heat and species flux, denoted as $\overline{u\prime_j \theta\prime}$ and $\overline{u\prime_j c\prime}$ respectively. These fluxes arise in the Reynolds-averaged scalar thermal energy and species transport equations, as introduced in equations 2.14 and 2.15. Investigating the proper modeling of these fluxes is of major importance for robust modeling of convective heat and species transfer.

In the context of Reynolds-Averaged Navier-Stokes (RANS) models applied to high molecular Prandtl number (Pr) transport scenarios, the accurate prediction of near-wall heat and species transfer remains a substantial challenge. This issue arises due to the limitations of such models in accurately capturing the intricate dynamics near walls. Successfully characterizing the pressure and velocity fields, along with a precise prediction of the modeled Reynolds stress tensor field, forms the foundational basis for correctly representing convective thermal scalar transport processes. Even numerical techniques that aim to resolve wall boundary layers and thus account for near-wall turbulence often struggle to capture heat transport accurately within the diffusive sub-layer and thermal buffer layer, as highlighted by Šarić and Basara (2018). In the context of this thesis, the modeling of thermal sub-scale fluxes $\overline{u\prime_j \theta\prime}$ is accomplished through the utilization of a RANS-RSM framework and its extended version, referred to as RSM (Section 2.4.2), and IIS-RSM (Section 2.4.2). These models, distinct from eddy viscosity-based models, have the capacity to capture unresolved anisotropic turbulent behavior. The utilization of a symmetrical second-order expression for the Reynolds stress tensor facilitates the incorporation of higher-order expressions for describing the turbulent heat flux $\overline{u\prime_j \theta\prime}$ within the temperature transport equation (Equation (2.14)). The significance of modeling turbulent heat transport in conjunction with RANS simulations is substantial. Even investigations of heat transfer in simpler flow configurations involving solely gaseous media, using near-wall turbulence models, have been observed to yield inaccurate Nusselt number predictions when compared to experimental data, as highlighted by Chang and Morris (2000). A common underlying issue appears to

be the variation of the turbulent Prandtl number Pr_t near the wall, a phenomenon that exists in reality but is often not considered. For instance, in widely used model formulations for $\overline{u\prime_j\theta\prime}$, such as the Simple Gradient Diffusion Hypothesis (SGDH), which assumes a simple proportionality to the mean temperature gradient analogous to the Boussinesq approximation, the effect of the varying turbulent Prandtl number is not accounted for. In models of this type, the scalar fluxes are directly linked to mean scalar-field gradients through a scalar turbulent diffusivity (Γ_Θ). This points to the critical need for refined modeling techniques that acknowledge the complex interplay of turbulence and scalar transport near walls, especially when dealing with high molecular Prandtl number transport scenarios.

$$-\overline{u\prime_j\theta\prime} = \Gamma_\Theta \frac{\partial \overline{\Theta}}{\partial x_j} \quad \text{with} \quad \Gamma_\Theta = \frac{\nu_t}{Pr_t} \tag{2.30}$$

Here, the eddy-diffusivity of the temperature field Γ_θ is commonly expressed in terms of the eddy viscosity ν_t and the constant turbulent Prandtl number Pr_t. The major weakness of such simple heat flux models is the scalar nature of the eddy-viscosity. Consequently, they are not capable of capturing the turbulence anisotropy, inherently residing in the diffusion fluxes. Accordingly, the proportionality coefficient Γ_Θ formulated in this way does not depend on the Reynolds stress components, whose individual energy content is selectively affected by the proximity to the wall, but on their global intensity representative expressed by the kinetic energy of the turbulence ($k = 0.5\overline{u\prime_i u\prime_i}$) providing consequently less satisfactory predictions than anisotropy-reflecting modeling strategies.

As it is well-known the models of this type, commonly applied in terms of a constant Prandtl number, result in a poor outcome in even simple flow configurations. The absence of an explicit dependence on the Reynolds stresses $\overline{u\prime_i u\prime_j}$ makes these models incapable of dealing with turbulence anisotropy, which is especially pronounced in the wall vicinity. Accordingly, the isotropic nature of the turbulent diffusivity implies obvious alignment of the turbulent scalar flux and the mean scalar gradient. This is clearly not the case in any complex flow configuration.

To address this issue a more extensive closure formulation was suggested by Daly and Harlow (1970) representing the so-called generalized gradient–transport hypothesis (GGDH) by using a second order turbulent diffusivity tensor D_{ij}:

$$-\overline{u\prime_i\theta\prime} = D_{ij} \frac{\partial \overline{\Theta}}{\partial x_j} \qquad \text{with} \qquad D_{ij} = k\tau_\theta C_\theta \frac{\overline{u\prime_i u\prime_j}}{k} \tag{2.31}$$

Within this expression C_θ and τ_θ are representing a model coefficient and the turbulent time scale respectively. As suggested in multiple works (e.g. Abe and Suga, 2001) the model coefficient C_θ is set to 0.3 and the time scale τ_θ is given by k/ϵ^h. With the consideration of the symmetric second order Reynolds Stress

tensor the above, algebraic model is anisotropy-reflecting and potentially more capable of dealing with complex flow straining when compared to the SGDH approach.

However, it is well known that the GGDH approach can also exhibit weaknesses in the overall prediction of the streamwise heat flux component $\overline{u\prime\theta\prime}$ in comparison to the wall-normal component $\overline{v\prime\theta\prime}$ (Launder, 1988). In order to sufficiently predict each component of the scalar flux, the ratio $\overline{v\prime\theta\prime}/\overline{u\prime\theta\prime}$ has to be obtained correctly. Which means, the direction of the scalar-flux vector has to be determined with sufficient accuracy.

Therefore, Abe and Suga (2001) suggested a extension to the GGDH approach which promises a more accurate prediction of the streamwise component and the overall turbulent heat flux $\overline{u\prime_i\theta\prime}$.

$$-\overline{u\prime_i\theta\prime} = k\tau_\theta\left(C_{\theta1}\frac{\overline{u\prime_i u\prime_j}}{k} + C_{\theta2}\frac{\overline{u\prime_i u\prime_k}\,\overline{u\prime_k u\prime_j}}{k^2}\right)\frac{\partial\overline{\Theta}}{\partial x_j} \tag{2.32}$$

Equation (2.32) shows the higher order generalized-gradient diffusion hypothesis (HOGGDH) approach as proposed by Abe and Suga (2001). Comparing the SGDH, GGDH and HOGGDH approaches, the higher order formulation in conjunction with a second moment closure RANS model promises to have the most accurate prediction of the streamwise heat flux component and therefor seems to be empirically suitable best for predicting complex thermal fields (Suga, 2003). For the present work, the model coefficient for the first term of Eqn. (2.32) which corresponds to the separately investigated model of Daly and Harlow (1970) is set to $C_{\theta1} = 0$. This leads to the following algebraic for the here investigated higher order GGDH model:

$$-\overline{u\prime_i\theta\prime} = k\tau_\theta C_{\theta2}\frac{\overline{u\prime_i u\prime_k}\,\overline{u\prime_k u\prime_j}}{k^2}\frac{\partial\overline{\Theta}}{\partial x_j} \tag{2.33}$$

The model coefficient for the quadratic term (Eqn. (2.33)) can be obtained from simple shear experiments and is set to $C_\theta = 0.575$. Model validation results have shown that the HOGGDH model is generally capable of improving the predictions of the standard GGDH model for a variety of turbulent heat transfer applications (Suga, Nagaoka, and Horinouchi, 2003 , Suga, 2004).

A further explicit algebraic relation for the turbulent heat flux is suggested by Younis, Speziale, and Clark (2005). In this approach the turbulent heat flux $\overline{u\prime\theta\prime}$ is constructed by utilizing various tensor quantities. The functional relationship is modelled by the following expression:

$$-\overline{u\prime_i\theta\prime} = C_1\frac{k^2}{\epsilon}\frac{\partial\overline{\Theta}}{\partial x_j} + C_2\frac{k}{\epsilon}\overline{u\prime_i u\prime_j}\frac{\partial\overline{\Theta}}{\partial x_j}$$

$$+C_3\frac{k^3}{\epsilon^2}\frac{\partial U_i}{\partial x_j}\frac{\partial\overline{\Theta}}{\partial x_j} \tag{2.34}$$

$$+C_4\frac{k^2}{\epsilon^2}\left(\overline{u\prime_i u\prime_k}\frac{\partial\overline{U_i}}{\partial x_k} + \overline{u\prime_j u\prime_k}\frac{\partial\overline{U_j}}{\partial x_k}\right)\frac{\partial\overline{\Theta}}{\partial x_j}$$

The first term in the above expression corresponds to the SGDH model in Eqn.(2.30) when the first model coefficient C_1 is set equal to $C_\mu/\mathrm{Pr_t}$. The second term corresponds to the model of Daly and Harlow (2.31). The third and fourth terms are depending from products of the velocity gradient and the Reynolds stress tensor. This combination was firstly suggested by Dakos and Gibson (1987). The

Coefficient	Value
C_1	-4.55×10^{-2}
C_2	$+3.37 \times 10^{-1}$
C_2	-3.37×10^{-3}
C_4	-2.35×10^{-2}

Table 2.1.: Model coefficients for an appropriate weighting of the contributing, respective heat fluxes, determined by Younis, Speziale, and Clark (2005) & Kaltenbach, Gerz, and Schumann (1994)

four model coefficients in table 2.1 are in reference to an LES of a basic turbulent flow in conjunction with scalar transport; The LES was performed by Kaltenbach, Gerz, and Schumann (1994) for a homogeneous shear flow with uniform scalar field gradients Younis, Speziale, and Clark (2005).

Since in the present thesis, the Reynolds-averaged energy equation 2.14 is reduced to a similar form as the Reynolds-averaged scalar transport equation 2.15 and there is no considered temperature dependency of the underlying kinematic viscosity ν and density ρ the modeling of a turbulent scalar heat and species transport ($\overline{v\prime\theta\prime} = \overline{v\prime c\prime}$) can be considered equal. The assumption to treat all considered transport phenomena as passive and scalar results in a greater set of data and the possibility to validate the scalar transport models against fields with different respective boundary conditions.

2.5. Large Eddy Simulation (LES)

Diverging from traditional Reynolds-Averaged Navier-Stokes (RANS) models, but mirroring the characteristics of sensitized RANS models, Large Eddy Simulation (LES) takes a different approach by directly resolving a large portion of turbulent motion. These non-isotropic eddies, exert a significant influence on flow dynamics, redistribution and transport processes. A thorough LES, in its classical manifestation, can be distinguished by the portion of turbulent kinetic energy attributed to the Sub-Grid Scale (SGS) model being less than 20% of the total turbulent kinetic energy, as outlined by Pope (2000).

The identification of the largest eddies entails subjecting the flow variables to a spatial low-pass filter, resulting in a partitioned representation of the variables: a filtered component denoted as $\widetilde{\Phi}_i(x_i,t)$, and a residual component $\Phi'_i(x_i,t)$ that corresponds to the Sub-Grid Scale (SGS) component. Equation (2.35) illustrates the decomposition of an arbitrary flow quantity $\Phi_i(x_i,t)$ using the filter-based approach. In this equation, the filtered components are designated by $\widetilde{(\cdot)}$, while the residual components are marked by $(\cdot)'$.

$$\Phi_i(x_i,t) = \widetilde{\Phi}_i(x_i,t) + \Phi'_i(x_i,t) \tag{2.35}$$

To establish the governing equations for the filtered flow variables, the procedure outlined in Equation (2.35) is applied to the velocity field $U_i(x_i,t)$ and pressure field $p(x_i,t)$ within the Navier-Stokes equations (Eqn. (2.1) and (2.2)). Subsequently, the resulting equations undergo spatial filtering using a filter width Δ. This sequence of steps yields the spatially filtered Navier-Stokes equations, represented as follows:

$$\frac{\partial \widetilde{U}_i}{\partial x_i} = 0 \tag{2.36}$$

$$\frac{\partial \widetilde{U}_i}{\partial t} + \frac{\partial \widetilde{U}_j(\widetilde{U}_i)}{x_j} = -\frac{1}{\varrho}\frac{\partial \widetilde{p}}{\partial x_i} + 2\nu\frac{\partial \widetilde{S}_{ij}}{\partial x_j} - \frac{\partial \tau_{\mathrm{SGS},ij}}{\partial x_j} \tag{2.37}$$

The filtered velocity and pressure fields in Eqn. (2.37) are denoted as $\widetilde{U}i(x_i,t)$ and $\widetilde{p}(x_i,t)$, respectively. The filter width Δ, also conceptualized as the representative grid spacing within the implicit filtering paradigm, is determined as the cubic root of the volume of a grid cell, i.e., $\Delta = V_{cell}^{1/3}$. The strain-rate tensor associated with the filtered velocity is defined as $\widetilde{S}_{ij} = 0.5\ (\partial\widetilde{U}_i/\partial x_j + \partial\widetilde{U}_j/\partial x_i)$. The Sub-Grid Scale (SGS) stress tensor τ_{SGS} characterizes the residual turbulent effects that remain unresolved and necessitates an appropriate closure model to account for its influence.

Analogous to the concept of turbulent viscosity, the Boussinesq correlation is utilized to model the residual stress tensor τ_{SGS}:

$$\tau_{\mathrm{SGS},ij} - \frac{1}{3}\delta_{ij}\tau_{\mathrm{SGS},kk} = -2\nu_{\mathrm{SGS}}\widetilde{S}_{ij} \tag{2.38}$$

In this present thesis, exclusively the well-established WALE model (Nicoud and Ducros, 1999) was used for the calculation of the sub-grid turbulent viscosity ν_{SGS}. A concise overview of the applied WALE model is provided in the following section. Further, the performed LES studies within the present thesis rely on the extensive preliminary work, additional modifications and findings of S. Wegt (2022).

2.5.1. Wall-Adapting Local Eddy-viscosity (WALE) Subgrid-Scale (SGS) model

The WALE SGS model as firstly introduced by Nicoud and Ducros (1999) calculates the subgrid turbulent viscosity ν_{SGS} as:

$$\nu_{\mathrm{SGS}} = (C_{\mathrm{w}}\Delta)^2 \frac{(\mathcal{S}^d_{ij}\mathcal{S}^d_{ij})^{3/2}}{(\widetilde{S}_{ij}\widetilde{S}_{ij})^{5/2} + (\mathcal{S}^d_{ij}\mathcal{S}^d_{ij})^{5/4}} \tag{2.39}$$

$$\mathcal{S}^d_{ij} = \widetilde{S}_{ik}\widetilde{S}_{kj} + \widetilde{\Omega}_{ik}\widetilde{\Omega}_{kj} - \frac{1}{3}\delta_{ij}[\widetilde{S}_{mn}\widetilde{S}_{mn} + \widetilde{\Omega}_{mn}\widetilde{\Omega}_{mn}] \tag{2.40}$$

The model involves the filtered vorticity-rate tensor $\widetilde{\Omega}_{ij} = 0.5(\partial\widetilde{U}_i/\partial x_j - \partial\widetilde{U}_j/\partial x_i)$ alongside the filtered strain-rate tensor $\widetilde{S}_{ij}$. The critical operator $(S^d_{ij}S^d_{ij})^{3/2} \sim y_w^3$ is used to achieve the desired near-wall behavior without relying on empirical damping functions. Here, S^d_{ij} (as defined in Eqn.(2.40)) refers to the traceless symmetric portion of the square of the velocity gradient tensor (Wegt, 2022).

To ensure nondimensionalization and enhance numerical stability, the operator $(S^d_{ij}S^d_{ij})^{3/2}$ is normalized by $(\widetilde{S}_{ij}\widetilde{S}_{ij})^{5/2} + (S^d_{ij}S^d_{ij})^{5/4}$. The previously introduced filter width Δ is utilized as the characteristic length scale of the SGS. As suggest by Wegt (2022) a specific value of $Cw = 0.325$ for the WALE-constant is recommended when using the OpenFOAM® code.

The SGS kinetic energy k_{SGS} and its dissipation rate ϵ_{SGS} can be calculated using the following equations:

$$k_{\mathrm{SGS}} = \frac{\nu^2_{\mathrm{SGS}}}{\Delta^2 C^2_{\mathrm{k}}} \tag{2.41}$$

$$\epsilon_{\mathrm{SGS}} = C_\varepsilon k^{3/2}_{\mathrm{SGS}}/\Delta \tag{2.42}$$

where the model constants are set to $C_k = 0.094$ and $C_\epsilon = 1.048$.

The workflow and models for all LES as well as further modifications for comprehensive investigations and grid studies used in the present work are based upon the work of Wegt (2022). Further information may be extracted from the corresponding literature.

2.6. Finite-Volume Method (FVM)

This present Chapter 2.6, is closely related to the combined explanations provided by Schäfer (2006), Ferziger, Perić, and Street (2002) and Wegt (2022). The methodology is reduced to a theoretical background indispensable for the present thesis.

When including the previously presented governing differential equations of fluid mechanics and turbulent closure (Sec. 2.1, 2.4) into the numerical framework of the Finite Volume Method, spatial and temporal discretization becomes imperative. This entails discretizing the differential equations to be applicable to the Control Volume-based flow domain. For demonstrative purposes and for the sake of simplicity, within this chapter, the spatial discretization is applied to a general stationary transport equation governing a non-specific, time-independent scalar field $\phi(x_i, t)$ (Eqn. (2.43)).

$$\frac{\partial}{\partial x_i}\left(\varrho U_i \phi - \Gamma_\Phi \frac{\partial \phi}{\partial x_i}\right) = \mathrm{f} \tag{2.43}$$

The spatial and temporal discretization process is explained using a simplified, two-dimensional grid consisting of equilateral cells with a uniform distribution and a node arrangement aligned with the cells, as shown in Fig. 2.2. The checked cell area with its corresponding node P, and its surface area δS_c and volume V is located in the center of the schematic illustration. The nodes and the midpoints of the faces around the control volume CV (node P) are labeled according to a compass with N, E, S, W and $c = n$, e, s, w. The normal vectors on the faces of the CV are denoted by $\vec{n_c}$, and the corresponding face lengths are δS_c.

2.6.1. Spatial & Temporal Discretization

The integral form of Eqn. (2.43) is derived by applying the theorem of Gauss, which leads to surface integrals being written as the sum over the surface S_c. The derived integral form of the general stationary transport equation (Eqn. (2.44))

$$\sum_{\mathrm{c}} \int_{S_\mathrm{c}} \left(\varrho U_i \phi - \Gamma_\Phi \frac{\partial \phi}{\partial x_i}\right) \vec{n}_i \ \mathrm{dS_c} = \iint_V f \ \mathrm{dV} \tag{2.44}$$

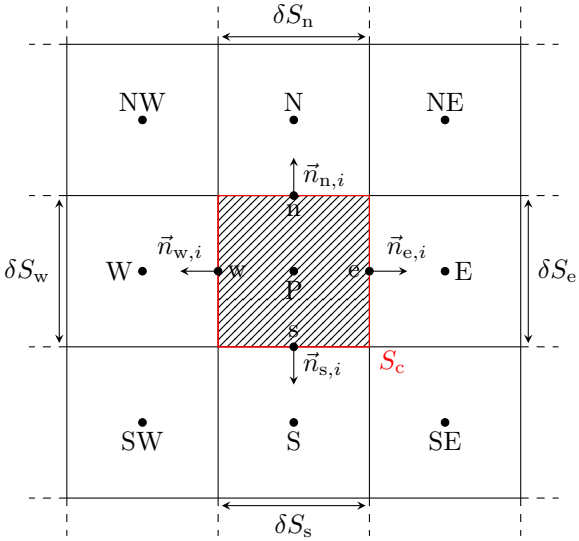

Figure 2.2.: Schematic illustration of a generic two-dimensional finite volume grid with homogeneous control volume (CV) arrangement.

encompasses surface integrals that account for the convective and diffusive fluxes across the boundaries of the control volume, in addition to volume integrals addressing the source and sink terms within the volume. Both of these components need to be numerically approximated in terms of the values at the control volume nodes, denoted as ϕ_C, to facilitate spatial discretization.

Applying the well-known midpoint rule to Eqn. (2.44) leads to the spatialy discretized form:

$$\sum_\mathrm{c} \dot{m}_\mathrm{c}\phi_\mathrm{c} - \sum_\mathrm{c} \Gamma_\Phi \vec{n}_{ci}\ \delta S_\mathrm{c} \left(\frac{\partial \phi}{\partial x_i}\right)_\mathrm{c} = \mathrm{f_P}\ \delta V, \tag{2.45}$$

Since only the node values ϕ_C are known but the corresponding cell surface values ϕ_c are needed, an explicit solution of Eqn. (2.45) can not be obtained. A solution can only be obtained by establishing a relationship between the cell center values ϕ_C and their respective surface center values ϕ_c.

Discretization of convective fluxes

The discretization of the convective fluxes is realized by approximation of the face center value ϕ_c as a function of the control volume node value ϕ_C. There are several methods for the approximation, which can be found in the corresponding literature (Schäfer, 2006), but in the following only the two most relevant are introduced.

The simplest approximation scheme is the so-called *Upwind Differencing Scheme* (UDS) which describes the face center value ϕ_c as a mass flux dependent function of the corresponding node value ϕ_C. For the simplest one dimensional transport the following relationship can be established by applying the UDS approximation:

$$\phi_\mathrm{e} \approx \phi_\mathrm{P} \ , \quad \text{if } \dot{m}_\mathrm{e} > 0 \ ; \qquad \phi_\mathrm{e} \approx \phi_\mathrm{E} \ , \quad \text{if } \dot{m}_\mathrm{e} < 0 \tag{2.46}$$

Since the functional relationship 2.46 is a very simple, explicit first order expression, a first order error can be expected. The arising error is practically impairing the accuracy of the corresponding numerical simulation as it numerically increases diffusion.
The second well-known approximation technique is the second-order *Central Differencing Scheme* (CDS). The corresponding approximation of the eastern face center value ϕ_e is presented in Eqn. (2.47).

$$\phi_\mathrm{e} \approx \gamma_\mathrm{e}\phi_\mathrm{E} + (1-\gamma_\mathrm{e})\,\phi_\mathrm{P} \tag{2.47}$$

According to Fig. 2.2 the factor $\gamma_e = (x_e - x_P)/(x_E - x_P)$ describes the absolute central difference of the surface center location x_e and the node location x_E and x_P on the x-axis.

Whereas CDS exhibits a high level of accuracy but also tends to be numerically unstable the UDS is more robust but therefor exhibits increased numerical diffusion and a subsequent loss of accuracy.

Discretized linear systems

When applying the above introduced numerical approximation approaches to Eqn. (2.45), the cell node value Φ_P is set into relation to its surrounding cell center points ϕ_N, ϕ_E, ϕ_S, ϕ_W by the following expression (2.48).

$$a_\mathrm{P}\phi_\mathrm{P} = a_\mathrm{N}\phi_\mathrm{N} + a_\mathrm{E}\phi_\mathrm{E} + a_\mathrm{S}\phi_\mathrm{S} + a_\mathrm{W}\phi_\mathrm{W} + b_\mathrm{P} \tag{2.48}$$

The corresponding prefactors a_P, a_N, a_E, a_S, a_W and b_P are hereby depend of the applied approximation method.

When extending the numerical finite volume mesh into an accumulation of $(N-1)$ CV a linear system of $\mathrm{i} = 1...N$ equations which are similar in form to Eqn. (2.48) arises. The resulting linear system for $\mathrm{c} = \mathrm{N, E, S, W}$ can be written as:

$$a_{\mathrm{P}}^{i}\phi_{\mathrm{P}}^{i} - \sum_{\mathrm{c}} a_{\mathrm{c}}^{i}\phi_{\mathrm{c}}^{i} = b_{\mathrm{P}}^{i} \tag{2.49}$$

Since the numerical procedures to determine a solution of a linear equation system is a well-known topic. More information about related techniques can be found in e.g. Hirsch (1988) or Ferziger, Perić, and Street (2002). Therefor for the sake of simplicity further explanation concerning the solution process is dispensed.

Temporal discretization

As fluid mechanical phenomena typically exhibit transient behavior, the priory stationary transport equation Eq. (2.43) is now extended into a transient transport equation described by Eq.(2.50).

$$\frac{\partial\left(\varrho\phi\right)}{\partial t} + \frac{\partial}{\partial x_i}\left(\varrho U_i\phi - \Gamma_{\Phi}\frac{\partial\phi}{\partial x_i}\right) = \mathrm{f} \tag{2.50}$$

Since the temporal derivative of $\phi(x_i, t)$ is a function of space x_i and time t the temporal discretization has to be preceded by the above spatial discretization. The subsequently now time-dependent prefactors $a_{\mathrm{P}}(t)$ have therefor also taken into account when summarizing Eqn. (2.48), which ultimately leads to the following ordinary differential equation:

$$\frac{\partial\phi_{\mathrm{P}}}{\partial t} = \frac{1}{\varrho\ \delta V}\left[-a_{\mathrm{P}}(t)\phi_{\mathrm{P}} + \sum_{\mathrm{C}} a_{\mathrm{C}}(t)\phi_{\mathrm{C}} + b_{\mathrm{P}}(t)\right] \tag{2.51}$$

When again extending the numerical finite volume mesh into an accumulation of $(N-1)$ CV a system of N, now ordinary differential equations arises. The system can be written as:

$$\frac{\partial\vec{\phi}}{\partial t} = \vec{L}(\vec{\phi}) \tag{2.52}$$

with $\vec{\phi}$ representing the sum of the N unknown functions and $\vec{L}(\vec{\phi})$ representing the right-hand side of Eqn. (2.51) (Wegt, 2022).

Relevant time discretization schemes can be subdivided in explicit and implicit methods. Hereby explicit methods only take the preceding time steps in consideration ($\phi^{n+1} = F(\phi^{n}, \phi^{n-1}, ...)$) whereas implicit methods, additionally utilize the current time step ($\phi^{n+1} = F(\phi^{n+1}, \phi^{n}, \phi^{n-1}, ...)$). Since the numerical time integration procedures are also well-known in literature more information about related techniques can be found in e.g. Hirsch (1988) or Ferziger, Perić, and Street (2002). Therefor for the sake of simplicity further explanation concerning the solution process is dispensed.

3. Characterization of turbulence anisotropy

The precise prediction of turbulence anisotropy holds significant importance in advancing reliable turbulence models within numerical fluid mechanics (Jovanovic, 2004). Within this context, accurately predicting turbulence anisotropy, particularly in Reynolds-Averaged Navier-Stokes (RANS) simulations, remains an intricate challenge. A primary hurdle in modeling turbulence anisotropy in RANS simulations pertains to the absence of precise closure models capable of predicting the complete symmetric Reynolds stress tensor $\overline{u\prime_i u\prime_j}$. Effectively analyzing turbulence anisotropy in RANS simulations is a pivotal step in formulating novel second-moment closure approaches or developing scale-resolving hybrid RANS/LES turbulence models (Banerjee, Krahl, Durst, and Zenger, 2007). Consequently, the present chapter is dedicated to outlining a methodology for a thorough comparative evaluation of the anisotropic Reynolds stress tensor. This tensor's accurate assessment is directly intertwined with the overall predictive capacities of the previously introduced steady and scale-resolving second moment closure Reynolds stress models, denoted as RSM and IISRSM respectively (Section 2.4.2 & 2.4.2).

Moving forward, the ensuing research detailed in chapters 4 and 5 encompasses the comprehensive analysis and validation of corresponding closure models associated with the Reynolds-averaged Navier-Stokes equations (2.13). This analysis leverages a combination of experimental and numerical reference data to refine and validate the proposed models.

3.1. Visualization of Turbulence Anisotropy

Within academic literature, numerous concepts have been put forth for representing turbulence anisotropy within turbulent flows. To comprehensively dissect the physical domain in which turbulent structures manifest as chaotic, three-dimensional, and transient occurrences with different length and time scales, it is from major importance to depict the inherent anisotropic behavior within a confined space that remains consistent across varying observers (Banerjee, Krahl, Durst, and Zenger, 2007). A key contribution for the analysis of turbulence anisotropy has been made by Lumley (1979) by introducing the Reynolds stress anisotropy tensor Eq. (3.1)

$$a_{ij} = \frac{\overline{u\prime_i u\prime_j}}{k} - \frac{2}{3}\delta_{ij} \tag{3.1}$$

with the turbulence kinetic energy $k = 0.5\ \overline{u\prime_i u\prime_i}$ and the Kronecker delta δ_{ij}. The anisotropy tensor a_{ij} can be utilized to quantify the anisotropic state of the underlying Reynolds stress tensor $\overline{u\prime_i u\prime_j}$. The two functional relationships given by $-\mathrm{II_a} = A_2/8 = a_{ij}a_{ji}/8$, and $\mathrm{III_a} = A_3/24 = a_{ij}a_{jk}a_{ki}/24$ can be employed to study the anisotropy of the turbulent stresses in an observer-invariant domain. Here A_2 and A_3 are the tensor invariants of the Reynolds stress anisotropy tensor a_{ij}.

The first observer-invariant domain, known as the Anisotropy-Invariant Map (AIM) (Fig. 3.1), was introduced by Lumley (1977). The AIM offers a visualization of the relationship between the two invariant-related scalars $\mathrm{II_a}$ and $\mathrm{III_a}$, associated with the Reynolds stress anisotropy tensor a_{ij}. This visualization is contained within a confined domain, confined by three defining corners: X_{c1}, X_{c2}, and X_{c3}. These corners represent the limits of one-componental (1-C), axisymmetric two-componental (2-C), and isotropic three-componental (3-C) turbulent state, respectively. The resultant boundaries of this domain, namely $[X_{c3}X_{c2}]$, $[X_{c3}X_{c1}]$, and $[X_{c2}X_{c1}]$, correspond to axisymmetric contraction and expansion, as well as the two-component limit. The AIM's significance lies in the fact that within its confines, every conceivable turbulent state is viable and thus physically accurate. This delineation of physical realizability imbues the AIM with practical utility, rendering it a straightforward and applicable theoretical tool for scrutinizing the predictive capabilities of any turbulence model. This applies across diverse flow configurations and is independent of the specific Reynolds number in question. Consequently, the analysis of functional relationships between $\mathrm{II_a}$ and $\mathrm{III_a}$ has been widely employed in diverse turbulence studies and model validations, particularly in scenarios involving shear and wall-bounded flows. Notable references for this include the works of (Jovanovic, 2004) and (Krogstad and Torbergsen, 2000).
For the present thesis, the wall-normal evolution of the turbulent stress tensor $\overline{u\prime_i u\prime_j}$ of a fully developed channel flow at a friction Reynolds number $Re_\tau = 180$, obtained by a DNS of Moser, Kim, and Mansour (1999) is used to discuss the

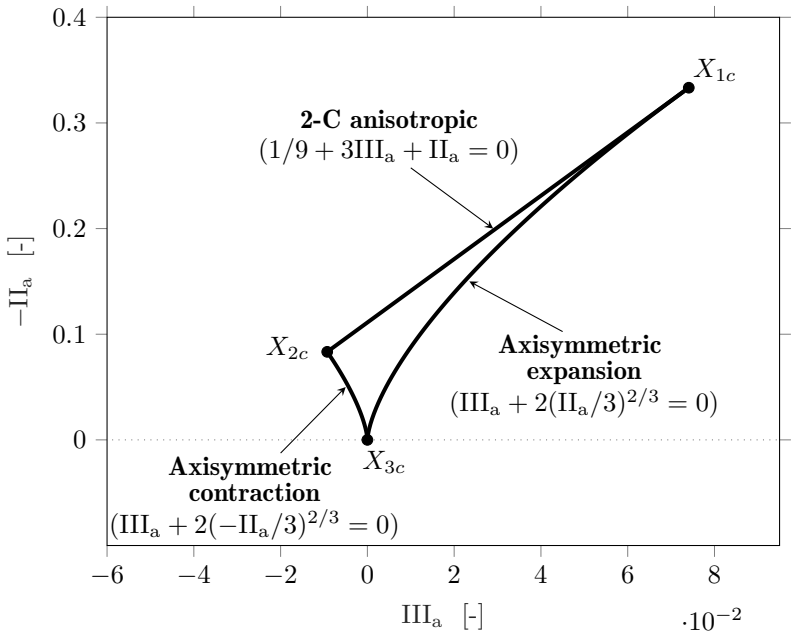

Figure 3.1.: Anisotropy-Invariant Map (AIM) for the invariant-related functional relationships $\mathrm{II_a}$ and $\mathrm{III_a}$ of the Reynolds stress anisotropy tensor a_{ij}, as proposed by Lumley and Newman (1977).

strengths and weaknesses of different visualization techniques for the Reynolds stress anisotopy tensor a_{ij}. In figure 3.2 (a) the trajectories of the invariant-related functional relationships $\mathrm{II_a}$ and $\mathrm{III_a}$ for the fully developed channel flow initiates at the two-component limit $[X_{c2}X_{c1}]$ at a corresponding dimensionless wall distance of $y^+ = 0$, marked in blue (■). After moving towards the 1-C limit X_{c1} the trajectory sharply changes direction at $y^+ = 7.67$ (■) and closely follows the axisymmetric expansion limit $[X_{c3}X_{c1}]$ until ending in vicinity to the 3-C isotropic limit X_{c3} at $y^+ = 180$ (■). It is important to notice that the trajectory seems to indicate an almost isotropic state of turbulence when approaching the channel's centerline at a dimensionless wall distance $y^+ = 180$.

In addition to the conventional AIM, an alternate depiction of the anisotropy triangle has been proposed by Choi and Lumley (2001). This approach involves transforming the second and third invariants A_2 and A_3 of the anisotropy tensor a_{ij} into new variables, namely $\xi = (\mathrm{III_a}/2)^{1/3}$ and $\eta = (\mathrm{II_a}/3)^{1/2}$. To facilitate proper visualization, corresponding definitions for boundaries and limiting states are provided in Table 3.1. Figure 3.2 b) showcases the trajectory of coordinates $\eta(\mathrm{II_a})$ and $\xi(\mathrm{III_a})$ for a fully developed channel flow at $Re_\tau = 180$, as studied by

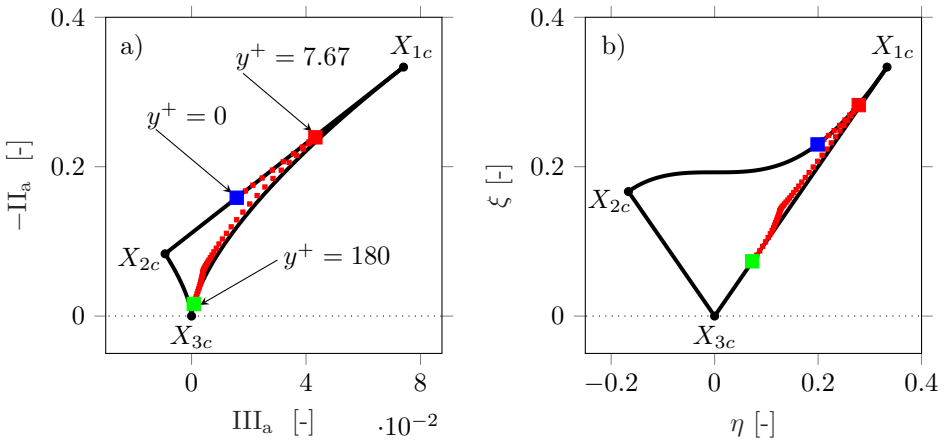

Figure 3.2.: Wall-normal evolution of the invariant tuples ($\mathrm{II_a}$, $\mathrm{III_a}$) and (ξ, η) of the Reynolds stress anisotropy tensor a_{ij} for a fully developed channel flow at a friction Reynolds number $Re_\tau = 180$, obtained by a DNS of Moser, Kim, and Mansour (1999).

Moser, Kim, and Mansour (1999). Upon visual inspection, the path $[\eta, \xi]$ within the adapted anisotropy map indicates a relatively consistent evolution across the dimensionless wall distance range of $y^+ = 0 - 180$. However, the corresponding turbulent anisotropic state at $y^+ = 180$ (■) notably diverges from the isotropic state, in contrast to what the classical AIM would suggest. Both the conventional AIM and the approach proposed by Choi exhibit inherent nonlinearities due to their boundary definitions. This complexity renders it challenging to definitively determine a superior analytical methodology.

A further technique to visualize turbulence anisotropy in a bounded domain, also suggested by Lumley (1979), can be directly derived utilizing the functional relationship between the second and third invariant $\mathrm{A_2}$, $\mathrm{A_3}$ and the eigenvalues λ_1 and λ_2 of the anisotropy tensor a_{ij}. The functional relationship between the invariants $\mathrm{A_2}$ & $\mathrm{A_3}$ and eigenvalues λ_i, of a_{ij} can be written as $\mathrm{A_2} = 2(\lambda_1^2 + \lambda_1\lambda_2 + \lambda_2^2)$ and $\mathrm{A_3} = -3\lambda_1\lambda_2(\lambda_1 + \lambda_2)$. Since the Reynolds stress tensor $\overline{u\prime_i u\prime_j}$ and its anisotropy tensor a_{ij} are symmetric second-order tensors ($\overline{u\prime_i u\prime_j} = \overline{u\prime_j u\prime_i}$, $a_{ij} = a_{ji}$) their eigenvalues are exclusively real and they can therefor be displayed in a two-dimensional domain. The boundary-defining definition and the respective limiting states for visualization of the domain are given in table 3.1.

The resulting eigenvalue map with the corresponding eigenvalue trajectory $[\lambda_2\lambda_1]$ for the turbulent channel flow of Moser, Kim, and Mansour (1999) is shown in figure 3.3 (a). Since the boundaries of the present eigenvalue map

Table 3.1.: Limiting states and boundaries of the η, ξ- and eigenvalue-related turbulence anisotropy map, suggested by Lumley (1979).

Turbulent state	**Eigenvalues**	**Invariants**
1-C limit	$\lambda_1 = 2/3,\ \lambda_2 = -1/3$	$\xi = 1/3,\ \eta = 1/3$
2-C axisym. limit	$\lambda_1 = \lambda_2 = 1/6$	$\xi = -1/6,\ \eta = 1/6$
3-C isotropic limit	$\lambda_1 = \lambda_2 = 0$	$\xi = \eta = 0$
Axisym. expansion	$\lambda_1 = (3\lvert\lambda_2\rvert - \lambda_2)/2$	$\eta = \xi$
Axissym. contraction	$\lambda_1 = (3\lvert\lambda_2\rvert - \lambda_2)/2$	$\eta = -\xi$
2-C limit	$\lambda_1 = 1/3 - \lambda_2$	$\eta = (1/27 + 2\xi^3)^{1/2}$

are exclusively linear the analysis of anisotropic behavior is simplified due to no hidden non-linearities within the trajectories between the limiting turbulent states, the interpretation can be considered as simplified when compared to the $\mathrm{II_a}$,$\mathrm{III_a}$- & η, ξ-related anisotropy maps. However, since all three introduced anisotropy maps show slightly different interpretations of anisotropic states for the considered turbulent channel flow there is still no definite superior methodology for visualization of turbulence anisotropy.

A major downside of the discussed anisotropy triangles (Fig. 3.2 a), b) & Fig. 3.3 a) is their incapability of defining a unique combination of all three turbulent states. To solve this problem Banerjee, Krahl, Durst, and Zenger (2007) suggested the utilization of a barycentric map within an euclidian domain, constructed between the three limiting states at $X_{c1} = (1, 0)$ for 1-C, $X_{c2} = (0, 0)$ for 2-C and $X_{c3} = (1/2, \sqrt{3}/2)$ for isotropic 3-C turbulence. The coordinates of the corner points, representing the limiting turbulent states, are chosen in way that the domain is defined through an equilateral triangle. This permits an equalized weighting of all three limiting states which furthermore exactly defines their linear combination. The barycentric coordinates within the equilateral triangle which are each assigned to a certain unique anisotropic turbulent state are defined as:

$$x_B = C_{1c}x_{1c} + C_{2c}x_{2c} + C_{3c}x_{3c} \tag{3.2}$$

$$y_B = C_{1c}y_{1c} + C_{2c}y_{2c} + C_{3c}y_{3c} \tag{3.3}$$

The corresponding weights

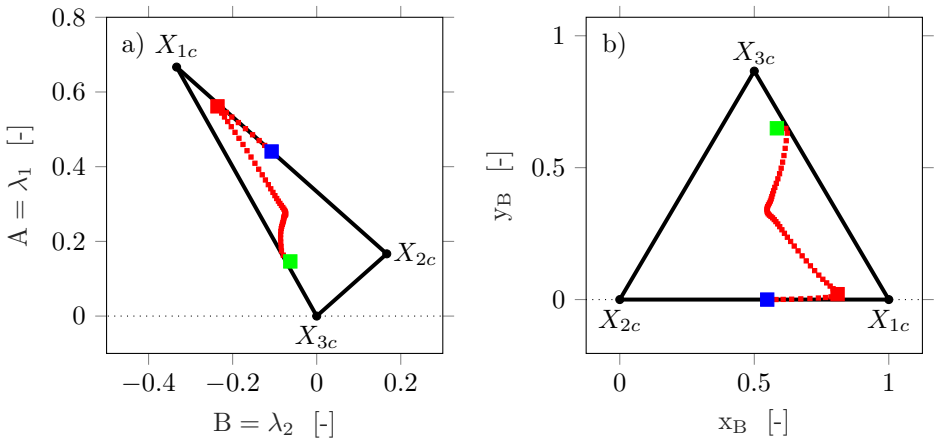

Figure 3.3.: Wall-normal evolution of the eigenvalue (λ_1, λ_2) and barycentric tuples (x_B, y_B) of the Reynolds stress anisotopy tensor a_{ij} for a fully developed channel flow at a friction Reynolds number $Re_\tau = 180$, obtained by a DNS of Moser, Kim, and Mansour (1999).

$$C_{1c} = \lambda_1 - \lambda_2 \tag{3.4}$$

$$C_{2c} = 2(\lambda_2 - \lambda_3) \tag{3.5}$$

$$C_{3c} = 2(3\lambda_3 + 1) \tag{3.6}$$

posses an important characteristic, as their sum is constrained to be $C_{ic} = 1$. This feature ensures a unique correlation between a turbulent state and its assigned barycentric tuple $(x_B(\lambda_i), y_B(\lambda_i))$. Figure 3.3 b) shows the trajectory of $[x_B y_B]$ for the turbulent channel flow by Moser, Kim, and Mansour (1999) within the barycentric anisotropy map. As all other trajectories within the shown anisotropy maps the evolution within the barycentric map initiates at the two-component limit and evolve towards the 1-C limit. The most present difference between all representations then occurs when approaching the 3-C limit, delivering a crucial deviation in isotropic behaviour, as firstly noted by Banerjee, Krahl, Durst, and Zenger (2007). The qualitative strength of the barycentric map is to linearly and clearly define the states of componentality as it delivers unique correlation between all three turbulent states at any point, which has been proven usefully in turbulence analysis. However Emory and Iaccarino (2014) noted that there are two notable drawbacks when analyzing turbulent flows utilizing the present barycentric map. The mentioned drawbacks are the loss of physical context as well as the difficulty to display large amounts of data. As visualized in figure 3.3 (b) the trajectory of the barycentric coordinates $(x_B(\lambda_i), y_B(\lambda_i))$ are only

depending on the eigenvalues λ_i of the anisotropy tensor a_{ij} and do not hold any information about the corresponding coordinates x_i within the original physical domain they are linked to. In the present case of a generic channel flow the information about the dimensionless wall distances y^+ have to be added via an additional colorbar or particular marks within the figures as it is realized in fig. 3.2 (a). Further, the simultaneous analysis of multiple data fields for more complex turbulent flow fields is furthermore impaired as anisotropic states of a_{ij} at different points x_i within the physical domain can deliver the same barycentric coordinates $(x_B(\lambda_i), y_B(\lambda_i))$. Even for two-dimensional slices of generic flow configuration the clustering of certain turbulent states within the barycentric map can prevent a clear interpretation of its trajectories. Therefore, for the analysis of larger more complex flow configurations it is necessary to identify few important subsets of points along a specific streamlines or a predefined arbitrary trajectories.

To resolve the problem of displaying large amounts of data Emory and Iaccarino (2014) introduced a new visualization technique to transfer componentality information to the physical domain by constructing a color map from the barycentric coordinates to assign every calculated componentality state of a_{ij} to a certain colour and then back to the original physical domain. Utilizing this technique, any two dimensional slice of an arbitrary flow configuration can be displayed without loosing spatial information. Emory and Iaccarino (2014) suggest using the coefficients C_{ic} of the barycentric map (Eq. 3.6) to implement a color-mixing scheme of the three base colors red $[1\ 0\ 0]^T$, green $[0\ 1\ 0]^T$ and blue $[0\ 0\ 1]^T$. Since the sum of all weights C_{ic} is constrained to be one, the linear combination

$$\begin{bmatrix} R \\ G \\ B \end{bmatrix} = C_{1c} \begin{bmatrix} 1 \\ 0 \\ 0 \end{bmatrix} + C_{2c} \begin{bmatrix} 0 \\ 1 \\ 0 \end{bmatrix} + C_{3c} \begin{bmatrix} 0 \\ 0 \\ 1 \end{bmatrix} \tag{3.7}$$

of these three base colors weighted by the barycentric weights C_{ic} can be used to construct colors in form of RGB triplets which then uniquely define the underlying anisotropic states of turbulence.

As represented by the barycentric weights, the linear combination assigns one-componental turbulence to the vector $[1\ 0\ 0]^T$ (red), two-componental turbulence to the vector $[0\ 1\ 0]^T$ (green) and isotropic turbulence to the vector $[0\ 0\ 1]^T$ (blue). All possible RGB triplets within the barycentric map are then linear combinations of these base colors. Figure 3.4 (left) shows the barycentric color map for the standard RGB colors with X_{c1} (red) representing the 1-C limit, X_{c2} (green) representing the 2-C axisymmetric limit and X_{c3} (blue) representing the isotropic,

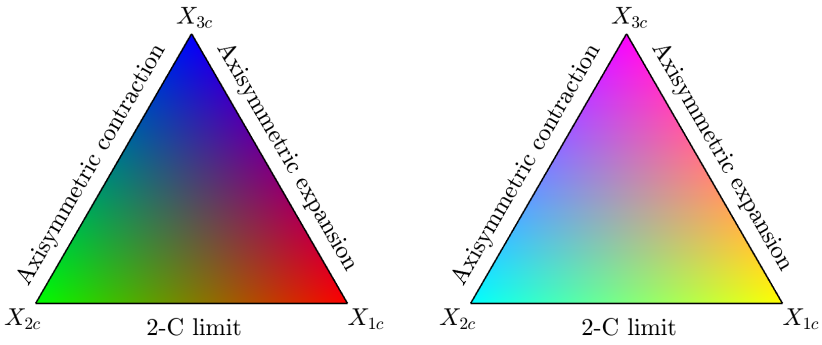

Figure 3.4.: Barycentric color map for the standard Red-Green-Blue (RGB) color model (left) and for the adapted Cyan-Magenta-Yellow-Black (CMYK) color model (right).

3-C limit. In the present thesis, a further subtractive color mixing scheme with the three base colors cyan $[0\ 1\ 1]^T$, magenta $[1\ 0\ 1]^T$ and yellow $[1\ 1\ 0]^T$ known as CMYK (Cyan Magenta Yellow Black) color model is introduced. With brighter base colors and more distinguishable mixing behaviour the adapted CMYK color model delivers an improved interpretation of anisotropic behavior further away from the corners. The newly introduced CMYK coloring model is displayed in Fig. 3.4 (right) and later applied in the subsequent analysis of various flow configurations.

While the present standard RGB-related barycentric color map defined by Eq. 3.7 is capable of conveniently categorizing turbulent anisotropy in vicinity to its corners X_{ci}, the resulting gradients within the center and near the edges of the domain are more difficult to interpret. In order to properly grade the mixing regime Emory and Iaccarino (2014) further suggested a adapted formulation for the construction of the RGB channel triplets.

Modifying the barycentric weights in equation 3.7 into $C^*_{ic} = (C_{ic} + C_{off})^{C_{exp}}$ by adding an offset C_{off} and exponential coefficient C_{exp} to them, enables the possibility of a proper adjustment of the barycentric color mixing. The modification of C_{off} allows the manipulation of the transition layer thickness between all three limiting states, whereas the smoothness of the color transition is controlled by the exponential coefficient C_{exp}. Figure 3.5 shows the modified RGB color map for $C_{off} = 0.65$ and $C_{exp} = 5$ as well as a modified version of the CYMK colormap

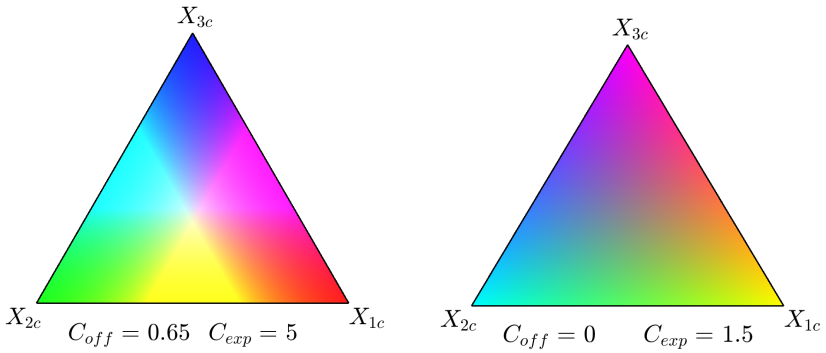

Figure 3.5.: Barycentric color map for the adjusted RGB (left) and CMYK color model (right) with modified barycentric weights $C^*_{ic} = (C_{ic}+C_{off})^{C_{exp}}$.

with $C_{off} = 0$ and $C_{exp} = 1.5$. Due to it's clearly distinguishable color mixing and proper saturation the adjusted RGB colormap, displayed in Fig. 3.5 (left) will be utilized in the subsequent anisotropy study of shear and wall-normal flows.

4. Preliminary investigations

The upcoming chapter encompasses significant preliminary investigations involving fundamental flow configurations, such as turbulent channel and impinging jet flows, coupled with passive scalar temperature transport. Furthermore, analytical techniques designed to quantify anisotropic turbulent characteristics are employed to extensively assess the predictive capabilities of the RANS-based RSM and its scale-resolving extension, IISRSM. Subsequent to these evaluations, the performance of the introduced models for scalar turbulent heat flux, in conjunction with both the second-moment closure models, is held against diverse DNS reference data sets. This extensive analysis serves to validate the models and provides insights into their efficacy for capturing the complex interplay of turbulence and scalar transport. Parts of the computational investigations within the present thesis are published by the author (Bopp, Wegt, Krüger, Secchi, Frohnapfel, and Jakirlić, 2024).

4.1. Turbulent channel flow with heat transfer

Case setup and computational domain

The first preliminary flow configurations considered is a fully-developed turbulent channel flow subjected to wall heating at a bulk Reynolds number of $Re_{2h} = 6490$ (corresponding to the friction velocity-based Reynolds number of $Re_\tau = 180$) for which the reference DNS database is available from Horiuti (1992) and Kasagi, Tomita, and Kuroda (1992).

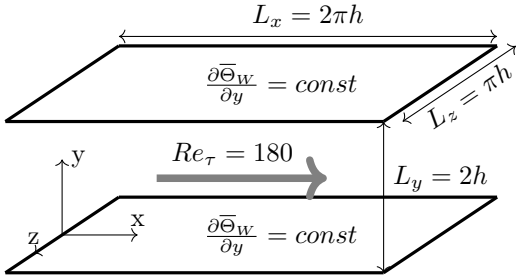

Figure 4.1.: Schematic representation of the solution domain considered for the fully-developed channel flow at a friction Reynolds number of $\mathrm{Re}_\tau = 180$.

Figure 4.1 schematically shows the typical regular hexahedron shape, bounded by lower and upper walls, and the dimensions of the computational domain of the considered turbulent channel flow, as well as the defined reference system. The dimensions of the three-dimensional solution domain adopted for the Sensitized RANS simulations with the IISRSM correspond to $L_x \times L_y \times L_z = 2\pi h \times 2h \times \pi h$, where h represents half the channel height. The corresponding numerical mesh consists of $N_x \times N_y \times N_z = 60 \times 64 \times 32$ cells, resulting in a total of 122880 cells. The height of the near-wall grid cell is $\Delta y^+ \approx 0.9$. The resolution of the uniformly distributed grid cells in the streamwise and spanwise directions corresponds to $\Delta x^+ = 19.0$ and $\Delta z^+ = 18.0$, respectively. The conventional RANS calculations are performed in a two-dimensional flow domain ($L_x \times L_y = 2\pi h \times 2h$) consisting of $N_x \times N_y = 60 \times 64$ cells. The fully-developed flow conditions are provided by applying periodic inlet-outlet boundary conditions. The no-slip boundary condition for the velocity field were set on all walls. An isoflux boundary condition with negative (directed away from the wall) gradient is applied to the upper and lower walls, implying that the time-averaged wall heat flux does not change in the flow direction. The overall thermodynamic equilibrium within the flow is characterized by the heat flux being continuously removed from the flow domain through the walls at a constant rate, resulting in a constant temperature value at both walls.

This thermal boundary condition leads to a linearly increasing mean and wall temperature $\overline{\Theta}_m$ and $\overline{\Theta}_w$ in x-direction as well as a wall temperature gradient $\partial\overline{\Theta}_w/\partial x = \text{const}$.

Results and Discussion

The following section addresses a preliminary, comparative assessment of the modeling strategies for the scalar, turbulent heat flux $\overline{u_i'\theta'}$ introduced in chapter 2.4.3 in conjunction with the RANS-RSM (Sec 2.4.2) and IISRSM (Sec. 2.4.2). To get a first impression about the basic structural characteristics of the discussed flow cases, Figures 4.2 visualize the instantaneous velocity and temperature fields.

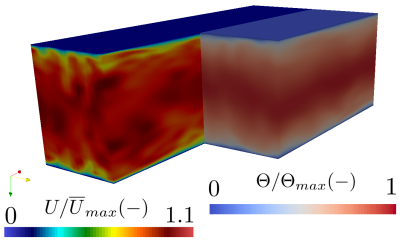

Figure 4.2.: Instantaneous velocity and temperature fields in a fully developed turbulent channel flow at a friction Reynolds number $\mathrm{Re}_\tau = 180$ with fixed iso-flux temperature boundary condition, obtained by the scale resolving IISRSM.

The results presented illustrate clearly the scale resolving capability of the IISRSM to resolve the turbulent fluctuations with respect to both velocity- and temperature fields. Their dynamics are mainly governed by their resolved fractions, whose generation is driven by the convective terms in the corresponding transport equations. However, in vicinity of the wall, the sub-scale turbulent momentum and heat fluxes are appropriately enhanced and are therefore crucial for the correct capturing of the near-wall effects. In the following individual sections, some time-averaged mean flow and turbulence characteristics are discussed along with the DNS reference results.

Figure 4.3 displays the semi-logarithmic plots of the mean velocity over the channel cross-section (left), and the profiles of all four non-zero Reynolds stress components (right) - normalized by the viscosity-scaled wall units - $U^+ = U/U_\tau$, $\overline{u_iu_j}^+ = \overline{u_iu_j}/U_\tau$ and $y^+ = y/(\nu/U_\tau)$ with the friction velocity $U_\tau = \sqrt{\nu(\partial U/\partial y)_w}$, obtained by the RANS-RSM and IISRSM. Apart from a slight under-prediction of the peak value of the streamwise stress component $\overline{u^2}^+$, the both RSM-related

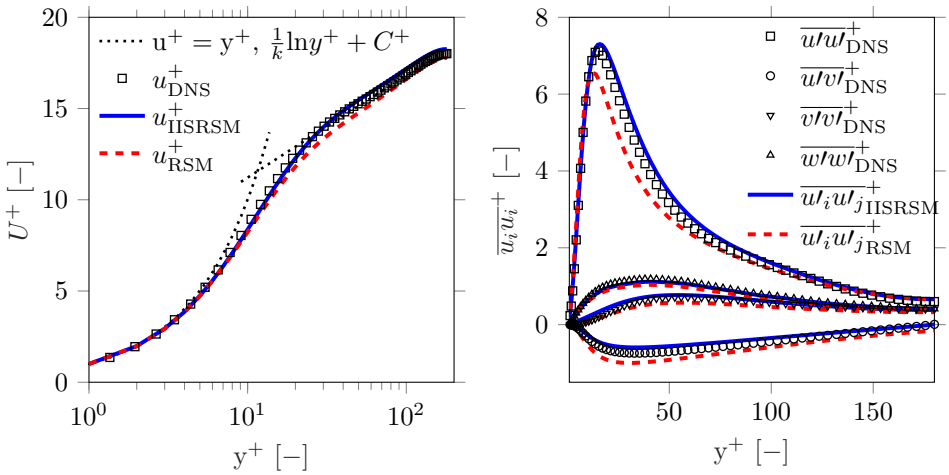

Figure 4.3.: Mean velocity (left) and Reynolds-stress component profiles (right) of the fully-developed channel flow of Horiuti (1992) and Kasagi, Tomita, and Kuroda (1992).

result sets show very good agreement with the DNS database in all characteristic boundary layer zones, viscous sublayer, buffer zone and the logarithmic region. Considering a passive character of the temperature field, there is no relevant influence on the mean velocity and turbulence field due to changes in the kinematic viscosity ν or density ρ. Accordingly, the use of different heat flux models does not influence the momentum transport and is therefore not illustrated.

Utilizing the nonlinear $\xi\eta$-based anisotropy map, introduced in chapter 3.1 for the visualization of the Invariants of the Reynolds-stress anisotropy tensor a_{ij} obtained by the RSM and IISRSM and comparing it to the reference DNS data of Kasagi, Tomita, and Kuroda (1992), three respective trajectories can be displayed in figure 4.4. The trajectory of the DNS-related reference tuples (η_{DNS}, ξ_{DNS}) starts at $y^+ = 0$ (■) at the two-component limit and ends at $y^+ = 180$ (■) in vicinity to the 3-C limit at X_{c3}. The trajectories of both RANS-based models show slight deviations when compared to the DNS data. Since the trajectories within the $\xi\eta$-based anisotropy invariant map can not clearly be differentiated, and properly compared to each other due to possible hidden non-linearities the previously, in chapter 3.1 introduced barycentric map is subsequently utilized for further analysis. Figure 4.4 (right) shows the anisotropy trajectories (x_B, y_B) of the DNS, RSM and IISRSM within the barycentric map. The trajectories displayed in the barycentric map exhibit a more notable deviation of the RANS-based results in comparison to the reference DNS data, clearly pointing out the analytical

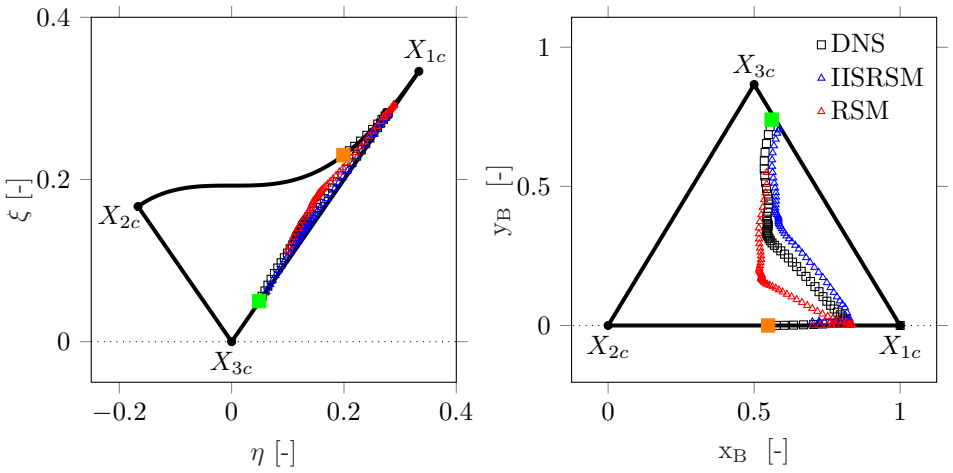

Figure 4.4.: Turbulent anisotropy trajectories calculated form the Reynolds-stress tensor fields of the IISRSM (△), RSM (△) and reference DNS (□) of Horiuti (1992) and Kasagi, Tomita, and Kuroda (1992), displayed in a nonlinear $\xi\eta$-based anisotropy invariant map (left) and a corresponding barycentric map (right).

advantages of linear anisotropy maps. It is worth mentioning that, however the Reynolds-stress components $\overline{u_i u_j}$ of both RANS models, displayed in figure 4.3 (right), are in good agreement with the DNS data, the derived anisotropic state can differ significantly. Since the turbulent anisotropy tensor a_{ij} is a rather sensitive measure for the predictive capability of the underlying turbulence models it is further utilized for model analysis within the present thesis.

When further investigate the passive, scalar temperature transport upon the previously analyzed flow field, good agreement with the DNS reference obtained by Kasagi, Tomita, and Kuroda (1992) & Horiuti (1992) is reported for the mean temperature profile across the half channel height, Fig. 4.5. Here, the mean temperature $\overline{\Theta}$ is normalized by the friction temperature $\Theta_\tau = q_w/(\rho C_p U_\tau)$. The influence of the different heat flux models SGDH (Eq. 2.30), GGDH (Eq. 2.31) and HOGGDH (Eq. 2.32), as well as of the Bassam and Speziale model (BS, Eq. 2.34), when applied in conjunction with the scale-resolving IISRSM, on the temperature profile evolution is not noticeable. All heat-flux model expressions result in the same temperature evolution over the channel domain, differing only by a maximum of 0.2%. This result was to be expected for the IISRSM application anyway, since the correspondingly high fraction of resolved turbulence leads to a dominant thermal energy transport originating from the convective term in the

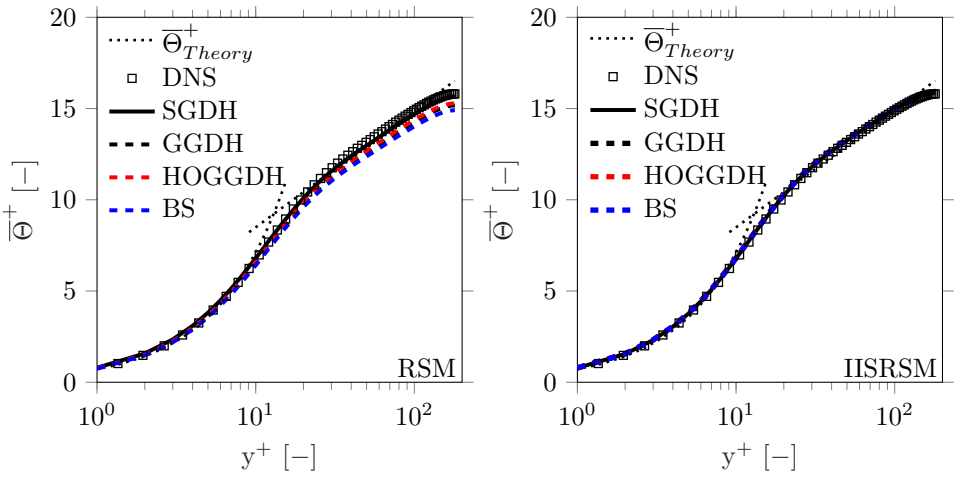

Figure 4.5.: Comparison of the dimensionless mean temperature profiles $\overline{\Theta}^+$ across the half channel height for the RSM (left), IISRSM(right) against the DNS of Horiuti (1992) and Kasagi, Tomita, and Kuroda (1992) and the theoretical temperature evolution $\overline{\Theta}^+_{Theory} = Pry^+$, $2.78\ln y^+ + C^+_\theta$.

temperature equation (2.14). In this case, the modeled turbulent heat flux $\overline{u\prime_i\theta\prime}$ relates only to the residual subscale motion contained in the diffusive term of the temperature transport equation under consideration. The results of the baseline RANS-RSM agree well with the DNS data, as does its scale-resolving counterpart. However, the steady RANS predictions for the temperature evolution over the channel deviate somewhat more, by a maximum of 3.8%. Considering that even in this case all heat flux formulations were applied in conjunction with a full differential Reynolds stress RANS model, this still satisfactory result is not very surprising. As shown in Fig. 4.3, the model is capable to correctly predict the mean velocity and the redistribution among the Reynolds stress components, which are directly incorporated into the algebraic expressions of the heat-flux models. In addition, all model coefficients for the calculation of turbulent heat-flux were previously calibrated with respect to wall-bounded channel-relevant generic flows subjected to mean shear, as mentioned in section 2.4.3. In conclusion, all adopted model formulations for the $\overline{u\prime_i\theta\prime}$ correlation led to a comparable mutual result between the two RANS-based models considered for turbulent plane channel flow with heat transfer. The further investigation within the present thesis will now focus on more complex flow configuration in conjunction with heat and species transfer.

4.2. Slot-jet impingement onto a heated wall

The next, more complex benchmark flow configuration investigated in the present Thesis is a slot-jet impingement onto a flat heated wall. The planar T-shaped flow geometry consists of an iso-thermal channel flow that vertically discharges into a horizontal channel and impinges on the opposite heated bottom wall, Figure 4.6. The simulation domain and boundary conditions for this case are set in accordance with the DNS study by Hattori and Nagano (2004). The reference DNS addresses three configurations with different distances between the heated bottom wall and the opposite adiabatic confinement wall. All simulations are performed under inflow conditions corresponding to an effective Reynolds number of $\mathrm{Re_b} = \mathrm{U_b D}/\nu = 4560$, where $\mathrm{U_b}$ represents the inflow velocity, and a molecular Prandtl number of $Pr = 0.71$. It is recalled that the DNS-related Reynolds number corresponding to $\mathrm{Re_{2D}} = 9120$ is based on the hydraulic diameter of the three dimensional inflow duct equal to $2D$.

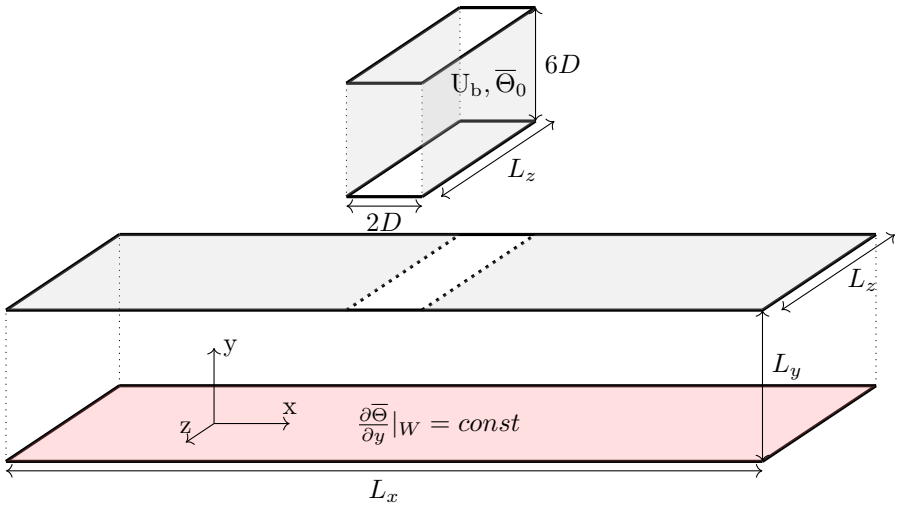

Figure 4.6.: Schematic representation of the solution domain for the slot-jet impingement configuration with an inflow Reynolds number of $\mathrm{Re_b} = 10000$ and a heated bottom wall according to Hattori and Nagano (2004).

The fully-developed channel flow exiting into the impingement domain is realized by a separate precursor computation of a channel segment using a periodic inlet/outlet condition. The flow field thus generated is subsequently mapped to the main inlet at the upper boundary of the horizontal channel. The boundary condition for the velocity field at all walls is set to no-slip. A constant heat-flux $\partial\overline{\Theta}/\partial y = q/\lambda$ is applied to the bottom wall at the impingement surface. An adiabatic wall temperature condition is then applied to the enclosing top wall and all other walls

within the inflow section. A cyclic condition is imposed on the span-wise boundary of the computational domain, ultimately resulting in an infinite channel-impingement configuration.

Height	Cells	Dimensions
$H = 2D$	$560 \times 150 \times 1$	$26D \times 2D \times 1D$
$H = 1D$	$560 \times 100 \times 1$	$26D \times 1D \times 1D$
$H = 0.5D$	$560 \times 50 \times 1$	$26D \times 0.5D \times 1D$

Table 4.1.: Arrangement of numerical cells and dimensions of the solution area for three nozzle-to-plate distances for the calculations with the conventional RSM.

Height	Cells	Dimensions
$H = 2D$	$300 \times 100 \times 30$	$26D \times 2D \times 6D$
$H = 1D$	$300 \times 60 \times 30$	$26D \times 1D \times 3D$
$H = 0.5D$	$300 \times 40 \times 30$	$26D \times 0.5D \times 3D$

Table 4.2.: Arrangement of numerical cells and dimensions of the solution area for three nozzle-to-plate distances for the simulations with the IISRSM.

All three DNS-relevant cases differing in the nozzle-to-plate distances - $H = 2.0$D, 1.0D and 0.5D - are calculated by both RSM versions. The length of the flow development region after impingement and the solution domain extension in the span-wise direction, as well as the resulting grid sizes, are summarized in Tables 4.1 and 4.2 for the RSM and IISRSM calculations, respectively. The corresponding grid spacings in wall units are in the range of $\Delta x^+ = 0.91 - 113.44$, $\Delta y^+ = 0.012 - 0.79$, and $\Delta z^+ = 36.31 - 53.92$ for the IISRSM simulations and $\Delta x^+ = 0.78 - 56.24$, $\Delta y^+ = 0.01 - 0.91$ for the two-dimensional finite volume mesh associated with the RSM calculations.

Results and Discussion

The outcomes of the comparative assessment of the previously introduced modeling approaches are showcased, encompassing mean flow and thermal field properties, the associated Reynolds stress tensor $\overline{u\prime_i u\prime_j}$ along with its anisotropic nature. These results are presented for three distinct nozzle heights, namely H/D = 0.5, 1.0, and 2.0. For an initial overview of the fundamental structural features within the examined flow cases, Figure 4.7 provides a visualization. This figure displays iso-contours of instantaneous velocity and temperature fields, alongside representations of vortical structures based on the Q-criterion. This visualization offers an insight into the basic flow characteristics within the flow configuration for a nozzle-plate distance of H/D = 2.0 .

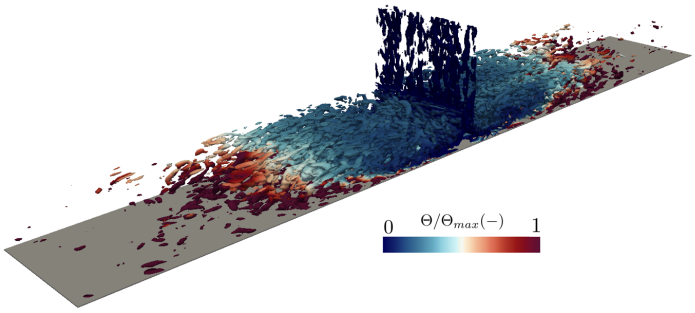

Figure 4.7.: Flow visualization by the Q-criterion, colored by the non-dimensionalized instantaneous temperature field ($\Theta/\Theta_{\max}$) obtained by the IISRSM in slot-jet impingement configuration at a nozzle-height of H/D = 2.0 with constant temperature gradient at the wall.

The results presented illustrate clearly the capability of the IISRSM to resolve the turbulent fluctuations with respect to both velocity- and temperature fields. Their dynamics are mainly governed by their resolved fractions, whose generation is driven by the convective terms in the corresponding transport equations. However, in the wall proximity, the sub-scale turbulent momentum and heat fluxes are appropriately enhanced and are therefore crucial for the correct capturing of the near-wall effects.

The flow impingement occurring under the influence of varying nozzle-to-target distance is by far more complex than the previously considered wall-parallel channel flow. This is furthermore enhanced by the simultaneously present thermal field initiated by the heated wall which strongly modifies the near-wall flow structure leading to an increased influence of the viscosity. The integration of the governing equation down to the wall itself and application of the wall-boundary

conditions relying on the asymptotic behavior of the turbulence quantities by approaching the solid wall is therefore of particular importance.

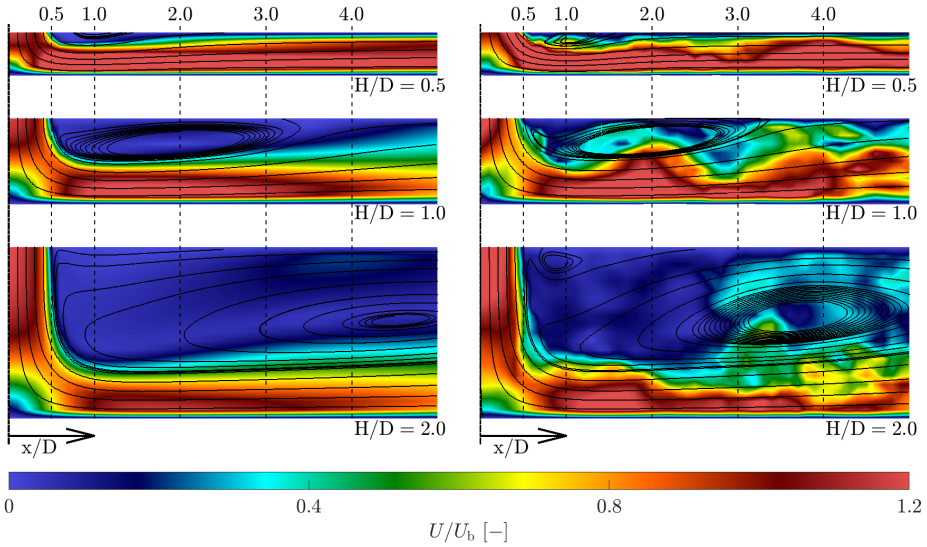

Figure 4.8.: Iso-contours of the instantaneous velocity field, colored by its magnitude, and corresponding mean streamlines obtained by the baseline RSM (left) and the scale-resolving IISRSM (right) at three nozzle-to-wall distances $H/D = 0.5$, $H/D = 1.0$, $H/D = 2.0$.

The mean flow topology (Figures 4.8) reveals a flow pattern typically characterizing impinging jet configurations featured by an intensive alternation in the velocity gradient, from abrupt jet deceleration in the immediate impingement area toward a prompt 90^o flow skewing and transition into the wall-jet region followed by a strong acceleration and subsequent flow relaxation. It is furthermore well known that a streamline curvature-induced turbulence production takes place here, which represents an inherent feature of Reynolds stress modeling techniques, but on the other hand is beyond the reach of the eddy-viscosity modeling concept.

Figure 4.8 visualizes the iso-contours of the RANS-RSM-related time-averaged (left) and IISRSM-related instantaneous velocity fields (right) colored by their magnitudes (normalized by the bulk velocity of the incoming channel flow U_b), respectively, illustrating the flow pattern variability as a function of the distance between the channel-shaped nozzle and the bottom wall - $H/D = 0.5, 1.0$ and 2.0; it is recalled that the characteristics of the fully-developed channel flow previously discussed correspond closely to those of the present inflow channel.

The representation of the mean flow topology aims to identify the characteristic flow localities within the impingement and wall-jet regions, enabling a more focused assessment of the predictive capability of the turbulence models used. The mean streamlines originating from the inlet channel enable a detailed insight into the flow topology around the stagnation point region. The streamline pattern indicates a right-angle bifurcation of the incoming flow characterized by a strong local curvature, signifying a rapid transition from flow deceleration (associated with impingement) to subsequent acceleration immediately downstream of the stagnation point ($x/D = 0$). The deceleration of the vertical flow and the subsequent acceleration of the horizontal flow after the impingement is closely correlated with the pressure gradient alternation around the stagnation point. The flow field consists of an inflowing vertically downward stream with a pronounced velocity gradient in the discharge zone, as well as an outflowing wall-bounded jet representing the consequence of the impingement occurrence. These two flow regions interface with the remaining low-intensity velocity field near the upper wall. Downstream of the impingement region, the wall jet exhibits significant spreading due to streamline displacement and widening of the flow region near the wall. This is accompanied by flow relaxation in the post-acceleration region. The presence of the upper wall limits the relaxation process, affecting the spatial suppression of the fast flow stream toward the lower wall, which was particularly noticeable in Case 1 with the smallest gap height of $H/D = 0.5$. The blue colored area between the wall jet and the upper wall, becoming gradually smaller as the distance between the nozzle and the wall is reduced, represents a zone of weak backflow intensity (in agreement with the negative axial velocities in Fig. 4.9). The velocity gradient within the shear layer exhibits high variability in regions aligned with the streamline separating the high velocity flow stream from the low velocity region for both the outflowing free jet and the wall confined jet. These regions with steep changes in the velocity field are identified as sources of increased turbulence activity.

In order to quantitatively evaluate the accuracy of the present computational results, the profiles of the mean flow and thermal quantities and the corresponding turbulence variables obtained by using both turbulence model formulations are directly compared with the available Direct Numerical Simulation (DNS) data of Hattori and Nagano (2004) at specific cross sections. These locations, indicated by dashed lines in Figure 4.8 are situated within three distinct flow regions: the immediate impingement region ($x/D = 0.5$), the region of alternating velocity gradient (from deceleration to acceleration) and wall-jet formation ($x/D = 1.0$), and the evolving wall-jet region ($x/D = 2.0$, 3.0 and 4.0). The analyzed flow variables include the axial velocity component (U/U_τ), the streamwise and wall-normal Reynolds stress intensities ($\sqrt{\overline{u'u'}}/U_\tau$ and $\sqrt{\overline{v'v'}}/U_\tau$, the mean temperature ($\overline{\Theta}$), and two integral flow quantities: friction coefficient (C_f) and Nusselt number (Nu) at the heated bottom wall.

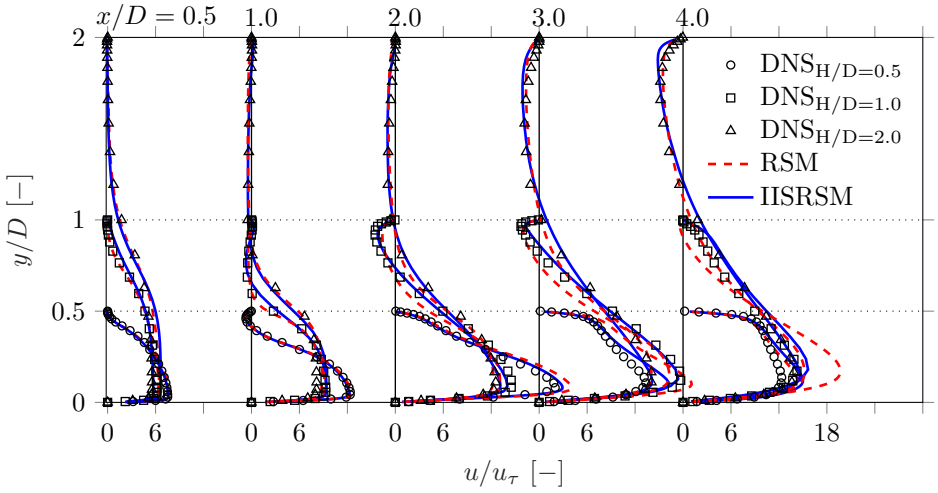

Figure 4.9.: Profile development of the mean axial flow velocity in x direction in the slot-jet impingement configuration for all three nozzle-to-plate distances $H/D = 0.5, 1.0, 2.0$.

Figure 4.9 shows the velocity profile development in main outflow direction (x-direction). As mentioned earlier, the axial velocity profiles in the upper part of the flow zone (colored blue in Figures 4.8) have low values that undergo a gradual flow reversal with slightly increasing intensity as the distance H increases, as indicated by the negative velocity values. This trend is statistically quantified by the continuous expansion of the recirculation zone with respect to distance H. The intensification of the negative velocity values, although still relatively small compared to the highly accelerated wall jet region, is consistent with this behavior. The velocity plots demonstrate a high level of agreement, both qualitatively and quantitatively, between the present computational model results and the DNS data for all three configurations considered. This is especially true for the IISRSM-related profiles, which finally indicate a correctly predicted size of the recirculation zone at the upper wall for all three cases. Considering the lower flow intensity in this region correlated with weak turbulence activity, representing generally a dominant driving force within turbulence transport dynamics, this is certainly a noteworthy outcome. The velocity profiles exhibit strong gradients in both the wall-normal and wall-parallel directions, indicating varying intensities of flow acceleration within the wall-jet region as the nozzle-to-wall distance increases. The largest relative acceleration within the wall-jet region, in relation to the friction velocity U_τ (with $U_\tau = \sqrt{\tau_w/\rho}$), is observed at location $x/D = 2.0$, corresponding to case 1 with the smallest gap ($H/D = 0.5$), while case 3 with the largest gap ($H/D = 2.0$) exhibits the

least intense acceleration. These velocity field variations follow closely the DNS database. As expected, the IISRSM-related results are superior to those obtained by RANS-RSM. However, the latter velocity profiles show good agreement with the DNS results at the first three streamline locations up to $x/D = 2.0$, with some noticeable deviations visible further downstream at the locations $x/D = 3.0$ and 4.0. Nevertheless, the mutual comparison between the profiles considering different gap heights H is consistent with the IISRSM results and the DNS database.

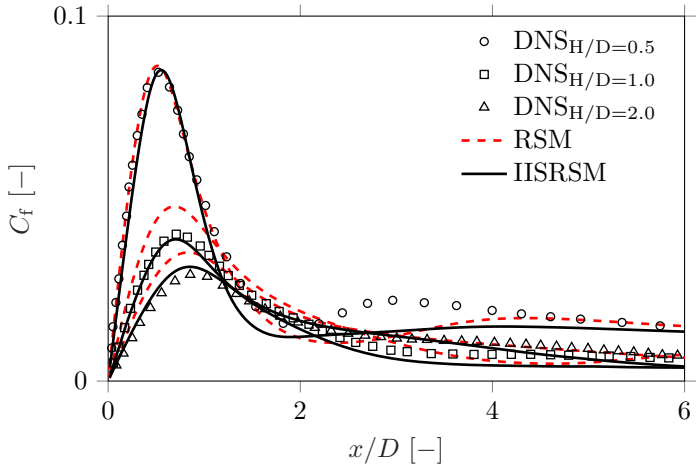

Figure 4.10.: Distribution of surface friction coefficient at lower wall C_f determined by RSM and IISRSM compared to DNS data for all three nozzle-to-plate distances $H/D = 0.5, 1.0, 2.0$.

The variation of the velocity profiles for all three nozzle-plate spacings are reflected in a significant difference in the evolution of the friction coefficient at the bottom wall. Fig. 4.10 shows a comparison between the friction coefficients ($C_f = \tau_w/(0.5\rho U_b^2)$) calculated with the turbulence models employed for all three flow configurations. The friction coefficient distributions are characterized by a distinctly pronounced peak near the center of the impingement point and a flattened evolution in the wall jet region downstream. For all three configurations, the computational model results are in good overall quantitative agreement with the DNS data. However, the RSM-related results show a slight overprediction of the peak value in the cases with a nozzle-to-plate distance of $H/D = 1.0$ and 2.0. Another significant discrepancy is observed downstream of the impact point for case 1 ($H/D = 0.5$). Both the IISRSM and the RSM significantly underpredict the second maximum of the friction coefficient at the dimensionless distance $x/D \approx 3$ from the impact point, characterizing primarily the case with

the smallest gap. This underprediction is considered reasonable for inherently steady RANS turbulence models, since they are known to be incapable to capture the spectral turbulence dynamics of an impinging jet. The latter is particularly important because, according to Hadžiabdić and Hanjalić (2008), the phenomenon of this second maximum is related to the redirection of the fluctuating velocity component at this locality. On the other hand, the IISRSM is the model that can capture the spectral dynamics to an extent governed by the solution of the relevant turbulence quantity equations and the underlying spatial and temporal resolutions. The latter numerical grid-related parameters, employed presently, are obviously insufficiently fine. A similar behavior can be observed in the distribution of the Nusselt number (Fig. 4.15, 4.16, 4.17). Accordingly, the discussion of the possible reasons for this deviation will be continued in this context.

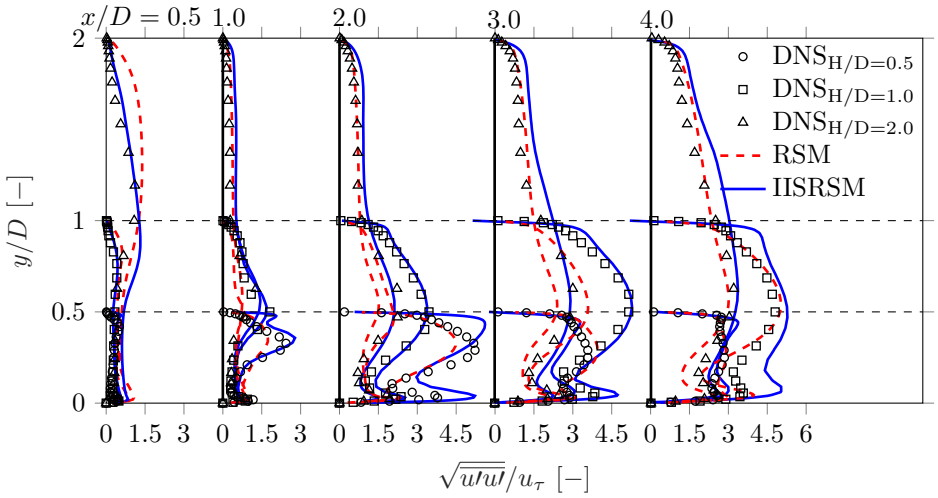

Figure 4.11.: Profile development of the streamwise ($\sqrt{\overline{u'u'}}/U_\tau$) Reynolds stress intensity in the slot-jet impingement configuration for all three nozzle-to-plate distances $H/D = 0.5, 1.0, 2.0$.

The assessment of the predictive capabilities of both turbulence models employed, RSM and IISRSM, with respect to the turbulence fields is interpreted below. In this regard, the streamwise and wall normal Reynolds stress intensity components ($\sqrt{\overline{u'u'}}/U_\tau$) (Fig. 4.11) and ($\sqrt{\overline{v'v'}}/U_\tau$) (Fig. 4.12), normalized by friction velocity, are shown at the axial positions $x/D = 0.5, 1.0, 2.0, 3.0$ and 4.0 from the point of impact. It is recalled that the Reynolds stress distribution in the corresponding channel-shaped inflow (not presented here)

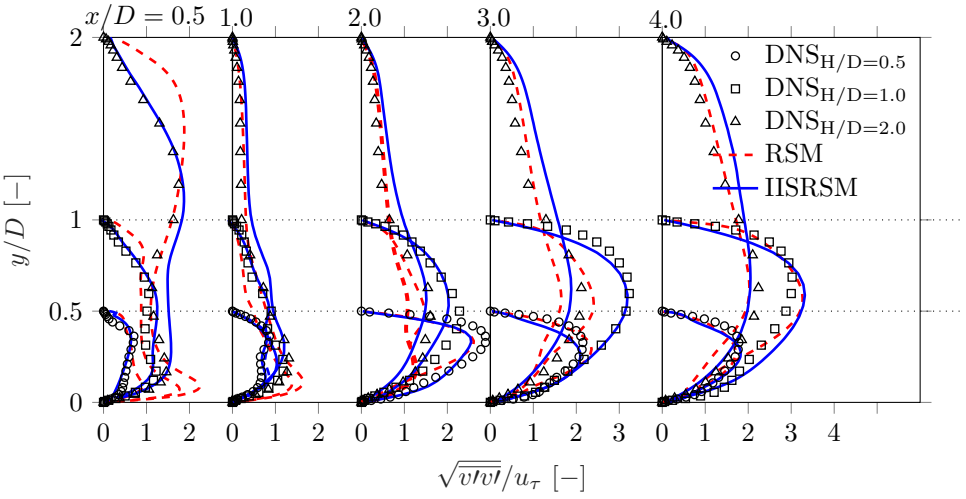

Figure 4.12.: Profile development of the normal-to-wall ($\sqrt{\overline{v'v'}}/U_\tau$) Reynolds stress intensity in the slot-jet impingement configuration for all three nozzle-to-plate distances $H/D = 0.5, 1.0, 2.0, 3.0, 4.0$.

shows very good agreement for both RANS models in comparison with the relevant DNS data, similar as in the fully-developed channel flow studied previously.

The Reynolds stress profile development demonstrates, especially around and downstream of the sharp edge of the inlet channel, increased turbulence production due to the rapidly developing free shear layer between the fully-developed inflow and the low-velocity region. The zone bordering the wall-bounded jet and the low-velocity flow region exhibited even more pronounced turbulence production. The wall jet extends over the entire height of the confinement (Fig. 4.8) within the Case 1 showing the highest turbulence activity within the flow impingement configuration up to $x/D = 2.0$. The development of both sets of profiles exhibits similar behavior, with one notable difference. The lower peak observed near the bottom wall corresponds to the streamwise stress component and correlates directly with the axial velocity gradient near the wall. However, this peak is not present in the normal-to-wall stress component. The maximum values of both stress components in all three cases and at all five selected streamwise positions coincide with the shear layer zone aligned with the streamline bordering the wall-jet region. In the horizontal duct, both Reynolds stress components show a gradual increase in turbulence intensity towards the outlet, particularly in case 3, which has the largest distance to the bottom wall ($H/D = 2$). It is important to exercise caution when drawing conclusions based on these findings since the Reynolds stress component intensities are normalized by $U_\tau = U_b\sqrt{C_f/2}$ (Fig.

4.10), where the largest C_f values at the locations $x/D = 0.5$ and 1.0 have the most significant impact on the lowest normalized turbulence level in this flow region. In the remaining part of the duct, the development of C_f values shows only minor variations, suggesting their proximity across all three cases. In any case, the largest relative increase in turbulence intensity is observed in case 2, which has a gap height of $H/D = 1.0$. Conversely, case 1, with the smallest gap height of $H/D = 1.0$, exhibits a decay in cross-sectional turbulence intensity.

The predicted axial stress components ($\sqrt{\overline{u'u'}}/U_\tau$) for both RANS-based models agree well overall with the compared DNS data. However, the scale-resolved IISRSM shows higher agreement with the reference DNS data compared to the baseline RSM, as expected. For impinging jet configurations, and especially in the wall jet region, the wall normal stress component ($\sqrt{\overline{v'v'}}/U_\tau$) plays a dominant role in the model formulation when a gradient approach is used to describe the turbulent heat flux, with the normal-to-wall temperature gradient overweighting the gradients in other coordinate directions. Accordingly, its correct prediction is of crucial importance. The corresponding RSM-related profiles of the two Reynolds stress intensity components at $H/D = 0.5$ show a significant overestimation of the near-wall peak, which is not visible in the present DNS data. This overestimation is a direct consequence of a local overestimation of turbulent production near the central impingement locality when the fully-developed channel flow impinges on the bottom wall. In the subsequent wall-jet region, a systematic relaxation in the form of a significant underestimation of both stress components is observed for all three cases, which correlates with the flow acceleration within the developing wall-jet region; some enhancement of the turbulence field, which agrees well with the DNS data and the IISRSM results, is evident at the $H/D = 4.0$ location corresponding to the fully developed wall-jet region. Contrary, the profiles of the wall parallel as well as the wall normal Reynolds stress intensity components predicted by the IISRSM show a steady increase of the respective turbulence intensity, following closely the DNS reference.

The last two last plots displaying the quantities of the thermal field induced by the constant wall heating, the mean temperature $\overline{\Theta}$ (Fig. 4.13 & 4.14), normalized by the difference between temperatures at the inlet ($\overline{\Theta}_{inlet}$) and at the wall ($\overline{\Theta}_{wall}$), and the distribution of the Nusselt number (Fig. 4.15, 4.16, 4.17), allow a discussion of the predictive performance of the heat-flux models adopted. The computational RSM-related results shown in Fig. 4.13 are obtained by applying the SGDH model (Eq. 2.30), analogous to the IISRSM. The results obtained with other investigated model formulations differ only slightly. A more distinct mutual deviations, although also noticeably small, can be seen in the Nusselt number distribution (Fig.4.15, 4.16, 4.17). The significant variations in the temperature profiles are primarily observed in the immediate vicinity of the bottom wall. As a result, the main focus of this investigation is on

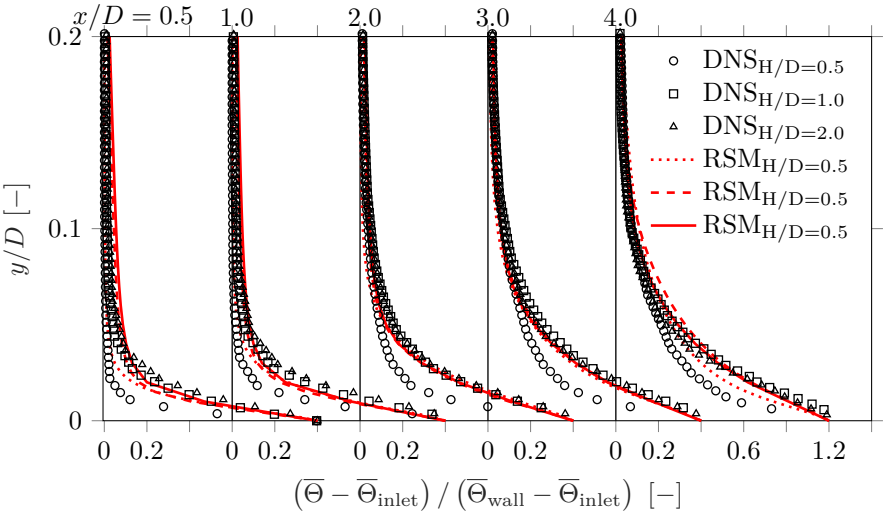

Figure 4.13.: Profile development of the temperature $\overline{\Theta}$ in x direction in the slot-jet impingement configuration obtained by the steady RSM for all three nozzle-to-plate distances $H/D = 0.5, 1.0$ and 2.0.

the spatial evolution of the near-wall temperature fields along the axial direction. Specifically, the analysis covers a dimensionless wall distance up to $y/D \leq 0.2$.

From the moment of impact at $x/D = 0.0$, the heated lower wall consistently affects the temperature field formation and its thermal boundary layer. Fig. 4.13 & Fig. 4.14 shows the spatial progression of the temperature profiles in the axial x direction, which points to a steadily thickening thermal boundary layer as a result of the constant heat flux at the bottom surface. The near-wall temperature gradient $(\partial\overline{\Theta}/\partial y)$ has its maximum near the point of impact $(x/D \approx 0.0 - 0.5)$ and decreases gradually from there toward the outlet of the horizontal channel. This phenomenon is manifested through an enhanced heat propagation from the boundary layer into the flow core, which is accompanied by the weakening of the temperature gradient mentioned above. This indicates that the convective transport of the induced thermal energy is strongest at the immediate impingement region and weakens in the axial direction thereafter. Both the RSM and IISRSM are capable to qualitatively reproduce the overall evolution of the temperature profile compared to the DNS data. The temperature profiles in the case of the configurations with larger heights of the horizontal channel - $H/D = 1.0$ and 2.0 - are correctly reproduced in its entirety. The corresponding profiles also show very good mutual agreement, indicating the weak influence of the distance between the channel-like nozzle outlet and the impact plate on the thermal field (this is also

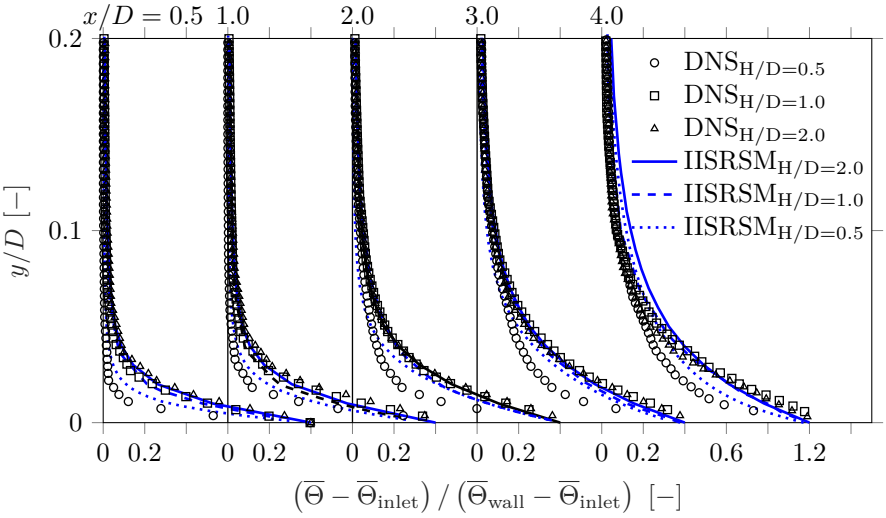

Figure 4.14.: Profile development of the temperature $\overline{\Theta}$ in x direction in the slot-jet impingement configuration obtained by the scale resolving IISRSM for all three nozzle-to-plate distances $H/D = 0.5, 1.0$ and 2.0.

visible in the case of the Nusselt number distribution, Fig. 4.15, 4.16, 4.17. This finding is fully consistent with the study of Behnia, Parneix, Shabany, and Durbin (1999), which confirms that the influence of nozzle-to-impingement-plate distance is noticeable only at the gap heights H/D smaller than unity. On the other hand, the temperature profiles corresponding to the narrowest gap ($H/D = 0.5$) predicted by both RANS-based models in the vicinity of the wall differ from the DNS data; this deviation becomes more pronounced with increasing distance from the impact region. The IISRSM-related results still follow the DNS data somewhat more closely. Nevertheless, for all three configurations, the results show that the corresponding wall temperature values are correctly predicted by both RSM and IISRSM calculations. A notable shift in the temperature profiles is observed in terms of the intensity of the corresponding gradient at $x/D \geq 2.0$. In contrast to locations where $x/D < 2.0$, the temperature gradient in Case 2 ($H/D = 1.0$) exhibits a more significant weakening compared to Case 3 ($H/D = 2.0$). This specific observation has been adequately reflected in the present simulation results.

The distribution of the Nusselt number Nu, representing a dimensionless parameter used to quantify convective heat transfer, is depicted in Fig. 4.15, 4.16, 4.17. It is presently determined as the difference between the temperature at a given point ($\overline{\Theta}$) and the inlet temperature ($\overline{\Theta}_{inlet}$), divided by the difference between the wall temperature ($\overline{\Theta}_{wall}$) and the inlet temperature: $(\overline{\Theta} - \overline{\Theta}_{\text{inlet}})/(\overline{\Theta}_{\text{wall}} - \overline{\Theta}_{\text{inlet}})$.

Accordingly, the Nusselt number progression is strongly influenced by the temperature field near the wall, as it is directly affected by its gradient. Consequently, the disparity in convective heat transfer mentioned earlier is reflected in the evolution of the Nusselt number with respect to all three nozzle-to-plate distances. The results obtained by applying different heat flux models (Equations 2.30, 2.31, 2.32, 2.34) in conjunction with the baseline Reynolds Stress Model (RSM) exhibit a significant overestimation of convective heat transfer, especially in the vicinity of the impingement center at $x/D = 0$, extending up to 2.0. However, when applied in the context of the Sensitized RANS-RSM framework, the IISRSM-related Nusselt number distribution shows a significantly better agreement with the reference DNS database. This improvement can be attributed to the superior prediction capabilities of IISRSM for the underlying Reynolds stress field compared to its baseline RSM counterpart. In particular, the accurate prediction of the wall-normal stress component ($\sqrt{\overline{v'v'}}/U_\tau$) by IISRSM, as shown in Figure 4.12, has a significant impact on the accurate determination of the turbulent heat flux and the resulting near-wall thermal field.

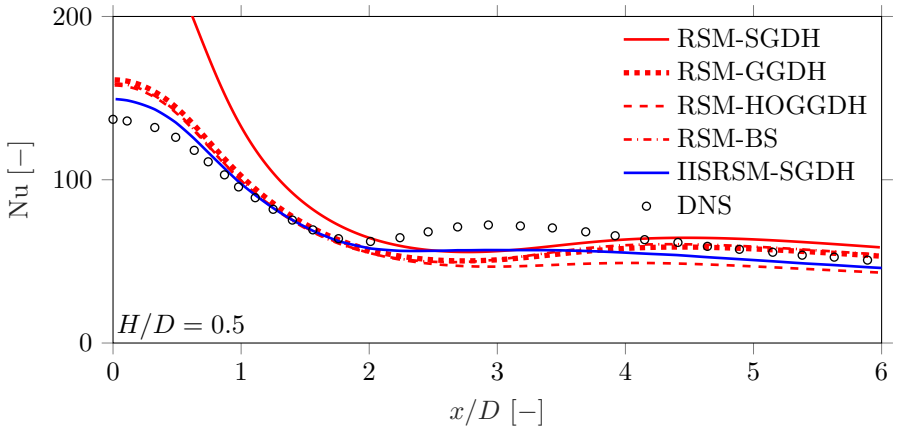

Figure 4.15.: Distribution of the Nusselt number Nu at the bottom impingement wall for the nozzle-to-plate distance $H/D = 0.5$ for the single-slot-jet impingement configuration at a bulk Reynolds number of $\mathrm{Re_b} = 10000$.

A notable characteristic of impinging jet configurations is the occurrence of a secondary peak in the Nusselt number downstream of the impingement point. At a certain distance from the high pressure stagnation point, the flow suddenly slows down. Structurally, according to Hadžiabdić and Hanjalić (2008), a local recirculation zone corresponding to a shear-layer vortex aligned with the wall jet boundary is formed, which then causes its global deceleration. The substantial

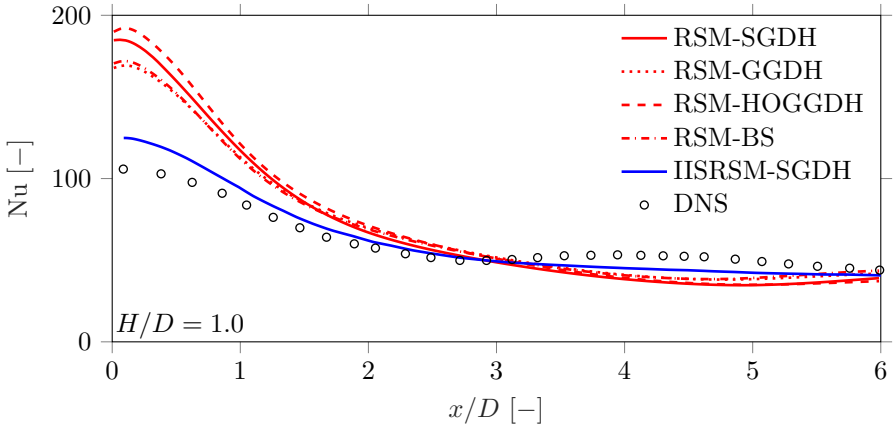

Figure 4.16.: Distribution of the Nusselt number Nu at the bottom impingement wall for the nozzle-to-plate distance $H/D = 1.0$ for the single-slot-jet impingement configuration at a bulk Reynolds number of $\mathrm{Re_b} = 10000$.

relative decrease in the bulk value of the axial velocity component is evident in Fig. 4.9, observed especially between the axial positions $x/D = 2.0$ and 3.0 for a nozzle-to-plate distance of $H/D = 0.5$. A similar, but clearly weaker deceleration is observed for the nozzle-outlet-wall spacings of $H/D = 1.0$ and $H/D = 2.0$, but is shifted downstream between the streamwise locations $x/D = 3.0$ and 4.0. Therefore, the second Nusselt number peak is most pronounced for the smallest nozzle-to-plate distance of $H/D = 0.5$ and gradually decreases as the gap height increases, reaching a significantly lower value, resulting finally in its complete absence for the largest spacing of $H/D = 2.0$. The observed delays in the bulk flow, coupled with an accompanying thickening of the boundary layer, are also associated with an asymmetry in the velocity and Reynolds stress profiles and their intensified gradients near the wall. This behavior is illustrated by the analogous abrupt change in the distribution of the friction coefficient shown in Fig. 4.10, which directly corresponds to the behavior of the Nusselt number, whose distribution follows a similar pattern.

These intricate relationships pose a significant challenge to the inherently steady Reynolds-Averaged Navier-Stokes (RANS)-based turbulence models. Presently, both RANS-based models, including the Sensitized RANS model, could not accurately reproduce the second Nusselt number peak at a nozzle-to-plate distance of $H/D = 0.5$. Nevertheless, the scale-resolving IISRSM exhibits a tendency to provide notably improved predictions, especially for the Nusselt number evolutions for the impinging jet configurations with the gap heights of $H/D = 1.0$ and

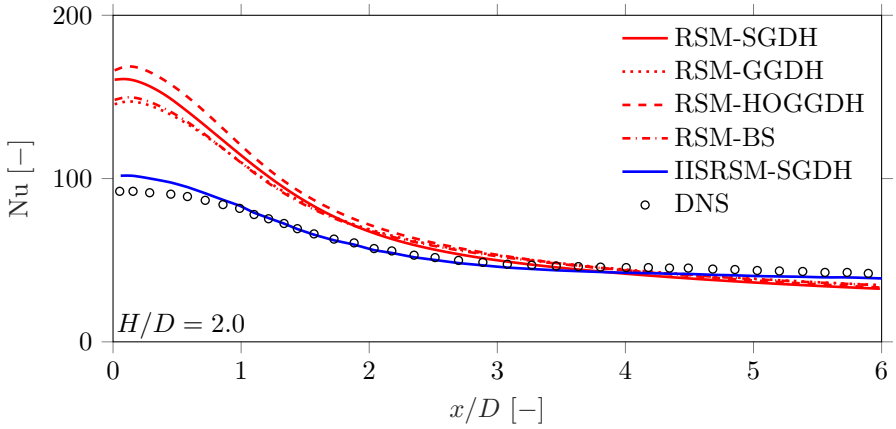

Figure 4.17.: Distribution of the Nusselt number Nu at the bottom impingement wall for the nozzle-to-plate distance $H/D = 2.0$ for the single-slot-jet impingement configuration at a bulk Reynolds number of $\mathrm{Re_b} = 10000$.

$H/D = 2.0$. According to Hadžiabdić and Hanjalić (2008), the distinctive second peak within the Nusselt number distribution, characteristic of the narrowest gap of $H/D = 0.5$, can be interpreted as a direct outcome of a low intensity wall-bounded detachment of the fluctuating flow field at this specific position. Capture of these flow phenomena exceeds the predictive capabilities of the currently employed steady RANS-RSM model, but can be partially predicted using the scale-resolving IISRSM. Addressing this underprediction may require a more detailed analysis, also with respect to the grid resolution requirements, especially at this locality, considering that the standard grid resolution constraints are primarily derived for wall-parallel flows (see e.g., Hadžiabdić and Hanjalić (2008)).

Concluding, simulations of three different slot-jet impingement configurations at nozzle-to-wall distances of $H/D = 0.5, 1.0$, and 2.0 on a heated wall were performed to further validate the predictive capabilities of a baseline RANS-RSM model and its Sensitized-RANS extension (IISRSM) under conditions of much more complex flow deformation, considering higher-order modeling for turbulent heat flux. The results show qualitative consistency between the RANS-based models in reproducing the velocity fields and the evolution of the friction coefficients compared to the DNS reference data. However, the scale-resolving IISRSM demonstrated significantly better predictive performance. The IISRSM improved the prediction of turbulent stresses in the central impingement region compared to the RSM, which resulted in too high a turbulence level, indicating its improved capability to account for turbulence unsteadiness. The differences in

the thermal fields obtained by applying different heat flux models in conjunction with the IISRSM are not as pronounced. Both gradient-diffusion approaches tested provide qualitatively valuable coefficient predictions when combined with the scale-resolving Reynolds-Stress model. The use of various heat-flux models in conjunction with the baseline RSM led to obvious differences in the thermal field determination, mostly in the immediate impingement region, with all model combinations yielding excessive heat transfer intensity as indicated by a too high Nusselt number.

Concluding the present section concerning important preliminary investigations, a numerical simulation was performed of a turbulent axisymmetric jet with twice the momentum impinging on a heated wall. The baseline RSM in combination with the considered heat flow models yielded a reasonable distribution of the Nusselt number for radial distances $x/D \geq 2$ where a mean shear induced flow behavior dominates. However, similar to the previous configuration, within and around the immediate impingement region up to $x/D \leq 2$, significant overprediction occurred due to more intense turbulence activity, exceeding by far the DNS-related results. In contrast, the scale-resolving IISRSM provided better predictions for velocity, Reynolds stress, and temperature profiles, closely following the DNS database. An exception is the resulting Nusselt number distribution, which showed a slight underprediction compared to the DNS reference data. A well-known feature of the latter global thermal field property, its second maximum characterizing the wall-jet development at higher impinging jet momentum (as specific to the round jet impingement considered here) and smaller nozzle-to-wall distances (relevant to the slot-jet impingement with $H/D = 0.5$), requires further analysis with respect to spatial and temporal resolution criteria in such wall-perpendicular flows.

5. Leading configurations

5.1. TUDa Flowbench - IC engine intake flow

The flow pattern in internal combustion engines plays a critical role in the combustion process and has a direct impact on engine efficiency and emissions. The flow within the relevant piston-cylinder assembly, the so-called TUDa Flowbench is significantly influenced by the interaction of various phenomena occurring simultaneously, even in the absence of combustion or heat transfer processes. The flow complexity arises from phenomena such as interacting injector jets, tumbling and swirling motion, wall shear stress variation and stretching as well as squeezing effects on the working fluid during expansion and compression modes of engine operation. Accordingly, the flow characteristics to be adequately described include complex flow straining caused by the collision of multiple intake jets and their subsequent impingement on the cylinder walls and piston surface, as well as multiple wall-bounded and free separation events. These phenomena lead to a complex, transient and recirculating flow topology with cyclic large-scale movements characterized by high-intensity anisotropic turbulence. Today, the design and optimization of internal combustion engines benefit greatly from Computational Fluid Dynamics (CFD) packages. In the past, the prediction of engine flow relied heavily on conventional Reynolds-Averaged Navier-Stokes (RANS) models. However, these RANS models, which use single-point closures based on a characteristic length scale related to large-scale motion, fail to capture an important part of the turbulence spectrum. As a result, they cannot satisfactorily capture the physics of flows dominated by organized, large-scale coherent structures. Recognizing this limitation, the engineering community has realized that advanced turbulence models capable of reproducing the fluctuating flow field are required to accurately predict the aforementioned flow phenomena. Studies by Rutland (2011) and Hasse (2016)), in their reviews on the feasibility of eddy-resolving turbulence models such as Large Eddy Simulation (LES) and hybrid RANS/LES, confirmed the need for such models in the calculation of combustion engine flows. Recently, Schmitt, Frouzakis, Wright, A. G. Tomboulides, and Boulouchos (2015) Schmitt et al. and Schmitt, Frouzakis, Wright, A. Tomboulides, and Boulouchos (2016) enriched the computational database by performing high-quality direct numerical simulations (DNS) of cylinder-piston assemblies operating under compression conditions, including the representation of the associated thermal field. Subsequently,Keskinen, Koch, Wright, Schmitt, Nuutinen, Kaario, Vuorinen, Larmi,

and Boulouchos (2018) simulated the above-mentioned DNS-related configurations using a wall-modeled LES approach. Haussmann, Ries, Jeppener-Haltenhoff, Li, Schmidt, Welch, Illmann, Böhm, Nirschl, Krause, et al. (2020) evaluated different wall-modeling treatments in an LES of an engine intake flow. The main objective of this section is to validate the recently developed eddy resolving RANS model IISRSM (Sec. 2.4.2), whose subscale model considers the dynamics of the entire fine structure tensor under conditions of coarser grid resolutions. In addition, a complementary LES using an appropriately fine grid is also performed.

Case setup and computational domain

The design of the TUDa Flowbench setup, considered presently, corresponds to the geometry of the spray-guided engine, representing a single-cylinder direct-injection engine. The configuration mimics the flow conditions when both valves are fully opened and the piston acceleration is zero. The configuration is experimentally investigated using the Magnetic Resonance Velocimetry (MRV) measurement technique at the Technical University of Darmstadt by Freudenhammer, Baum, Peterson, Böhm, Jung, and Grundmann (2014).

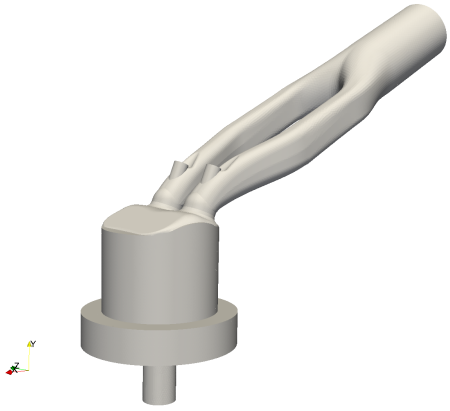

Figure 5.1.: Stereolithography of the considered TU Da Flowbench configuration for the reference experimental investigation of Freudenhammer, Baum, Peterson, Böhm, Jung, and Grundmann (2014) and all numerical LES- and scale resolving RANS-based computational simulations.

Accordingly, the flow configuration considered resembles an annular jet formed inside the intake-manifold at a Reynolds number of 38000, impinging on the cylinder liner and piston walls and forms complex vortical structures. The flowbench is a single-cylinder direct injection engine. It includes a twin-cam, overhead-valve

pent roof engine. Bore and stroke of the engine is 86 mm and it is operated at 800 RPM. The intake valves are fixed to a lift of 9.21 mm, that corresponds to a CA of 270°bTDC. The inlet mass flow rate is equivalent to 66 L/min, working fluid is water heated up to 40°C. The inlet diameter of the engine is 56.3 mm, just upstream the bifurcation of the manifold. The equivalent Reynolds number at inlet is equivalent to 38000. In the real engine at a CA of 270° bTDC the valve velocity is 0.01 m/s and piston acceleration is near zero. Under these conditions, a quasi steady state flow is established. Inlet Flow complexity refers to a variety of differently structured phenomena, including, among other things, strong streamline curvature, characteristic of impinging flow events and intensified tumbling motion. The so-called 'piston' actually represents an endplate with a centrally positioned opening used to discharge the fluid.

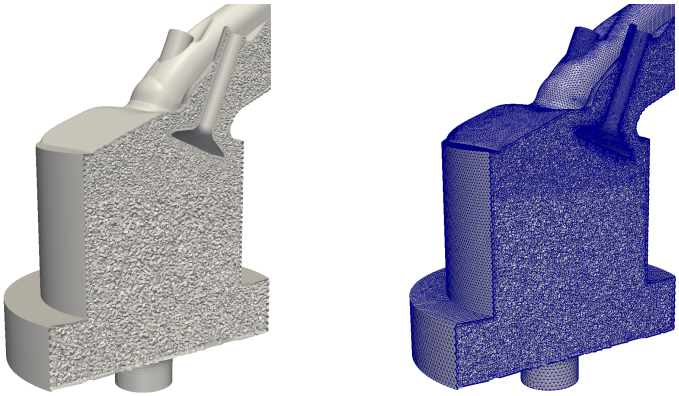

Figure 5.2.: Preprocessed 8 million cells finite-volume mesh of the considered TUDa Flowbench configuration for the numerical LES- and scale resolving RANS-based computational simulations.

The TUDa Flowbench configuration is meshed using the ANSA preprocessing software by BETA CAE Systems International AG. For the scale resolving RANS-RSM-based IISRSM two meshes are generated containing 2.3 and 4 million polyhedral cells. For the reference LES one mesh with 8 millon finite volume mesh cells, seen in figure 5.2, is generated. The finite volume meshes are constructed in a way that the performed numerical simulations resolve the near-wall region with the wall-next cells situated well within the viscous sub-layer. To capture the flow behaviour of the viscous sub-layer correctly the wall-nearest cell centers of all considered finite volume meshes are situated at a dimensionless distance of $y^+ < 1$ throughout the flow domain. Additionally, for comparative assessment, the reference LES was performed using the σ-subgrid-scale model of Nicoud and Ducros (1999) on a grid of 8 million cells.

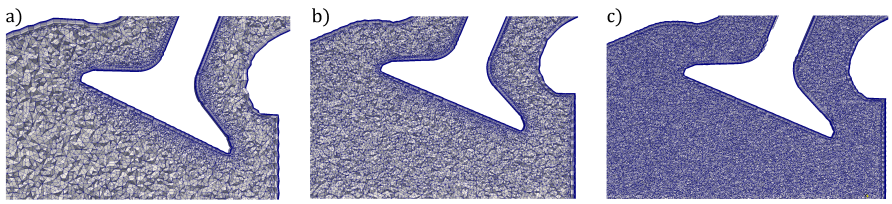

Figure 5.3.: Comparison of the computational grid around the inlet valve for the IISRSM (a) 2.3m cells & (b) 4m cells as well as for the reference LES (a) calculations.

Figure 5.3 shows a comparison of the computational grid around the inlet valve of the TUDa Flowbench for the IISRSM (a) 2.3m cells & (b) 4m cells as well as for the reference LES (a) simulations. The corresponding grid spacings in wall units for the coarsest, 2.3 millon cells finite volume mesh are in the range of $\Delta x^+ = 0.41 - 198.19$, $\Delta y^+ = 0.79 - 245.91$, and $\Delta z^+ = 0.81 - 229.64$. The grid spacings in wall units for the 4 millon cells finite volume mesh are in the range of $\Delta x^+ = 0.36 - 103.82$, $\Delta y^+ = 0.58 - 116.38$, and $\Delta z^+ = 0.89 - 131.84$. The grid spacings for the corresponding reference LES are in the range of $\Delta x^+ = 0.27 - 57.63$, $\Delta y^+ = 0.63 - 84.33$, and $\Delta z^+ = 0.23 - 73.28$ within the refined region around the inlet and the valves. To reduce the computational effort, the LES mesh is coarsened in vicinity to the outlet of the flow domain.

To provide an additional baseline for the validation of the URANS-based IIS-RSM a reference LES is carried out. Due to lack of experimental turbulence data, the LES is applied to enrich the reference database in addition to the experimental MRV measurements. The MRV measurements for this particular study provide exclusively time-averaged volumetric velocity fields without any further information of turbulence. The TUDa Flowbench is a highly turbulent flow configuration with turbulent eddies of various time and length scales. An LES approach reduces the computational costs by filtering out only the smallest scales of motion which then have to be modelled, while larger scales are fully resolved. When using proven and simple SGS models within an LES framework, a large range of turbulent scales has to be resolved. This directly results in the present, well-resolved 8 million cells finite-volume mesh. However, it is not straight forward to define a sufficient grid resolution for an LES of a complex flow setup like the present Flowbench. To ensure this sufficient grid resolution, multiple corresponding mesh quality parameters will be evaluated in the following.

Due to its dependency of the corresponding numerical discretization and SGS modeling the mesh-related assessment of the uncertainty in an LES is not trivial as mentioned by Celik (2005). It is further important to remark that no

grid-independent solution for LES can be obtained. An overly resolved LES is essentially a DNS where all the turbulence scales are resolved (Speziale, 1998). Therefore different parameters have been proposed to identify an high-quality LES. Two different approaches can be used to test the performance of a SGS model in a priori and a posteriori manner (Vreman, Geurts, and Kuerten, 1997). However, both approaches have their own weaknesses to consider. A priori tests can be too pessimistic, while a posteriori tests can show difficulties distinguishing between discretization and modeling error. Therefore, it is important to adopt both methodology to properly validate an LES. In the present thesis, the performed reference LES as well as the scale-resolving RANS-RSM setup is first verified a priori and then a posteriori against the experimental MRV results. The a posteriori comparison is realized by a comparison of the numerical results against the experimental measurement of the volumetric, time-averaged velocity field of the TUDa Flowbench obtained with the previously described MRV procedure (Freudenhammer, Baum, Peterson, Böhm, Jung, and Grundmann, 2014).

For the a priori analysis, different quality indices are defined by various sources. These quality indexes can be classified according to the analysed parameter, where the SGS viscosity, the grid resolution compared to the Kolmogorov scale and the turbulence kinetic energy are suggested. The LES reference data originates from the work of Pati (2022) and is further applied to all following LES mesh studies within the present thesis.

The, for this work considered LES quality index is derived from the comparison between grid size and the Kolmogorov scale. This quality index compares the length scale of a finite-volume mesh cell with the length scale of the smallest, dissipative eddies within the considered flow.

$$\mathrm{LES\_IQ}_{\eta} = \frac{1}{1 + \alpha_{\eta} \left(\frac{h}{\eta_{\mathrm{k}}} \right)^{m}} \tag{5.1}$$

The quality index $\mathrm{LES\_IQ}_{\eta}$ is shown in Eq. 5.1. Here h is the length scale of the finite volume mesh and η_{k} the Kolmogorov length scale. The Kolmogorov length scale can be estimated by:

$$\eta_{\mathrm{k}} = (\nu^3 / \epsilon^{\mathrm{eff}})^{0.25} \quad \text{with} \quad \epsilon^{\mathrm{eff}} = \frac{\nu + \nu_{\mathrm{sgs}} + \nu_{\mathrm{num}}}{\widetilde{S}^2} \tag{5.2}$$

with ϵ^{eff} representing the effective dissipation rate. In this context ϵ^{eff} accounts for the effects of numerical dissipation. Setting $\alpha_{\eta} = 0.05$ and $m = 0.5$ according to Celik (2005), a value of $\mathrm{LES\_IQ}_{\eta} > 0.8$ is indicating a qualitatively sufficiently resolved LES.

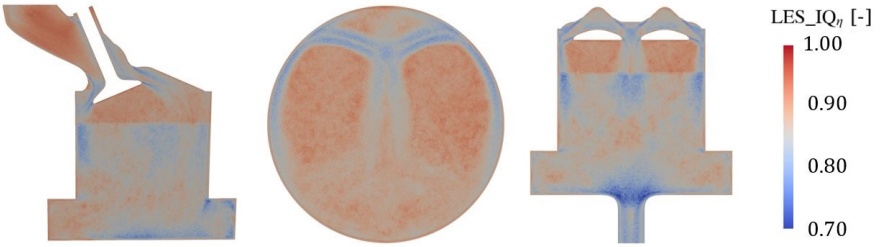

Figure 5.4.: Kolmogorov Scale LES Quality Index field LES_IQ$_\eta$ withing the valve plane (left), the vertical and horizontal and collision plane (middle & right) of the TUDa Flowbench configuration for the corresponding reference LES at its 8 million finite volume cells mesh.

Figure 5.4 shows the Kolmogorov Scale LES Quality Index LES_IQ$_\eta$ on the valve plane of the corresponding 8 million cells LES simulation. The mesh quality index clearly indicates a sufficiently resolved finite volume mesh around the intake valves of the present TUDa Flowbench configuration. It is remarked that, since the evaluation of the present quality index requires information of the overall flow conditions within the analyzed finite volume mesh, an additional grid study was performed. Hereby, the present 8 million cells grid was identified as a suitable solution domain for the reference LES.

As previously mentioned, the quality of a numerical solution in conjunction with its underlying domain can be investigated a priori and a posteriori. The following section contains an a priori analysis of the different URANS setups. A further way to determine the resolved fraction within LES and scale-resolving (U)RANS simulations is to evaluate the ratio of modeled and total turbulence kinetic energy:

$$k_{\mathrm{mod}}/k_{\mathrm{total}} = \frac{k_{\mathrm{mod}}}{k_{\mathrm{res}} + k_{\mathrm{mod}}} \tag{5.3}$$

The modeled turbulence kinetic energy can be determined by $k_{\mathrm{mod}} = 0.5\overline{u_i u_i}_{\mathrm{mod}}$, where $\overline{u_i u_i}_{\mathrm{mod}}$ describes the modeled part of the total RST. Consequently the total turbulence kinetic energy k_{total} comprises the modeled and the resolved turbulence kinetic energy k_{mod} and k_{res}.
Applying Eq. 5.3 to previously described polyhedral 2.3 and 4 million meshes for the scale-resolving URANS simulations, provides insight to the mesh-dependent modeling percentage of turbulence for each case respectively. For an LES a ratio of 20% modeled and 80% resolved turbulent kinetic energy indicates a sufficiently resolved finite volume mesh. Fig. 5.5 shows the indicator $k_{\mathrm{mod}}/k_{\mathrm{total}}$ applied to the 2 and 4 millon cells URANS meshes. The evaluation shows that the percentage of modeled turbulence kinetic energy within the combustion chamber and under

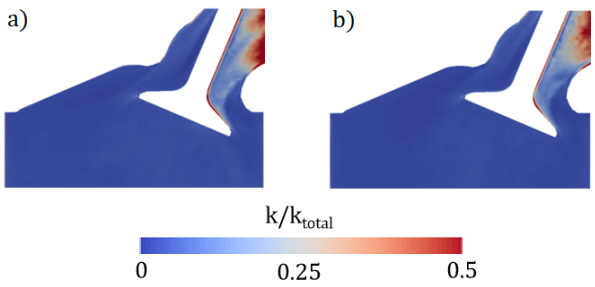

Figure 5.5.: Ratio between the modeled and total turbulence kinetic energy $k_{\mathrm{mod}}/k_{\mathrm{total}}$ for the scale-resolving, RANS-RSM-related IISRSM simulations on the underlying 2.3 and 4 million cells finite volume meshes.

the valves is constantly smaller then 20% for both meshes. However it is important to notice that the modelled part of the turbulence kinetic energy is significantly higher at the intake and above the valves of the combustion chamber. Within these areas, the advanced modelling of the RANS-RSM-based IISRSM should clearly come into effect. The subsequent analysis of the RANS-RSM-related results in comparison to the reference LES and experimental MRV measurements is illustrated within the following section.

Results and Discussion

The following section contains a posteriori validations of the considered numerical simulations against the experimental MRV data and further turbulence analysis between the scale-resolving, RANS-RSM-related simulations and the corresponding reference LES. The present work especially emphasizes the validation of the anisotropic modeling for the RST within the scale-resolving URANS framework by comparing its results against the reference LES.

A first impression of the gerneal flow structure and their corresponding length scales can be obtained by analyzing the instantaneous velocity fields of the scale-resolving IISRSM simulation results on its corresponding 4 million cells mesh in Fig. 5.6. The present section mainly focuses on the evaluation of the tumbling motion within the so called valve plane of the TUDa Flowbench, as seen in Fig. 5.6. The strong velocity gradients and complex geometry as well as the depicted formation of wall-perpendicular jets above the valves provide an excellent opportunity for the a posteriori validation of the considered scale-resolving IISRSM.

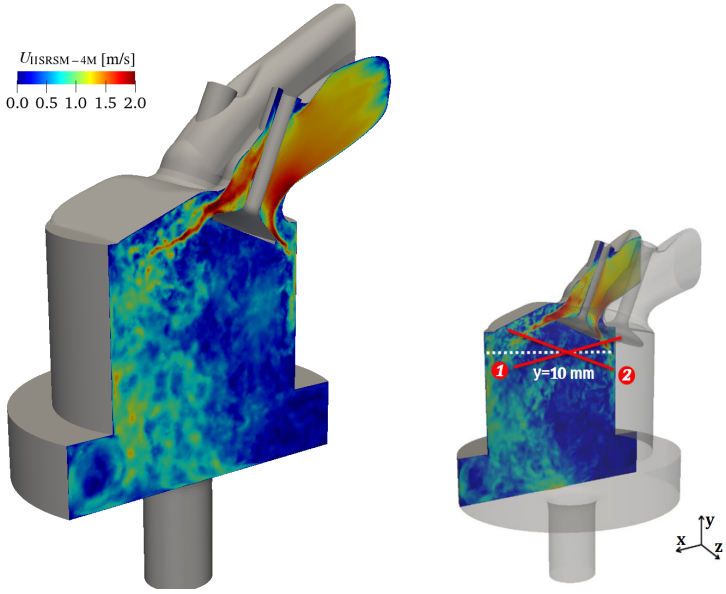

Figure 5.6.: Instantaneous velocity field on the valve plane of the TUDa Flowbench configuration obtained by the scale-resolving IISRSM on the corresponding 4 million cells finite volume mesh.

Therefor, the further analysis of the present internal combustion engine flow is carried out within the previously introduced valve plane.

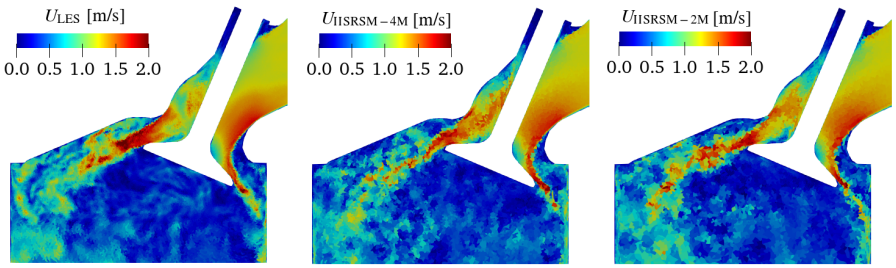

Figure 5.7.: Instantaneous, time-resolved velocity field on the valve plane of the TUDa Flowbench configuration obtained by the scale-resolving IISRSM and LES on the corresponding 2.3, 4 and 8 million cells finite volume mesh.

in Fig. 5.7 the LES and both scale-resolving URANS simulations on the corresponding 2.3 and 4 million cells grid show similar behaviour in jet forming and eddy decay within valve proximity. All simulations show similar velocity magnitudes over the complex valve plane within the Flowbench domain. Due to different numerical grid sizes, there are still minor differences in the diffusivity of the resolved velocity fluctuations between the present calculations respectively. However, these inevitable differences do not impair the overall good agreement of all simulations.

However, instantaneous flow fields are not a suitable option for an a posteriori analysis. The following a posteriori validations of the LES and URANS simulations are performed using time-averaged fields. Therefore, in the first place, all numerically obtained mean velocity fields are directly compared to the experimental MRV data provided by Freudenhammer, Baum, Peterson, Böhm, Jung, and Grundmann (2014).

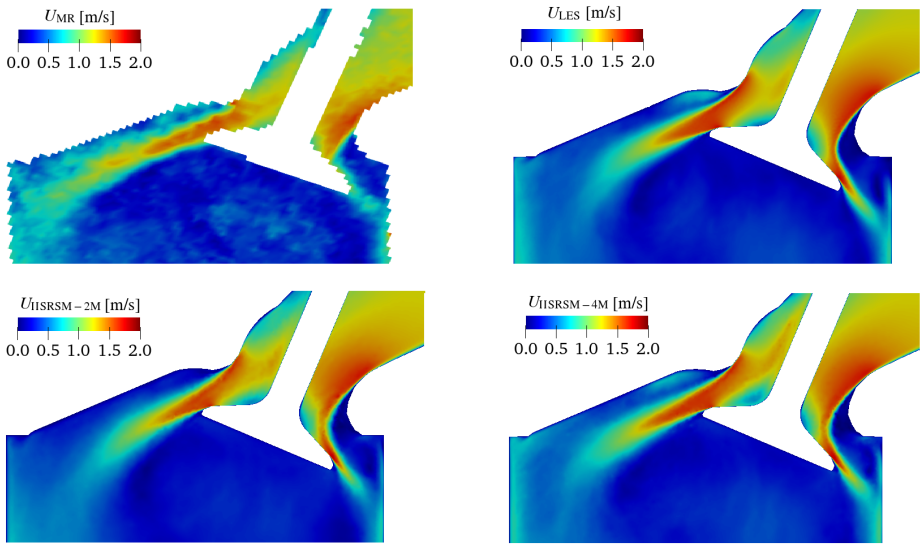

Figure 5.8.: Time-averaged velocity field on the valve plane of the TUDa Flowbench configuration obtained by the scale-resolving IISRSM and LES on the corresponding 2.3, 4 and 8 million cells finite volume mesh in comparison with the experimentally obtained MRV velocity field.

Fig. 5.8 contains the time-averaged velocity fields sampled from the MRV experiment, the corresponding LES and both scale-resolving URANS simulations with 2.3 and 4 million cells. The velocity field data is extracted at the previously mentioned

valve plane, cutting through the center point of the respective valve. All simulations are able to qualitatively and quantitatively reproduce the important large scale flow structures seen in the MRV measurements. The simulations correctly predict the re-circulation vertices beneath the valve plate which are commonly known as the tumble motion of an IC engine intake flow (Hill and Zhang, 1994). Compared to the time-averaged flow structure of the LES and scale-resolving URANS simulations, it is possible to observe higher velocities and a less diffusive valve jet stream for the MRV experiment when compared to the numerical simulations. However, the experimental MRV data shows local fluctuations which can be an indication that the time-averaging process of the magnetic resonance velocimetry averaging is not fully completed. Beside that, all simulations are capable of capturing even smaller flow phenomena like e.g. the impingement's of the valve jets onto the cylinder walls.

A more detailed analysis of time-averaged flow quantities is additionally performed by utilizing the so-called valve curtain. The valve curtain is an annular, closed lateral surface which originates on top of the valve with a height of the opened valve distance. All mass entering the combustion chamber is passing through this projected area. Analysing the valve curtain makes it possible to capture the whole complex flow field into the combustion chamber and its corresponding flow features at once.

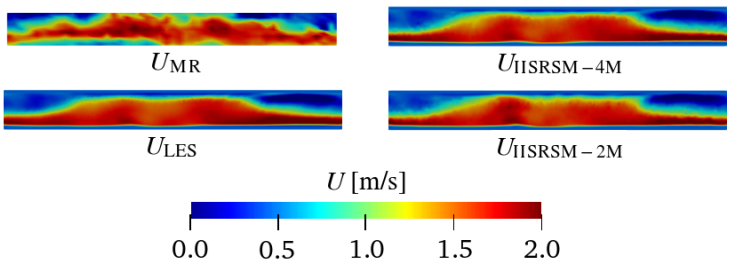

Figure 5.9.: Mean velocity field on the valve curtain obtained by the MRV, LES and scale-resolving IISRSM.

Fig. 5.9 shows the experimental and numerical plane-normal, mean velocity magnitude through the valve curtain. The LES and both eddy-resolving URANS simulations show high levels of similarity over the projected area. However, the MRV differs significantly from all simulations in terms of smoothness and still shows signs of turbulent fluctuation. The experimental data therefore again indicates a not fully completed time-averaging process within this highly turbulent flow regime.

For a better qualitatively comparison, Fig. 5.10 shows the different experimentally and numerically obtained velocity magnitudes along two orthogonal lines directly beneath the valves within the local, cartesian x and z direction. The LES and both

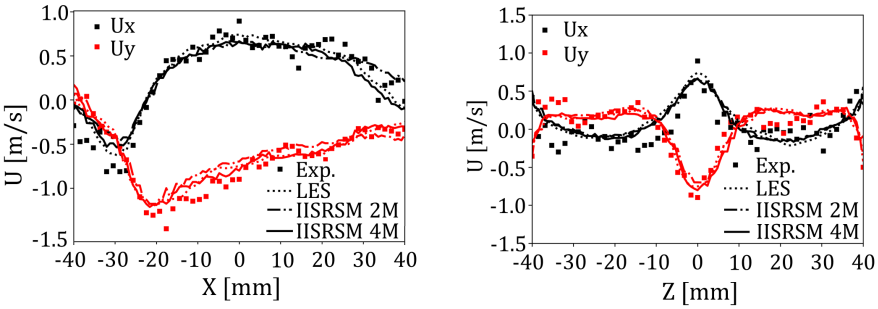

Figure 5.10.: Time-averaged profiles of the velocity components U_x and U_y parallel to the x and z axis at the absolute position of 10 mm below the valve indicated by the white dashed line in Fig. 5.6, evaluated along the red marked lines 1 and 2.

scale-resolving URANS simulations show similar results along all directions and are also closely following the noisier MRV data. It is especially notable that both URANS simulations, performed on significantly differing grid sizes are in quantitatively close agreement to each other and the corresponding LES respectively. The grid spacing free model formulation of the IISRSM enables the usage of coarse numerical grids when compared to an LES but still maintain its eddy-resolving properties. However, the experimental MRV data once again exhibits signs of turbulent fluctuations which indicates a not fully completed time-averaging process.

The next step within the validation process is the comparison of the corresponding turbulent quantities. The experimental data in this case is limited to the previously analyzed time-averaged velocity fields and does not contain further turbulent information. Therefore, the upcoming comparisons are only performed between the numerical results of the reference LES and the corresponding scale-resolving URANS simulations, respectively.
Fig. 5.11 shows the turbulence kinetic energy $k = 0.5\overline{u\prime_i u\prime_i}$ normalized by the squared mean bulk inlet velocity at the valve plane for the LES and the scale-resolving URANS simulations. The URANS simulations exhibit a slightly higher turbulent activity around the valve jets and the corresponding impingement regions in comparison to the LES results. Its also noticeable that both URANS simulations are more diffuse around the valve jets due to their coarser numerical grids. The difference in grid size can especially be noticed when comparing the center region of the upper right valve jet. The LES shows a sharp separation of the upper and lower shear layer whereas the URANS simulations predict a more diffuse and higher momentum transport in this regions. When comparing the URANS simulations performed on the 2 million and 4 million cells meshes, the only significant difference occurs within the forming of the upper right shear

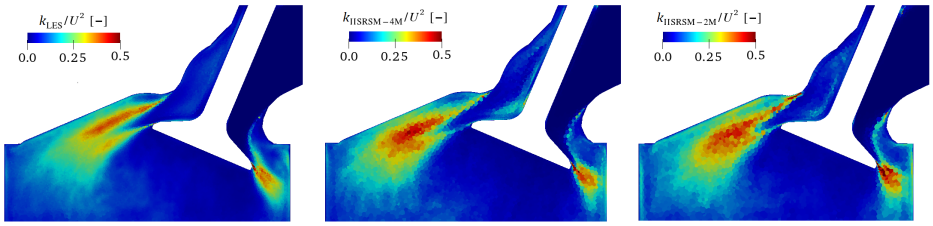

Figure 5.11.: Total turbulence kinetic energy k_{tot} normalized by the bulk inlet velocity U_b for the LES and IISRSM simulations within the valve plane of the TUDa Flowbench configuration.

layer of the bigger valve jet. The results obtained on the 2 million cells mesh show higher levels of turbulence directly originating form the separation point. Subsequently, all numerical results are, despite the discussed minor differences, in outstandingly good agreement and show high levels of similarity.

As previously mentioned, a further characteristic of turbulent flows is the turbulence anisotropy, which can be directly visualized. In the present work, a proper prediction of the turbulence anisotropy is essential for an accurate numerical prediction of the internal flow within the complex Flowbench geometry. Various properties of the Reynolds stress anisotropy tensor can be utilized to later enhance modeling strategies. The present work focuses on the visualization of the Reynolds stress anisotropy tensor as introduced in section 3.1. There are only a few visualization techniques for second-order tensor fields, like glyphs or hyperstreamlines (see Hashash, Yao, and Wotring (2003)). Due to their complex construction and difficult interpretation, none of these techniques has been established for broad use. Instead derived quantities according to Emory and Iaccarino (2014) are used to investigate anisotropic behavior of the flow, which compresses the contained information of a second-order tensor to either scalar or vector metrics.
Figure 5.12 presents the time-averaged two componentality parameter within the valve plane of the TUDa Flowbench configuration obtained by the LES and scale-resolving IISRSM. The two componentality parameter $A = 1 - 9/8(A_2 - A_3)$, as a well known approach for visualizing turbulence anisotropy in a spatial domain, gives information about the general anisotropic turbulent state within a physical domain. If $A = 1$ the turbulent state can be considered isotropic, if $A < 1$ it anisotropic. Therefore the two componentality parameter only provides information about the level of anisotropy of a given Reynolds stress field but does not contain information about the exact anisotropic turbulent state. The comparison between the LES- and RANS-RSM-related two componentality parameter fields in 5.12 reveals a fundamentally equal anisotropic state between the LES and scale-resolving RANS simulations. All simulations indicate a highly

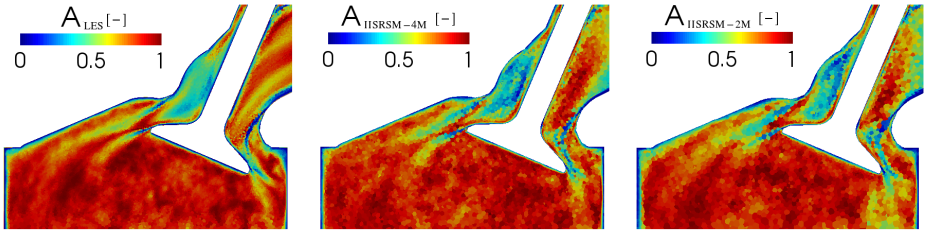

Figure 5.12.: Comparative assesment of the time-averaged two componentality parameter $A = 1 - 9/8(A_2 - A_3)$ within the valve plane of the TUDa Flowbench configuration obtained by the LES and scale-resolving IISRSM.

anisotropic turbulent state within the intake and above, but a nearly isotropic state beneath the valves. Since the intake design of an internal combustion engine is heavily motivated by achieving a homogeneous mixing of fresh air and the injected gasoline spray, the underlying turbulent transport processes should also exhibit an almost isotropic character. All respective simulations clearly show this intended isotropic turbulent state within the combustion chamber.

A further more advanced technique which is also based on the eigenvalues λ_i and has been previously introduced is Sec. 3.1 utilizes the barycentric map of Banerjee, Krahl, Durst, and Zenger (2007). The Barycentric map shown in Fig. 3.5 uses the fact that any turbulent state can be described as a combination of the three limiting turbulent states (corners). The tree limiting turbulent states are one-,two- and three-componental marked as x_{1_C}, x_{2_C}, and x_{3_C}.

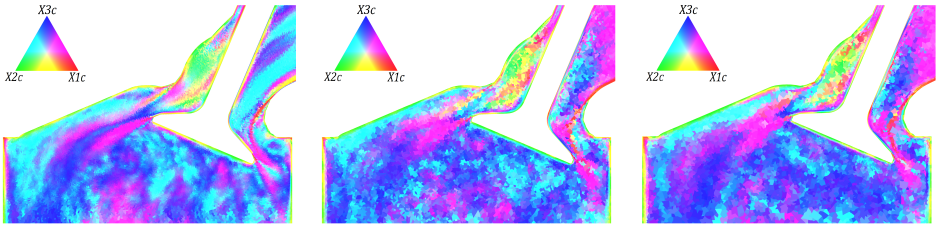

Figure 5.13.: LES- (left) and the IISRSM-related cell coloring of the time-averaged barycentric coloring for the corresponding 4m (middle) and 2.3m (right) cells finite volume meshes in the valve plane of the TUDa Flowbench configuration.

Leveraging the characteristics of the barycentric anisotropy map and convey its information back to the real computational domain by color-coding the turbulent states as previously introduced in chapter 3.1 the so generated cell coloring of figure 5.13 provides a profound insight into the anisotropic turbulent states within the valve plane of the Flowbench configuration. When comparing the two componentality parameter, depicted in Fig. 5.12 and the barycentric color-coded fields of figure 5.13 it is important to notice that the dark red regimes within the two-componentality fields are perfectly correlating with the corresponding dark blue regimes within the barycentric color-coded field plots. This shows that both methods reliably identify regimes of three componental isotropic turbulence. By further utilizing the barycentric color-coded visualization technique, several characteristic flow phenomena can be identified within the present valve cutting plane. Following the inflow over the valve, a collision of the fluid flowing around the valve stem can be detected by a characteristic color shift from pure blue (isotropic three componental turbulence X_{c3}) or magenta before the valve stem to green (axisymmetric two componental turbulence X_{c2}) after the valve stem. It is important to notice that the scale-resolving IISRSM correctly predicts the anisotropic turbulent state around the valve stem when compared to the reference LES. Further, the scale-resolving RANS-RSM based IISRSM correctly predicts the turbulent state within the flow regime of strong acceleration at the edge of the valves, which is characterized by a color shift into magenta and subsequent also dark red (One componental turbulence - X_{c1}). When evaluating the highly sensitive barycentric coloring of the underlying anisotropic turbulent states, the overall accordance of the scale-resolving IISRSM with the corresponding reference LES is remarkable.

In summary, the present section addresses the validation of the eddy-resolving Improved Instability Sensitive Reynolds Stress Model (IISRSM) on a complex Internal Combustion engine intake flow. The IISRSM turbulence model is presented as a second-moment closure Reynolds stress model with a sensitivation towards LES-like fluctuation. The turbulence model and its corresponding framework is implemented in the Finite-Volume-Method open-source toolbox OpenFOAM version 2.4.x. The meshing of the Flowbench geometry for all numerical simulations is realized by the pre-processing software ANSA. Two different grid sizes with 2.3 and 4 million finite volume cells for the scale-resolving URANS simulations and 8 million cells for the Large Eddy Simulation are presented. To ensure a sufficient mesh quality, a priori analyses are performed to every numerical grid. The resulting URANS simulations are held against a Magnetic Resonance Velocimetry (MRV) and the corresponding LES. The comparison shows that the URANS simulations on both grids correctly predict the general structure of the intake flow, especially in term of flow detachment from the valve and the subsequently developing tumble motion within the combustion chamber. The instantaneous flow fields of both URANS simulations show similar

eddy-resolving characteristic according to the baseline LES. This indicates that the IISRSM model is capable of correctly capturing the unsteady nature of the complex flow within the investigated Flowbench geometry, but with up to 60% less computational cost compared to an LES. Further comparisons of the total Reynolds stress fields and the corresponding Reynolds stress anisotropy also showing similar behaviour over the whole flow domain. Concluding all comparisons the eddy-resolving IISRSM is capable of correctly reproducing the complex flow within the Flowbench geometry in comparison to the baseline LES and the experimental MRV data by reducing the necessary computing effort by 60%.

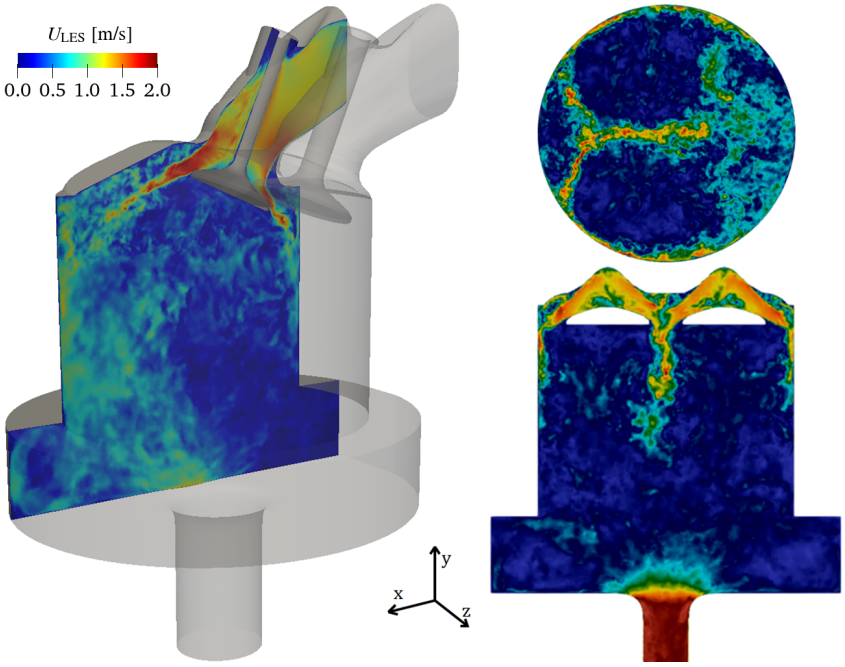

Figure 5.14.: Full rendering (left) of the TUDa Flowbench, its collision plane (bottom right) and its top plane (top right) colored by the time-resolved, fluctuating, instantaneous velocity field of the reference LES.

Based of the results of the stationary Flowbench with its fixed valve and piston positions addressed in the current section, the scale-resolving IISRSM will, from here on be further investigated in two derived generic flow configurations. The first further generic flow configuration is focusing the impingement processes of the previously shown valve jets (See Fig. 5.14) with inclusion of a passive, scalar temperature transport equation into the numerical setup (Sec. 5.2). An additional

focus to in this investigation is the modeling of the turbulent heat flux $\overline{u_i \theta_j}$ (See, Sec. 2.4.3) which additionally appears within the Reynolds-averaged temperature equation (Eqn. 2.14) similarly to the Reynolds stress tensor $\overline{u_i u_j}$ in the Reynolds-averaged momentum equation (Eqn. 2.13) . The second generic flow configuration, derived from the present Flowbench setup addresses the jets collision and wall-perpendicular mixing, seen in the additional slices of Fig. 5.14 within a double-slot jet impingement configuration (Sec. 5.3).

5.2. Axis-symmetric Impining Jet (ASIJ)

Case setup

The flow configuration considered within the present section resembles a circular jet impinging perpendicularly onto a heated wall. The jet structure corresponds to a fully-developed pipe flow at a diameter-based Reynolds number of $Re = 10000$. Reference DNS data are made available by Secchi, Häber, Gatti, Schulz, Trimis, Suntz, and Frohnapfel (2022) and Secchi, Gatti, and Frohnapfel (2023). The turbulent round jet entering the flow domain is realized by a separate calculation of a pipe segment using the periodic inlet/outlet conditions. The flow field generated in this way is then mapped onto the domain inlet. The jet impinges perpendicularly on a partially heated wall located at $2D$ distance from the pipe outlet, with boundary conditions corresponding to a constant wall temperature.

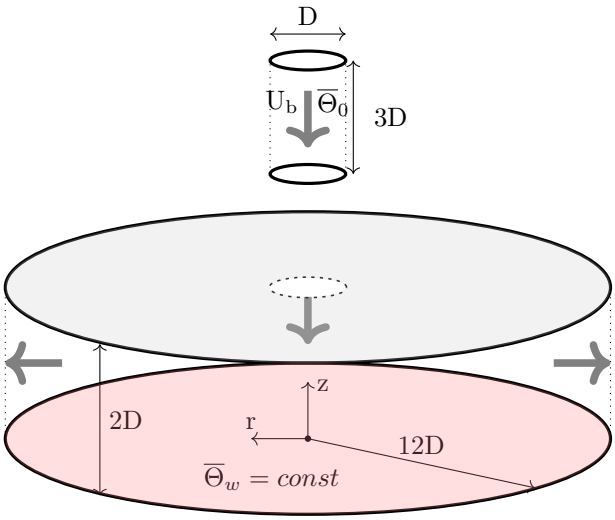

Figure 5.15.: Schematic representation of the solution domain for the round-jet impingement at a bulk Reynolds number $Re_\mathrm{b} = 10000$ onto a heated wall with a nozzle-plate distance of H/D = 2.

Figure 5.15 shows the schematic of the solution domain accommodating the round impinging jet configuration. Its cylindrical shape is bounded by the lower impingement wall and an upper bounding plate in the normal direction and extends in the radial direction to $12D$. The number of cells in the radial plane of $N_r = 46400$ multiplied by the number of cells in the normal z-direction $N_z = 138$ gives a total of 6.4 million cells. The height of the grid cells adjacent to the wall over the entire simulation domain is $\Delta z^+ = 0.06 - 0.94$. The lower values refer to the immediate

impinging area and the higher values to the region near the configuration outlet. The grid resolution in the radial direction corresponds to $\Delta r^+ = 4.76 - 139.54$, following the analogous grading from the impinging center to the configuration outlet. The same three-dimensional solution region and grid resolution were used for both the steady conventional RANS and the time-accurate sensitized RANS simulations.

Results and Discussion

In this section, results of the comparative evaluation of the different modeling approaches introduced in section 2.4.3 for the mean flow and thermal field properties and associated Reynolds stress tensor $\overline{u\prime_i u\prime_j}$ and the turbulent heat flux $\overline{u\prime_i \theta\prime}$ are presented for the introduced axisymmetric impinging jet flow configurations. To get a first impression about the basic structural characteristics of the discussed flow case, Figure 5.16 visualizes the instantaneous velocity and temperature fields by showing their iso-contours as well as the vortical structures represented in accordance with the Q-criterion.

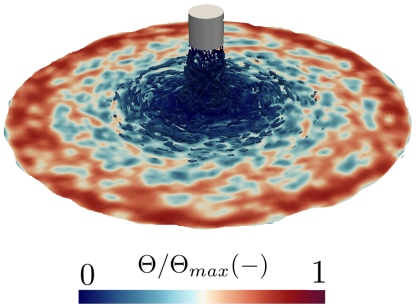

Figure 5.16.: Flow visualization by the Q-criterion, colored by the non-dimensionalized instantaneous temperature field ($\overline{\Theta}/\overline{\Theta}_{\max}$) obtained by the IISRSM in a round impinging jet with fixed wall temperature.

The results presented illustrate clearly the capability of the IISRSM to resolve the turbulent fluctuations with respect to both velocity- and temperature fields. Their dynamics are mainly governed by their resolved fractions, whose generation is driven by the convective terms in the corresponding transport equations (Eqn 2.13 & 2.14). However, in the wall proximity, the sub-scale turbulent momentum and heat fluxes are appropriately enhanced and are therefore crucial for the correct capturing of the near-wall effects. In the following, some time-averaged mean flow and turbulence characteristics are discussed along with the DNS reference results. This section in particular examines the outcomes derived from the computation of a round jet, which exhibits structural characteristics similar to a fully-developed

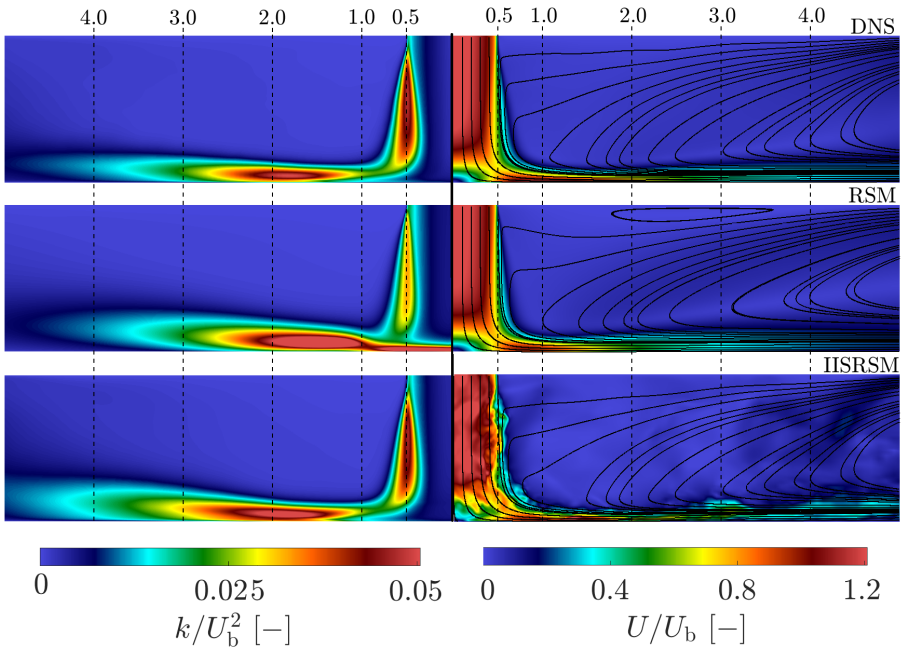

Figure 5.17.: Time-averaged DNS- (top) and RANS-RSM-related (middle) iso-contours and instantaneous IISRSM-related (bottom) velocity fields with their respective corresponding mean streamlines (right) and the corresponding time-averaged turbulence kinetic energy (left) in the central $(r-z)$ vertical plane of the round-jet impingement configuration.

pipe flow, impinging on a heated surface. The analysis compares the results obtained using the baseline RSM (Eqn. 2.4.2) and its eddy-resolving version, the IISRSM (Eqn. 2.4.2), in combination with closures for heat-flux modeling introduced in section 2.4.3. The analysis is made with reference to the DNS database provided by Secchi, Gatti, and Frohnapfel (2023).

The global flow topology visualized in Figure 5.17 (left) is qualitatively similar to that studied in the previously discussed slot-jet impingement (Sec. 4.2). Accordingly, the description of the flow characteristics provided with reference to Figure 4.8 can be applied here as well. Compared to the planar slot-jet impingement, the present round-jet impingement takes place at a twice higher Reynolds number of $Re_D = 10000$ (based on pipe diameter and bulk velocity). The round jet deflects radially at the bottom wall after impingement. Spreading radially over the heated

wall, in addition to all the flow strains discussed previously for the slot-jet impingement, the flow in the impingement region experiences a transverse shear of a certain intensity in the azimuthal direction, which varies slightly with increasing distance from the impingement center. This feature represents an additional difficulty for RANS-related modeling strategies in comparison with the planar impinging jet. Another important difference corresponds to the abruptly decelerated jet stream at the point of impingement. The area of confined low-velocity backflow is much smaller for the round impinging jet (Fig. 5.17) compared to a correspondingly extended region observed for the planar slot-jet impingement (Fig. 4.8). As a consequence of the circular propagation of the flow after impact, the mass flow of the incoming jet is distributed over the entire plate, which results in a thin wall-jet with low velocity, Fig. 5.17. On the other hand, the shear layer aligned with the mean streamline bounding the wall-jet is somewhat wider than for planar impingement (about twice the wall-jet width). With increasing radial distance, the axial wall-parallel momentum of the wall jet weakens and consequently more momentum is transported into the upper part of the flow domain.

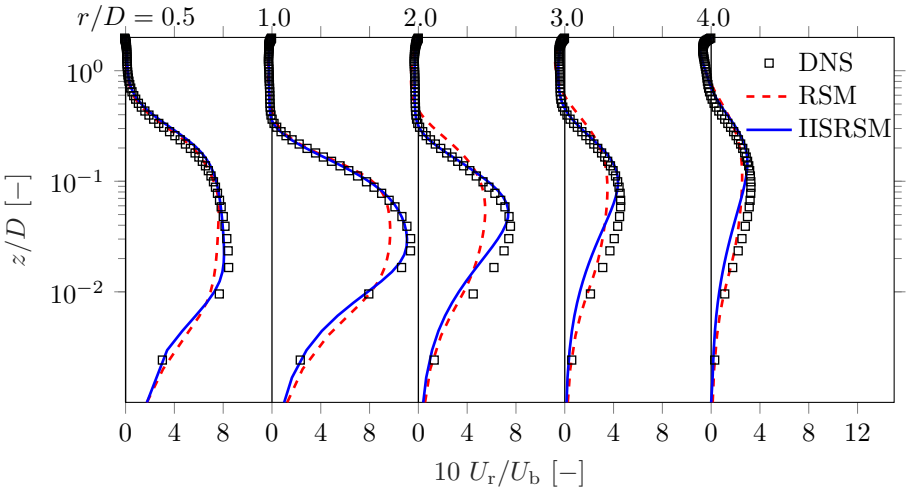

Figure 5.18.: Profile development of the horizontal velocity component (U_r/U_b) in the radial direction in the round-jet impingement configuration.

Fig. 5.18 shows the profile development of the radial mean velocity U_r/U_b at five selected positions $r/D = 0.5, 1.0, 2.0, 3.0$ and 4.0. The wall-normal dimensionless coordinate z/D is plotted on a logarithmic scale to emphasize the near-wall behavior. The corresponding velocity profiles are characterized by an intensification of the flow momentum that occurs during the impingement event (at $r/D = 0.5 - 1.0$) and the subsequent transition (at $r/D \geq 1.0$) to the wall jet. Thereafter, the flow momentum decreases. Immediately after the impingement at $r/D = 1$, the

experimental and both computational results are in good agreement. In particular, the agreement of the results obtained by the scale-resolving IISRSM with the DNS database at the central area of impingement is remarkable. The RSM-related results also show a physically reasonable level of agreement with DNS. Further downstream, at the radial positions $r/D \geq 1$, the RSM results exhibit more pronounced deviations from the DNS database then the results determined by the scale-resolving IISRSM. It is noticeable that the boundary layer formation shows significant differences between the two RANS-based models. Due to the upper confinement plane, a weak intensity back flow is generated above the wall jet region, similar to the flow configuration previously investigated, which is indicated by negative velocity values.

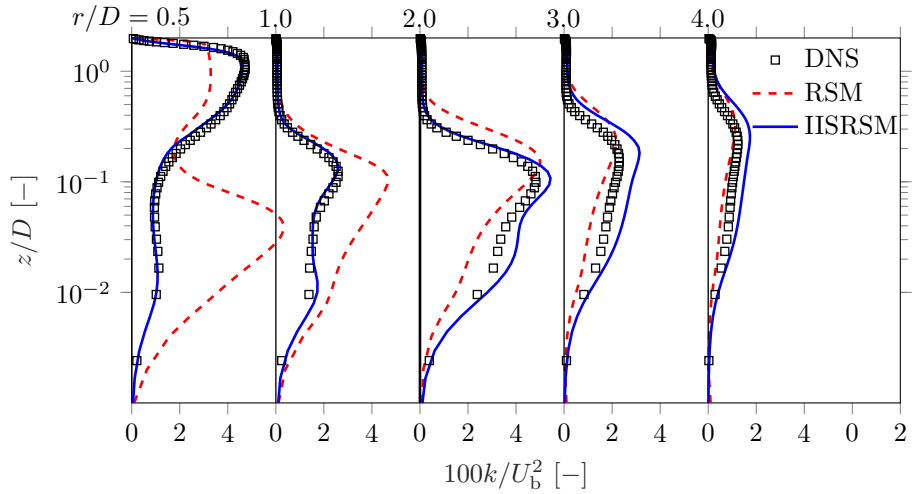

Figure 5.19.: Profile development of the turbulence kinetic energy (k/U_b^2) in the radial direction in the round-jet impingement configuration.

Analogous observations are presented in Fig. 5.19, showing the turbulence kinetic energy non-dimensionalized by the inlet bulk velocity k/U_b^2. As before, the dimensionless wall-normal coordinate z/D is plotted on a logarithmic scale to provide better insight into the the near-wall behavior. The agreement in profile shape and its magnitude between the turbulence kinetic energy predicted by the IISRSM in comparison with the DNS data is very good at all radial positions, except for the slight enhancement in the far wall-jet region. When comparing the RSM-related predictions to the reference DNS data, an enhanced, disproportionate production of turbulence kinetic energy can be observed in the vicinity of the impingement point at $r/D = 0.5$ and 1.0.

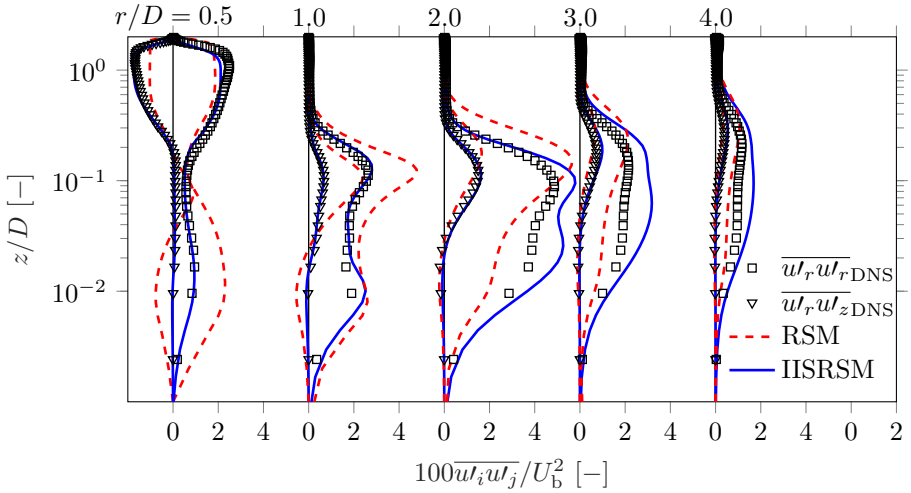

Figure 5.20.: Profile development of the radial ($\overline{u\prime_r u\prime_r}$) and shear ($\overline{u\prime_r u\prime_z}$) Reynolds stress components in the radial direction in the round-jet impingement configuration.

The radial (parallel to the impinging plate) $\overline{u\prime_r u\prime_r}$ and shear $\overline{u\prime_r u\prime_z}$ Reynolds stress components returned by the IISRSM closely follow the DNS database, Figures 5.20 and 5.21. At the cross-section $r/D = 0.5$, which coincides with the pipe outlet, the maxima of the turbulence kinetic energy and both stress components originate from the near wall region within the inflow pipe. The correctly predicted double maximum of the $\overline{u\prime_r u\prime_r}$ component and the turbulence kinetic energy, visible at $r/D = 0.5 - 2.0$, coincides with the wall-jet boundary, which is characterized by a velocity maximum at $z/D = 0.1$ and the strong mean shear in the immediate vicinity of the wall at $z/D = 0.01$. Additionally, the characteristic sign change of the shear stress component $\overline{u\prime_r u\prime_z}$ can be correctly captured in terms of both the location of this change and the corresponding magnitude. However, the baseline RSM substantially overestimates the turbulence production within the impingement region, resulting in the significantly overpredicted turbulence level seen at all Reynolds stress components. An analogous outcome can also be seen at the Reynolds stress profiles in the previous slot-related impingement configuration in section 4.2. This can be partially explained by the 'standard' expression of the so-called wall-reflection redistribution term withing the transport equation of the present RSM, which was originally formulated for wall-parallel flows as suggested in Craft, Graham, and Launder (1993). Moreover, the RSM-related results suggest that an excessive streamline curvature-induced turbulence production takes place here, inherently present in the Reynolds stress modeling concept. The strong local streamline curvature presently acts in a destabilizing manner, thus contributing

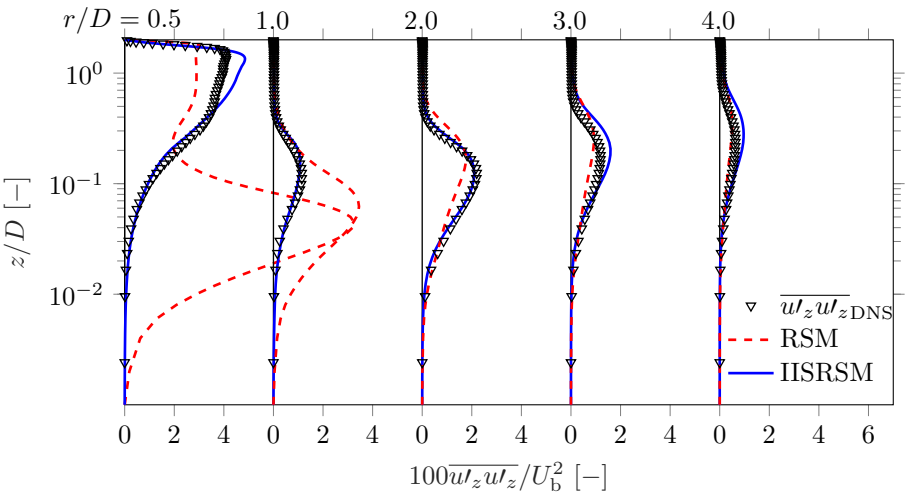

Figure 5.21.: Profile development of the wall-normal ($\overline{u'_z u'_z}$) Reynolds stress component in the radial direction in the round-jet impingement configuration.

to the turbulence level increase. On the other hand, it is worth noting that, considering the large deviation of the RSM-related turbulent kinetic energy, the overall good agreement of the mean flow velocity is mainly due to the role of the mean pressure gradient, which dominates the balance in the equation of motion, significantly overcoming the Reynolds stress gradients.

The evaluation of the Reynolds stress anisotropy tensor a_{ij} and its capability to further depict anisotropic momentum and temperature transport is, in the following analyzed by various comparative techniques for the present flow configuration. As introduced in section 3.1, the anisotropy triangle of Lumley and Newman (1977) firstly gives the important information about the general realizability of numerically predicted Reynolds stress fields. Figure 5.22 shows a comparative assessment of the anisotropy tensors second and third invariant (A_2 & A_3) for every underlying Reynolds stress tensor data point within the physical, computational domain of all respective numerical procedures and models. As expected the general realizability of all turbulent states of any considered numerical approach is given without exception. Its important to notice that the overall anisotropic states, predicted by the scale resolving IISRSM (blue) (chap. 2.4.2) seem to be in reasonable accordance to the reference DNS data, whereas the baseline RSM (red) suggests slightly differing results. Since the present, classical anisotropy triangle, originally suggested by Lumley and Newman (1977), delivers a narrow and non-linear

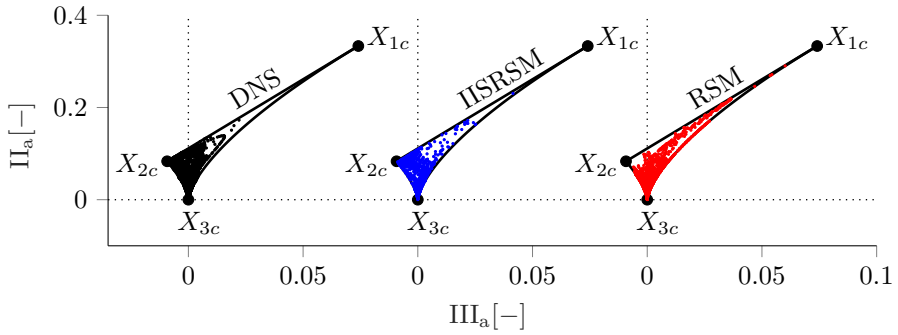

Figure 5.22.: Comparative assessment of the anisotropy tensors second and third invariant (II_a & III_a) for every data point of the computational axisymmetric impinging jet configuration domain obtained by the reference DNS, scale-resolving IISRSM and baseline RSM.

domain it is worth considering the linear barycentric anisotropy triangle for further analysis of the general anisotropic turbulent states across the entire physical domain.

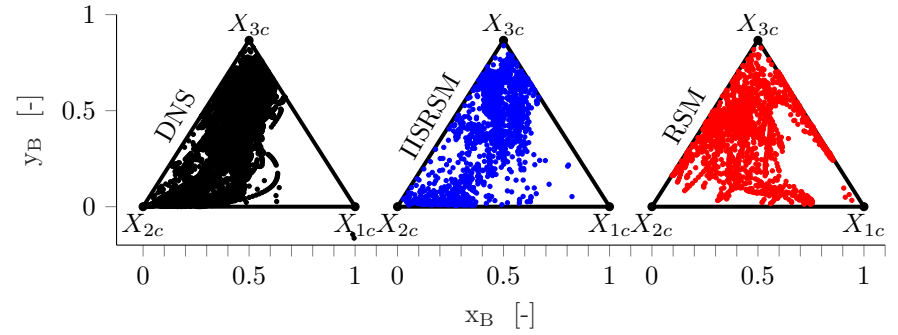

Figure 5.23.: Comparative assessment of the barycentric coordinated $x_B(a_{ij})$ and $y_B(a_{ij})$ for every data point of the computational axisymmetric impinging jet configuration domain obtained by the reference DNS, scale-resolving IISRSM and baseline RSM.

The turbulent anisotropic states of the IISRSM, RSM and reference DNS, displayed within the previously introduced linear barycentric map (Chap. 3.1) are shown in Figure 5.23. The linear barycentric domain clearly enhances the analytical capabilities compared to the nonlinear domains of figure 5.22. As suggested in advance, the general anisotropic turbulent state predicted by the scale resolving

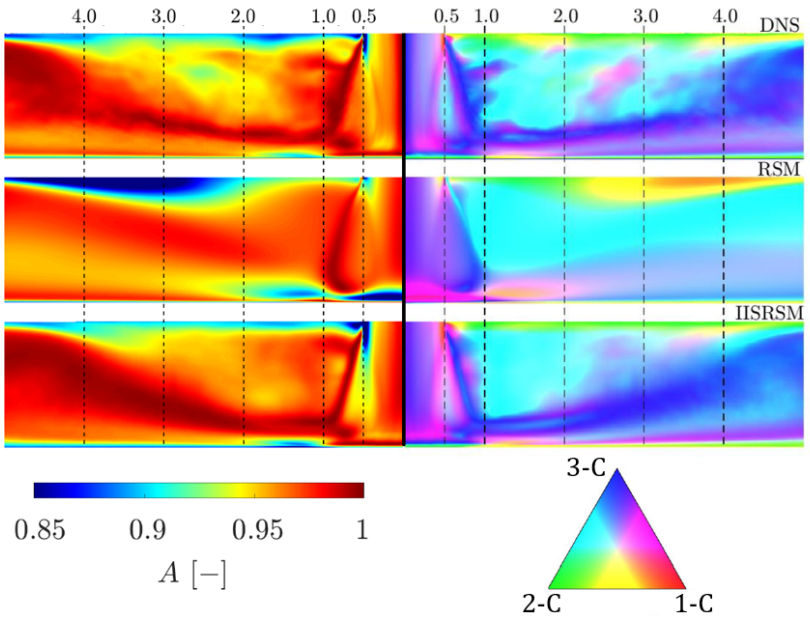

Figure 5.24.: DNS- (top) and RANS-RSM-related (middle) and IISRSM-related (bottom) iso-contours of the time-averaged two componentality parameter A (left) and time averaged barycentric coloring (right) in the central $(r-z)$ vertical plane in the round-jet impingement configuration.

IISRSM is in overall good agreement with the DNS data, clustering between two- and three-dimensional turbulence states whereas the baseline RSM exhibits a more pronounced overall deviation, extending more towards 1D turbulence states.

Since the evaluation of anisotropy-related point clouds of an entire physical domain as seen in Figs. 5.22 and 5.23, with no further information about the actual corresponding physical locations does not reveal enough detail to elaborate a proper comparative assessment, the barycentric coordinates of figure 5.23 can be utilized to remap the anisotropic turbulent state contained in the corresponding coordinates x_B and y_B to the actual physical domain. The applied visualization method for the barycentric coordinates is found in section 3.1.
Figure 5.24 presents the time-averaged two componentality parameter (left) and the Reynolds stress anisotropy componentality contours (right) of the round-jet impingement configuration obtained by the DNS, IISRSM and RSM. The two componentality parameter $A = 1 - 9/8(\mathrm{A}_2 - \mathrm{A}_3)$, as a well known approach for visualizing turbulence anisotropy in a spatial domain, gives information about

the general anisotropic turbulent state within a physical domain. If $A = 1$ the turbulent state can be considered isotropic, if $A < 1$ it is non-isotropic. Therefore the two componentality parameter only provides information about the level of unisotropy of a given Reynolds stress field but does not contain information about the exact unisotropic turbulent state. It is however clearly visible that the unisotropic state, depicted by the two componentality parameter in Fig. 5.24(left) varies between DNS, RSM and IISRSM predictions. While the scale resolving IISRSM is capable to properly predict the unisotropic state in comparison to the reference DNS data, the RANS-based RSM shows significant deviation within vicinity to the impingement point at $r/D = 0$ up to $r/D = 2$. Hereby the most notable differences are found in immediate wall vicinity around the impingement point and the shear layers of the wall perpendicular as well as the wall parallel jets. The RANS-RSM related predictions suggest a highly anisotropic turbulent state at the central high pressure stagnation point which is a subsequent result of the overestimation of the wall normal Reynolds stress component seen in figure 5.21. The pronounced near wall peak of the $\overline{u\prime_z u\prime_z}$ stress component directly leads to a significantly distorted two componentality at the stagnation point. Leveraging the characteristics of the barycentric anisotropy map in figure 5.23 and transfer its information back to the physical domain by color-coding the turbulent states as previously introduced in chapter 3.1 the so generated iso-contours of figure 5.24 (right) provides an enhanced insight into the unisotropic turbulent state of the round jet impingement. By directly comparing the two componentality and color-coded barycentric coordinate fields of figure 5.24 it is important to notice that the dark red regimes within the two-componentality fields (left) are perfectly correlating with the corresponding dark blue regimes within the barycentric color-coded field plots (right); which shows that both methods reliably identify regimes of three componental isotropic turbulence. By further utilizing the barycentic color-coded visualization technique, several characteristic flow phenomena can be identified within the round-jet impingement. Following the stagnation streamline on the center line of the impinging jet, a flow deceleration characterized by a color shift from pure blue (isotropic three componental turbulence X_{c3}) to cyan and a subsequent axisymmetric compression in immediate wall vicinity, characterized by a color shift from blue (X_{c3}) to green (axisymmetric two componental turbulence X_{c2}) are correctly predicted by the scale resolving IISRSM when compared to the reference DNS data. An additional, by both RANS-realted models, correctly predicted flow feature, is the strong acceleration at the edge of the nozzle exit at ($r/D = 0.5$ and $z/D = 2.0$), which is characterized by a color shift into dark red (One componental turbulence - X_{c1}). When evaluating the highly sensitive barycentric coloring of the underlying anisotropic turbulent states, the overall accordance of the scale-resolving IISRSM with the corresponding reference DNS is remarkable.

To facilitate a more detailed evaluation of the above discussed two-componentality parameter A as well as the color-coded barycentric coordinates x_B and y_B, both methods are evaluated along the previously utilized vertical lines at the dimensionless radial positions $r/D = 0.5$, 1.0, 2.0, 3.0 and 4.0 in the r-z plane of the impinging round-jet configuration.

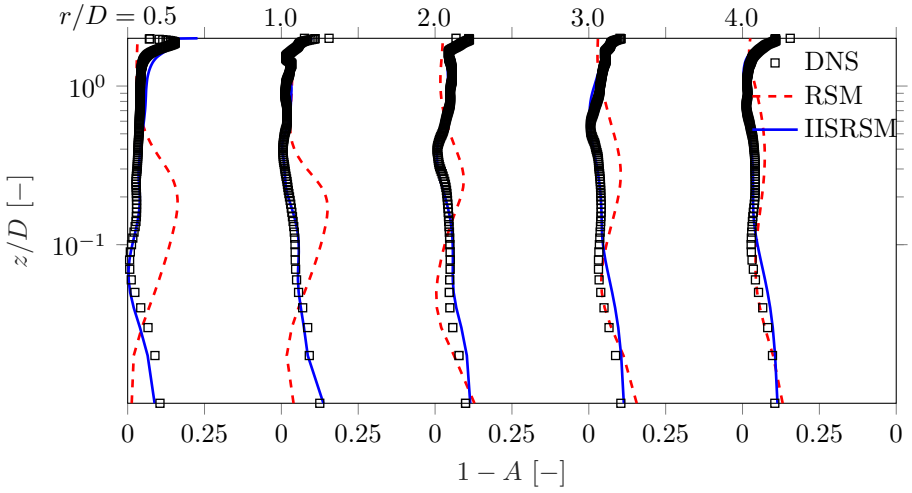

Figure 5.25.: Profile evolution of the 1-A (two-componantality parameter) in different radial positions $r/D = 0.5$, 1.0, 2.0, 3.0 and 4.0 within the r-z-plane of the round-jet impingement configuration.

As suggested by the field evaluation of the two-componentality parameter in Fig. 5.24 the profile evolution of 1-A, shown in Fig. 5.25, indicates a significantly better predicting capability in terms of general Reynolds stress anisotropy for the scale-resolving IISRSM, when compared to the baseline RSM. It is worth noticing that the predicted radial evolution of A obtained by the IISRSM almost perfectly matches the reference DNS data.

The most detailed comparative assessment addressing the predictive capabilities in terms of anisotropic turbulent behaviour across the radial direction of the round-jet impingement, utilizing the barycentric map is shown in Figure 5.26. Here the trajectory evolution of the barycentric coordinates obtained by the reference DNS, IISRSM and RSM is evaluated at the radial positions $r/D = 0.5$, 1.0, 2.0, 3.0 and 4.0. An interesting special feature of all trajectories obtained by the DNS and IISRSM is that they start and end in vicinity to the two-component axisymmetric limit X_{c2} as the wall normal Reynolds stress component $\overline{u'_z u'_z}$ drops to zero in immediate wall vicinity (Figure 5.21). While the scale-resolving IISRSM shows a high level of accordance to the DNS data at all five evaluated radial positions,

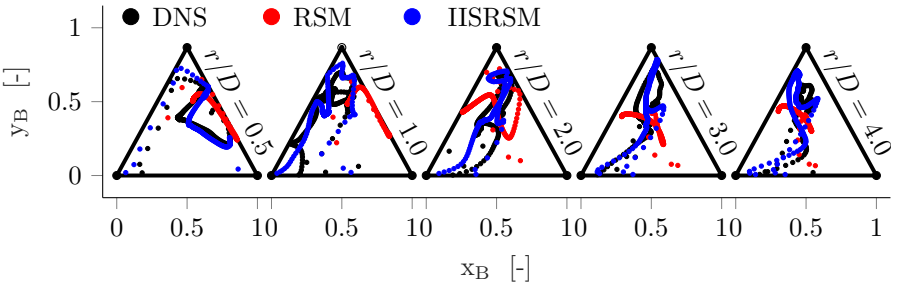

Figure 5.26.: Trajectory evolution of the barycentric coordinates obtained by the reference DNS, IISRSM and RSM at the radial positions $r/D = 0.5$, 1.0, 2.0, 3.0 and 4.0 within the r-z-plane of the round-jet impingement configuration.

the baseline RSM exhibits significant deviations. On the other hand, it is again worth noting that, considering the large deviation of the RSM-related turbulent kinetic energy in Fig. 5.19 and the subsequent significantly deviating anisotropy of turbulent states, the overall mean flow velocity is in good accordance to the DNS data. This circumstance mainly originates from the substantial role of the mean pressure gradient dominating the momentum transport in the equation of motion and significantly overcoming the influence of gradients of the resulting turbulent stresses $\overline{u\prime_i u\prime_j}$.

Since the velocity field obtained by both RANS-based Reynolds stress models demonstrates a high level of agreement, the evolution of the friction coefficient at the bottom wall, as depicted in Figure 5.27 is subsequently almost identical. When comparing the numerically determined friction coefficients, it is observed that both models are capable of accurately predicting the maximum value of the friction coefficient at the impingement region. This peak value is associated with the intense local flow acceleration at the transition onset toward the wall-jet. However, there are notable differences in the predicted downstream evolution compared to the DNS reference data. Neither the RSM nor the IISRSM adequately capture the characteristic wave-like progression observed at a dimensionless distance of $x/D = 2$, although a slight tendency toward this elevated behavior can be recognized on the IISRSM-relevant C_f evolution.

Fig. 5.28 illustrates the non-dimensional temperature profiles obtained by performing the RSM and IISRSM-related simulations. The performance difference among the tested heat-flux models is clearly visible in these profiles. Specifically, the temperature profiles obtained from the IISRSM-GGDH simulation closely match the data from DNS (a similarly good agreement was achieved when

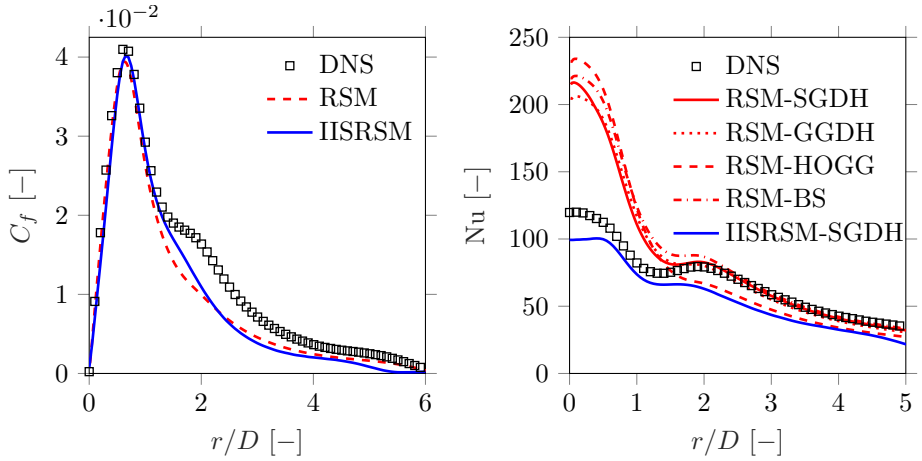

Figure 5.27.: Friction coefficient C_f (left) and Nusselt number distribution (right) at the impingement wall over the dimensionless radius r/D within the r-z-plane of the round-jet impingement configuration.

using the SGDH model for the heat flux). It is noteworthy that the IISRSM exhibits a significantly better capability to reproduce the near-wall temperature gradient compared to the baseline RSM model. The difference between the scale-resolving and the baseline RANS models becomes particularly pronounced near the impact point at $x/D = 0.5$. While analyzing the temperature profiles, no clear superiority of any specific heat-flux model emerges. However, it is crucial to accurately capture the temperature gradient in the vicinity of the bottom wall for an accurate estimation of convective heat transfer. The near-wall temperature gradients obtained with the IISRSM align very well with the DNS-related gradients. This alignment holds significance as even slight differences in the wall temperature gradients directly impact the distribution of the Nusselt number and can significantly influence near-wall heat transfer phenomena.

Fig. 5.27 (right) shows the Nusselt number distribution at the heated bottom wall ($z/D = 0$) over the dimensionless radius r/D. Considering its direct proportionality to the dimensionless temperature gradient, it is clear that the accurate IISRSM-related prediction for the temperature field is directly transferred to the corresponding Nusselt number prediction. The results obtained from various heat flux models (formulated in Eqs. 2.30, 2.31, 2.32 and 2.34) applied to the Reynolds stress model (RSM) again exhibit a significant overprediction of the Nusselt number near the impingement center at $x/D = 0.0 - 1.5$. This discrepancy in magnitude between the Nusselt number peaks from the RSM and IISRSM simulations is attributed to the IISRSM's more accurate prediction of the

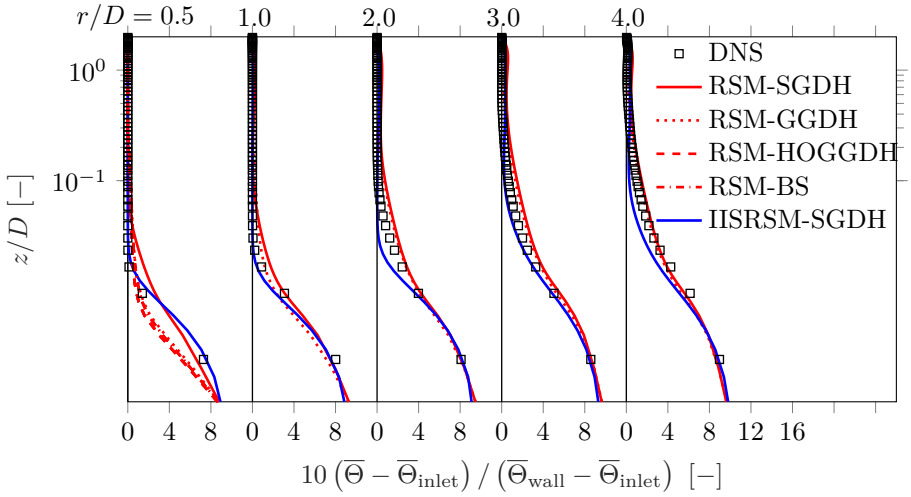

Figure 5.28.: Profile development of the temperature $\overline{\Theta}$ non-dimensionalized by the inlet and wall temperature $\overline{\Theta}_{\text{inlet}}$ and $\overline{\Theta}_{\text{wall}}$ in radial direction of the round-jet impingement configuration.

turbulent fields, as shown in Figures 5.20 and 5.21. It is important to note that the IISRSM in combination with the GGDH modeling approach for the turbulent heat-flux (similar outcome is detected when using the SGDH model) is capable to reproduce the characteristic second Nusselt number peak at $x/D = 2.0$, although exhibiting a slightly flattened behavior and a somewhat lower value compared to the reference DNS. Nevertheless, the IISRSM-specific underprediction requires a more detailed analysis, also in terms the grid resolution requirements. The RSM-relevant result obtained in conjunction with the GGDH (2.31), HOGGDH (2.32), and BS (2.34) models shows a corresponding reduction in the values of the Nusselt number, starting at the very elevated value at the impact center, until the value corresponding to the second peak of the Nusselt number was approximately reproduced. It is worth mentioning that the second Nusselt number peak phenomenon is somewhat less pronounced in the case of the axisymmetric impinging jet configuration ($Nu_{max}(x/D = 0.0) - Nu_{2nd} = 120 - 80$) compared to the previously studied slot-jet impingement with a nozzle-to-plate distance of $H/D = 0.5$ $(140 - 70)$.

Concluding the present chapter, the objective of the present study was to examine the predictive performance of the baseline Reynolds-Averaged Navier-Stokes Reynolds-Stress Model (RANS-RSM) and its eddy-resolving counterpart, referred to as Improved Instability-Sensitive Reynolds-Stress Model (IISRSM), employed within the Sensitized-RANS concept in comparison to a reference DNS database.

The numerical simulation of a turbulent axisymmetric jet impinging on a heated wall was evaluated by comparative assesments of the predictive performances of both RANS-RSM-related models with respect to their capabilities to correctly predict anisotropic momentum and heat transport processes. The baseline RSM in combination with the considered heat flow models yielded a reasonable distribution of the Nusselt number for radial distances $x/D \geq 2$ where a mean shear induced flow behavior dominates. However, similar to the previous configuration, within and around the immediate impingement region up to $x/D \leq 2$, significant over-prediction of the Nusselt number occurred due to more intense turbulence activity, exceeding by far the DNS-related results. In contrast, the scale-resolving IISRSM provided better predictions for velocity, Reynolds stress, and temperature profiles, closely following the DNS database. An exception is the resulting Nusselt number distribution, which showed a slight underprediction compared to the DNS reference data. A well-known feature of the latter global thermal field property, its second maximum characterizing the wall-jet development at higher impinging jet momentum (as specific to the round jet impingement considered here) and smaller nozzle-to-wall distances (relevant to the slot-jet impingement with $H/D = 0.5$), requires further analysis with respect to spatial and temporal resolution criteria in such wall-perpendicular flows.

In summary, this chapter provided the following important insights. In order to accurately predict the near-wall thermal field, a RANS-based model, whether in the conventional or sensitized RANS framework, must capture not only the velocity field but also the anisotropic turbulent stress tensor, especially within the impingement region and subsequently generated wall-jet characterized by variably oriented flow straining. Concerning a correspondingly enhanced turbulence level in this region pertinent to the baseline RANS-RSM, all tested heat-flux model formulations resulted in an excessive temperature gradient at the wall and a subsequently overestimated Nusselt number. However, further downstream in the region of the developed wall-jet, all models resulted in a reasonably well predicted thermal field. Accordingly, except for minor differences in model performance, no model emerged as significantly superior to the others. On the other hand, sensitizing a second-order Reynolds stress model to adequately resolve the fluctuating turbulence unsteadiness can significantly improve the prediction of the flow structure in terms of all dependent flow properties - velocity, Reynolds stress, and thermal fields - considering that a significant fraction of the turbulence has been resolved in this inherently highly unsteady flow region.

5.3. Double-Slot Impinging Jet (DSIJ)

Within the framework of the Simple-Gradient Diffusion Hypothesis (SGDH) paradigm (as shown in Equation 2.30), the eddy diffusivity Γ_Θ for modeling turbulent species transport is commonly represented in relation to the eddy viscosity ν_t and the constant turbulent Schmidt number Sc_t. However, the simplicity of eddy diffusivity models like Γ_Θ in Equation 2.30 is tied to a significant drawback. These scalar models primarily depend on scalar-field gradients, which poses a notable limitation. These models fail to consider unresolved turbulence anisotropy, inevitably leading to less accurate numerical predictions compared to more advanced modeling techniques.

This chapter aims to address this issue by focusing on second-moment Reynolds-Averaged Navier-Stokes (RANS) models and scale-resolving RANS models, coupled with various algebraic expressions for the correlation of turbulent species flux $-\overline{u\prime_j c\prime}$. The objective of this chapter is to perform a comprehensive evaluation of the combined predictive capabilities concerning near-wall velocity, Reynolds stress, species fields, and their impacts on associated mixing processes.

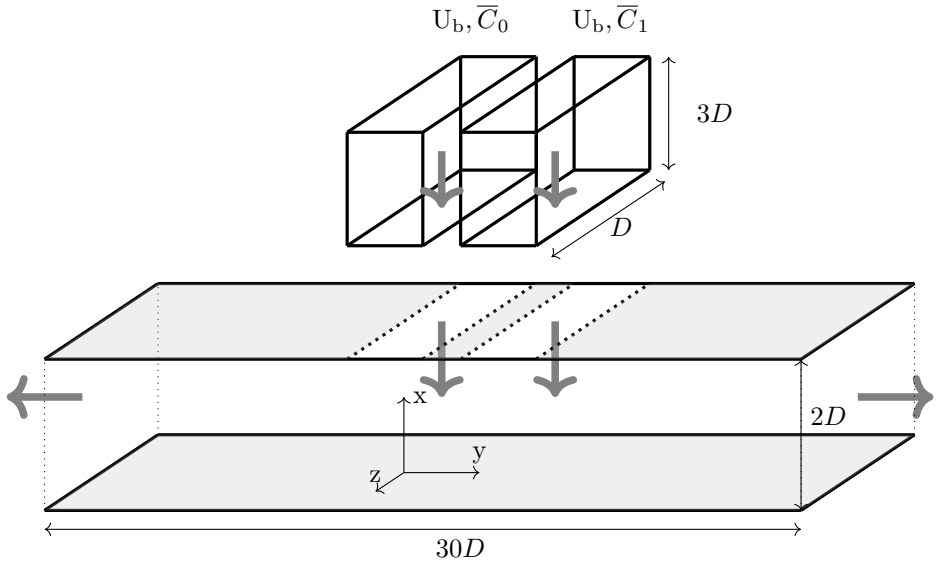

Figure 5.29.: Schematic drawing of the solution domain for the double slot impingement configuration with species transfer at a bulk Reynolds number of $Re_b = 10000$.

The flow configuration under investigation involves a double-slot impingement onto a planar wall. The geometry relevant to this study comprises two parallel, infinite channels that discharge perpendicularly into a horizontal confined space. All numerical simulations are conducted using an inflow condition characterized by $\mathrm{Re_b} = \mathrm{U_b D}/\nu = 10000$, where $\mathrm{U_b}$ represents the inlet bulk velocity, and a general Schmidt number of $Sc = 1$. The jet structure corresponds to two identical fully-developed channel flows operating at a diameter-based Reynolds number of $Re = 10000$.

In addition to the baseline Reynolds Stress Model (RSM) (Eqn. 2.4.2) and the scale-resolving Improved Instability Sensitive Reynolds Stress Model (IISRSM) (Eqn. 2.4.2), a reference Large Eddy Simulation (LES) is performed to provide suitable reference data. The introduction of the channel jets into the computational domain is achieved through separate calculations of channel segments, utilizing periodic inlet/outlet conditions. Subsequently, the resulting flow fields are mapped onto the domain inlets. The resulting slot jets impinge perpendicularly onto a smooth wall positioned at a distance of $2D$ from the corresponding channel outlets.

In Figure 5.29, the schematic representation illustrates the setup for the double-slot impinging jet configuration in this study. The implementation of the two channel flows entering the computational domain involves conducting separate precursor computations for each individual channel segment. By applying cyclic boundary conditions to the streamwise boundaries, two statistically independent, fully developed channel flows are generated. Subsequently, these fully developed and separate flow fields are mapped onto their corresponding primary inlets. To analyze scalar species transport and mixing phenomena, one of the channels contains a passive specie $C_1 = 1$ that is numerically fully dissolved, while the other channel lacks this additional specie, signified by $C_0 = 0$. Moreover, the boundary conditions for velocity fields at all walls are set to no-slip conditions. A zeroGradient boundary condition is applied to the specie C along the confining walls and all outlet boundaries.

Model	**Dimensions**	**Cells**	**Mesh size**
RSM	$30D \times 2D \times 3D$	$1000 \times 150 \times 1$	150k
IISRSM	$30D \times 2D \times 3D$	$1000 \times 150 \times 50$	7.5mio
LES	$30D \times 2D \times 3D$	$1500 \times 225 \times 105$	35mio

Table 5.1.: Dimensions, segmentation, numerical cells and resulting mesh size for the solution domain of the RSM, IISRSM and LES for the DSIJ configuration.

The dimensions of the flow development region post-impingement, the extent of the solution domain in the spanwise direction, and the resulting grid sizes are summarized in Tables 5.1 for the RSM and IISRSM as well as the LES calculations. The corresponding grid spacings expressed in wall units fall within the range of $\Delta x^+ = 2.31 - 115.92$, $\Delta y^+ = 0.92 - 231.43$, and $\Delta z^+ = 81.14$ for the IISRSM simulations. To ensure a sufficient domain length in the cartesian z-direction, preliminary results of the resolved flow field are utilized for a test of statistical independence. The domain length in z-direction is sufficient if the velocities at two different points $P(x, y, z_0)$ and $P(x, y, z_1)$ are not correlated. The corrected covariance of the two velocities $U_i(z_0)$ and $U_i(z_1)$ at $P(x, y, z_0)$ and $P(x, y, z_1)$

$$\mathrm{Cov}(U_i(z_0), U_i(z_1)) = \frac{\sum_{i=1}^{n_t}(U(z_0) - \overline{U_i(z_0)})(U_i(z_1) - \overline{U_i(z_1)})}{n_t - 1} \tag{5.4}$$

and the respective corrected variances

$$\mathrm{Var}(U_i(z_j)) = \frac{\sum_{i=1}^{n_t}(U(z_j) - \overline{U_i(z_j)})^2}{n_t - 1} \tag{5.5}$$

are utilized to determine the direct correlation

$$\rho_\mathrm{p}(U_i(z_0), U_i(z_1)) = \frac{\mathrm{Cov}(U_i(z_0), U_i(z_1))}{\sqrt{Var(U_i(z_0))Var(U_i(z_1))}} \tag{5.6}$$

which results in $\rho_\mathrm{p} = -1$ for a full negative, $\rho_\mathrm{p} = 0$ for no and $\rho_\mathrm{p} = 1$ for a full positive correlation of the respective velocity components $(U_i(z_0), U_i(z_1))$. Since the depth of the geometry in set to $z/D = 3$ and the respective boundaries are coupled by a cyclic boundary condition the evaluated points are $P(x, y, z/D = 0)$ and $P(x, y, z/D = 1.5)$. For a sample size of $n_t = 1000$ time steps the correlation results in $\rho_p(U_i(z/D = 0), U_i(z/D = 1.5)) = -2.4 * 10^{-7}$ which does not indicate any significant correlation of velocity fluctuations and a sufficiently deep computational domain.

For the two-dimensional finite volume mesh associated with the RSM calculations, the grid spacings are $\Delta x^+ = 1.57 - 122.40$ and $\Delta y^+ = 0.47 - 239.97$. Given that the Reynolds-averaged energy equation (Equation 2.14), previously utilized in the investigation of heat transfer in round jet impingement, is reduced to a form similar to the Reynolds-averaged scalar transport equation (Equation 2.15), and there exists no temperature dependency of the underlying kinematic viscosity ν and density ρ, the modeling of turbulent scalar heat and species transport can be regarded as analogous ($\overline{v\prime\theta\prime} = \overline{v\prime c\prime}$). This assumption facilitates treating all analyzed transport

phenomena as passive and scalar, leading to a more comprehensive dataset and an improved opportunity to validate scalar transport models against fields with diverse boundary conditions.

Results and Discussion

In this section, the outcomes of the comparative analysis of the baseline RSM (2.4.2) and its scale-resolving extension IISRSM (2.4.2) in conjuction with various modeling approaches for the turbulent species fluxes (Chap. 2.4.3) for a double-slot impinging jet (DSIJ) are presented. The assessment is conducted for mean flow field and species dispensation properties, along with the associated Reynolds stress tensor $\overline{u\prime_i u_j\prime}$ and turbulent species flux $\overline{u\prime_i c\prime}$, within a double slot-jet impingement configuration. To initially grasp the fundamental structural features of the discussed flow scenario, Figure 5.30 illustrates the instantaneous velocity, pressure, and species fields through their iso-contours. Additionally, the representation incorporates the vortical structures, which are delineated based on the Q-criterion.

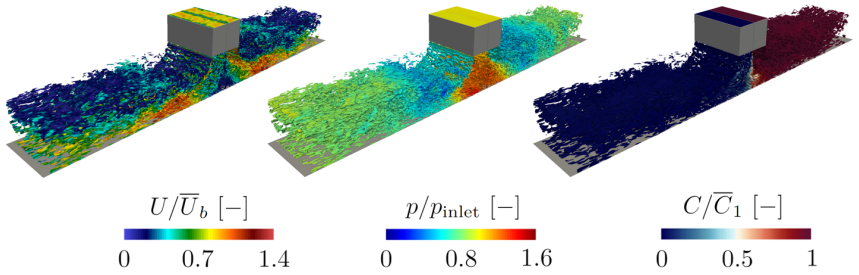

Figure 5.30.: Flow visualization by the Q-criterion, colored by the non-dimensionalized instantaneous velocity ($U/\overline{U}_b$), pressure (p/p_{inlet}) and species field ($C/\overline{C}_1$) obtained by the IISRSM in a double slot impingement configuration.

The results presented illustrate the scale resolving capabilities of the IISRSM to resolve turbulent fluctuations with respect to the corresponding velocity-, pressure and species fields. Their dynamics are mainly governed by their resolved fractions, whose generation is driven by the convective terms in the corresponding transport equations (Eqn. 2.13 & 2.15). However, in wall proximity and within the mixing layer in between both channel jets the sub-scale turbulent momentum and species fluxes are appropriately enhanced and are therefore crucial for the correct capturing of the near-wall and mixing effects. In the following, instantaneous and time-averaged mean flow and turbulence characteristics are discussed along in comparison with reference LES results. This section comparatively examines the computational results obtained by the RANS-related RSM (Eqn. 2.4.2), its scale resolving extension IISRSM (Eqn. 2.4.2) and a corresponding reference LES.

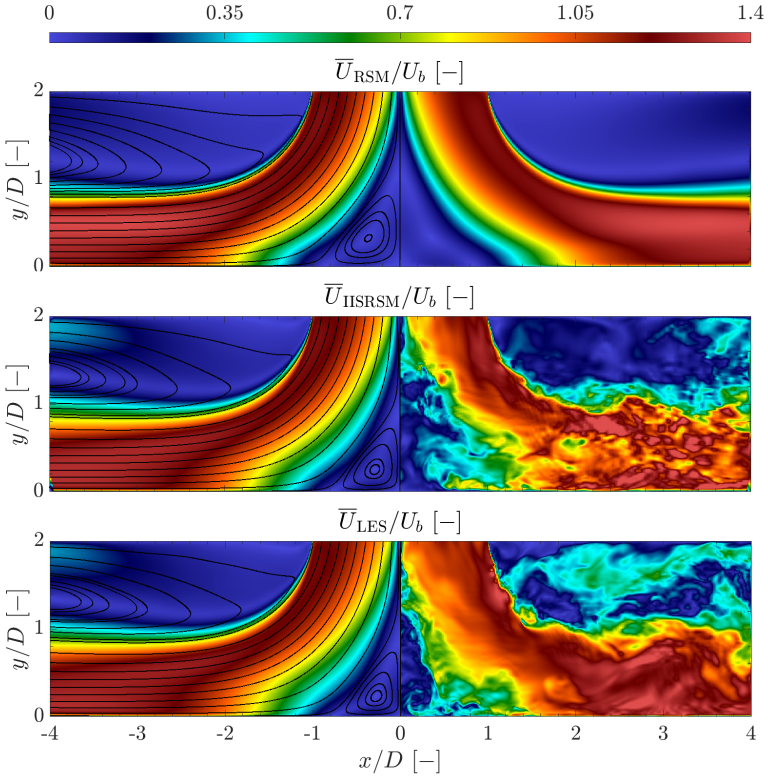

Figure 5.31.: Instantaneous and mean velocity fields normalized by the bulk velocity U_b with its corresponding stream lines obtained by the IISRSM for the present double-slot impingement configuration.

The overall flow structure depicted in Figure 5.31 bears qualitative resemblance to those observed in the previously discussed slot-jet and round jet impingement scenarios (Sections 4.2, 5.2). The instantaneous velocity field obtained from the IISRSM illustrates the model's ability to effectively capture the LES-like spectral dynamics of the flow. However, notable differences exist when compared to the planar slot-jet and round-jet impingement, where in the case of double slot-jet impingement, a significantly more pronounced high-pressure stagnation region is evident around the center of the impingement point at $y/D = 0$. This region is mainly characterized by a secondary, large-scale, low-velocity structures not commonly observed in the classical slot and round-jet impingement scenarios (Figs. 4.8 and 5.17). Another contrast lies in the deceleration of the jet stream upon impact. Comparing the confined low-velocity region at the stagnation point, the forming

flow structures within this high-pressure region are considerably larger than those observed in the single-slot and round jet impingements. Furthermore, a significant distinction from the previously investigated impingement configurations is the behavior of the streamlines exiting the channel nozzle at $y/D = 2.0$ in the double slot-jet configuration. In contrast to the abrupt and strong streamline curvature observed in the previously investigated cases (Sec. 5.2 and 5.2), the streamlines in the double slot-jet configuration exhibit a steadier and weaker curvature. This difference arises due to the quasi-doubled mass flux and dimensionless diameter associated with the combined two inlets in the double slot-jet configuration. This alteration significantly influences species transfer within the mixing plane.

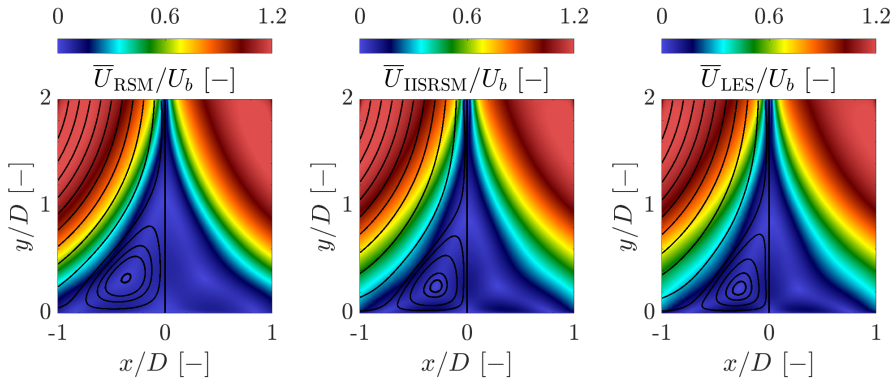

Figure 5.32.: Mean velocity field ($U/\overline{U}_b$) around the stagnation point $-1 \leq x/D \leq 1$ and $0 \leq y/D \leq 2$ of the double slot-jet impingement configuration obtained by LES, IISRSM and RSM.

All time-averaged mean velocity fields within the region $-1 \leq x/D \leq 1$ and $0 \leq y/D \leq 2$, as depicted in Fig. 5.32, exhibit remarkably similar qualitative outcomes. The time-averaged mean velocity fields obtained from RANS-RSM exhibit a significant level of agreement with the reference LES data. Notably, they accurately capture the secondary flow structure within the stagnation region. This achievement is particularly notable, given that RANS-related models often struggle to correctly predict the secondary double vortex, its separation, and the reattachment points. The primary distinction between the baseline RSM results and the scale-resolving approaches (IISRSM and LES) in the time-averaged velocity field is relatively minor. It manifests as a slightly more diffused secondary flow structure, particularly in the region between the two incoming slot jets (indicated by the blue flow regime), characterized by the separating streamline at the outer boundary of the stagnation region. Overall, the agreement between the RSM results

and the scale-resolving methods (IISRSM and LES) in terms of the time-averaged velocity field is quite remarkable, especially in capturing the complex secondary flow patterns.

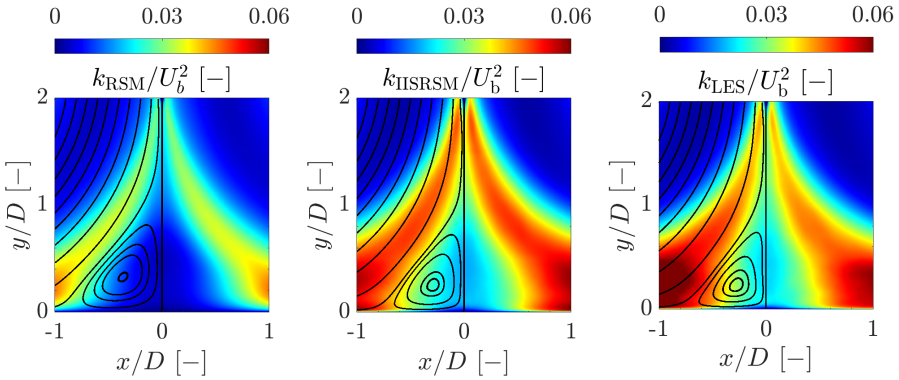

Figure 5.33.: Mean turbulence kinetic energy ($k/\overline{U}_b^2$) around the stagnation point $-1 \leq x/D \leq 1$ and $0 \leq y/D \leq 2$ of the double slot-jet impingement configuration obtained by LES, IISRSM and RSM.

Figure 5.33 shows the turbulence kinetic energy within the impingement region of the DSIJ configuration obtained by the baseline RSM, the scale resolving IISRSM and the reference LES. The topology of the turbulence kinetic energy evolution unveils a flow pattern that is not typical for impinging jet configurations with a nozzle-plate distance of $H/D = 2$, with a significantly more pronounced stagnation region and inner shear layer that is almost reaching into the inlet channels. The inner shear layers, characterized by enhanced turbulent activity and the resulting stagnation region in between these shear layers, cannot be seen in any previously investigated impingement configuration. Therefore, all further comparative evaluations are focusing on the flow area directly beneath the two inlet channels at $-1 \leq x/D \leq 1$ and $0 \leq y/D \leq 2$ as seen in figure 5.33. The qualitative topology of the turbulent kinetic energy evolution around the impingement region of both RANS-related models is in good accordance to the comparative LES data. The absolute values however, are significantly differing between the baseline and scale-resolving RANS model. Since the streamline curvature around the impingement area of the DSIJ configuration is not as intense as it is for the single-slot and round jet impingement, the resulting turbulence kinetic energy obtained by the baseline RSM does not deliver an unreasonable over-prediction, but rather an under prediction of turbulent activity when compared to the reference LES data. The corresponding results obtained by the scale-resolving IISRSM are in significantly better accordance when compared

to the LES data. However the notably coarser grid arrangement of the IISRSM in comparison to the reference LES case setup is leading to a slightly thickened inner shear layer at the inner wall of the nozzle exit when compared to the LES data.

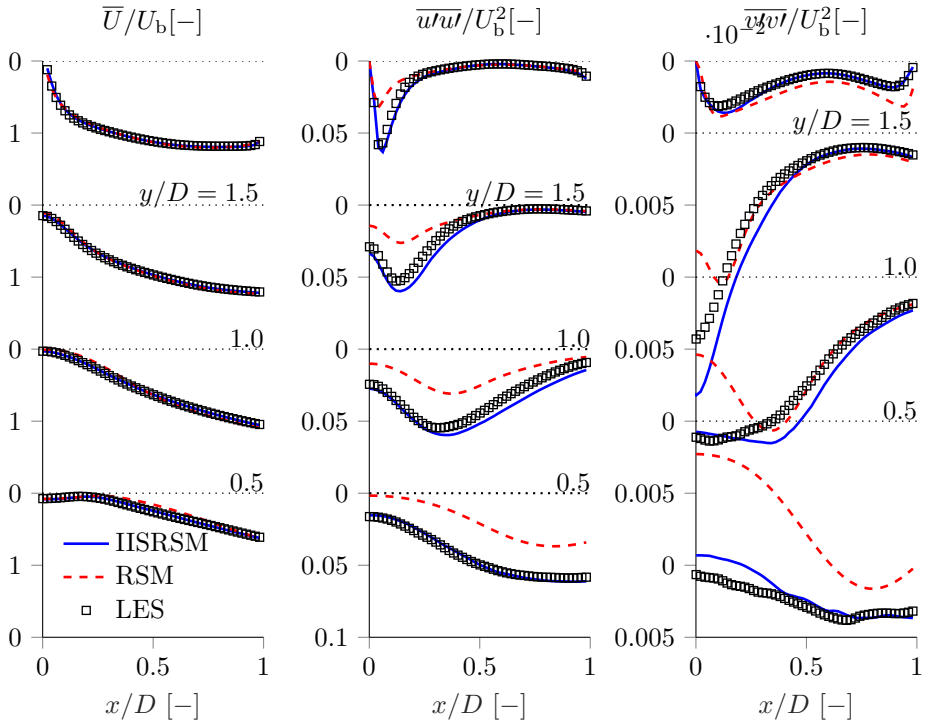

Figure 5.34.: Vertical, wall-normal profile development of the mean velocity magnitude $\overline{U}$, the wall normal Reynolds stress component $\overline{u'u'}$ and the wall parallel Reynolds stress component $\overline{v'v'}$ normalized by the mean bulk velocity U_b of the the double-slot-jet impingement configuration at $-1 \leq x/D \leq 1$ and $0 \leq y/D \leq 2$.

Fig. 5.34 provides insight into the wall-normal profile development of various flow parameters within the double-slot-jet impingement configuration, specifically the mean velocity magnitude $\overline{U}$, the wall-normal Reynolds stress component $\overline{u'u'}$, and the wall-parallel Reynolds stress component $\overline{v'v'}$. These profiles are normalized by the mean bulk velocity U_b and are presented within the dimensionless region $-1 \leq x/D \leq 1$ and $0 \leq y/D \leq 2$. The velocity profiles ($\overline{U}/U_\mathrm{b}$) exhibit a typical deceleration phenomenon associated with impingement flows, resulting in a loss of momentum through the forming high-pressure stagnation region. The flow's

momentum is deflected during the impingement process (at $x/D = -1.0 - 1.0$) and is subsequently transferred into wall jets at $x/D \geq ||1||$ (see fig. 5.31). Both RANS-related results show strong agreement with the reference LES data. However, there is a slight deviation in the RANS-RSM-related results within the stagnation region near the bottom wall at $y/D \leq 1.0$. The presence of a relatively large high-pressure region makes it more challenging to capture secondary flow structures within the stagnation region. This challenge arises because the influence of pressure gradient-related momentum transport decreases compared to the previously investigated slot-jet and round-jet impingement scenarios (Sections 4.2 and 5.2). Consequently, the diminishing influence of the non-modeled pressure gradient-related momentum transport leads to a higher contribution from viscous and turbulent diffusion in terms of momentum transport. Given that the viscous diffusion term within the Reynolds-averaged momentum equation (Equation 2.13) plays a smaller role compared to the turbulent momentum flux (Reynolds stress tensor $\overline{u\prime_i u\prime_i}$), accurately predicting the Reynolds stress tensor is crucial for correctly capturing low-velocity flow patterns within the double-slot-jet configuration.

While the non-dimensionalized vertical (normal to the impinging wall) and wall normal $\overline{v\prime v\prime}/U_\mathrm{b}^2$ Reynolds stress components predicted by the IISRSM closely follow the reference LES database (Fig. 5.34), the RANS-RSM-related stress components exhibit a significant under prediction at all vertical distances from the bottom wall ($z/D = 2.0$, 1.5, 1.0, 0.5). The influence of the extended high pressure stagnation regime into the inlet channel ($z/D = 2.0$) is clearly visible as the relative to the bottom wall, vertical Reynolds stress component $\overline{u\prime u\prime}/U_\mathrm{b}^2$ is fully asymmetric and only exhibits a pronounced peak close to the inner wall at $x/D = 0$. Its important to recall that the extended high pressure stagnation region significantly reduces the maximum streamline curvature of the mean flow in comparison to the single slot- and round jet impingement (Sec. 4.2, 5.2), as the flow is almost immediately deflected at the respective nozzle outlets ($y/D = 2.0$). This constant, but not as intense streamline curvature does not lead to an over prediction of turbulent stresses by the RANS-RSM, as it has been observed in the previous stagnation flow configurations. The basic expression of the wall-reflection redistribution term within the Reynolds stress transport equation of the present baseline RSM, has shown difficulties in dealing with wall normal flows as it was originally formulated for wall-parallel flows (Craft, Graham, and Launder, 1993). On the other hand, considering the significant under-prediction of the RSM-related turbulent kinetic energy, the overall good agreement of the mean velocity field is mainly due to the dominating influence of the mean pressure gradient within the equation of motion, still significantly overcoming the Reynolds stress gradients.

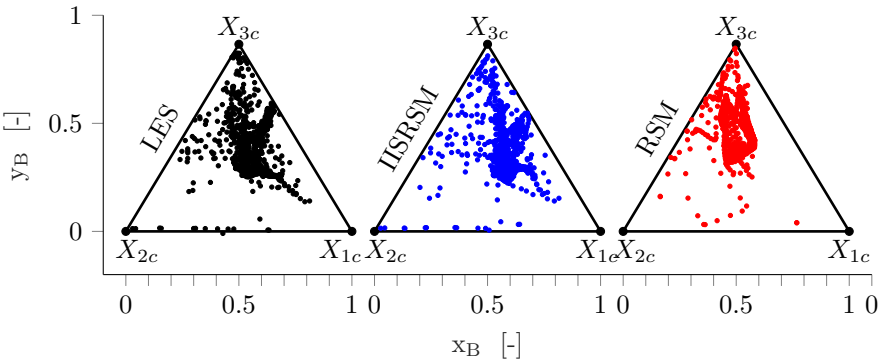

Figure 5.35.: Point cloud of the barycentric coordinates ($x_B(a_{ij})$, $y_B(a_{ij})$) at $-1 \leq x/D \leq 1$ and $0 \leq y/D \leq 2$ obtained by the LES, scale-resolving IISRSM and baseline RSM for the double slot-jet impingement configuration.

The evaluation of the Reynolds stress anisotropy tensor a_{ij} and its capability to depict anisotropic momentum and temperature transport is utilized for various comparative techniques within the current flow configuration. As introduced in Sec. 3.1, the barycentric anisotropy map is a crucial tool that offers important information about the general realizability of numerically predicted Reynolds stress fields for each computed data point within the physical computational domain of all respective numerical approaches and models. This analysis confirms the general realizability of all turbulent states for every considered numerical approach. Notably, the barycentric anisotropy map in Fig. 5.35, representing the entire physical domain, demonstrates that the scale-resolving IISRSM's anisotropic states (blue) (Chapter 2.4.2) closely align with the reference LES data (black), while the baseline RSM's (red) results exhibit slight differences. Given that analyzing anisotropy-related point clouds of the physical domain, as seen in Figure 5.35, without further information about their corresponding physical locations lacks the granularity needed for a comprehensive comparative assessment, the barycentric coordinates from Figure 5.23 can be utilized to map the anisotropic turbulent states represented by the coordinates x_B and y_B back to the actual physical domain. The visualization method applied for these barycentric coordinates has been previously utilized in Sec. 5.2 in conjunction with the round-jet impingement and can be found in section 3.1.

Drawing upon the attributes of the barycentric anisotropy map presented in Fig. 5.36, and transferring its insights back to the physical domain through color-coding, as previously introduced in Chap. 3.1, the depicted resulting iso-contours provide a deeper understanding of the anisotropic turbulent state

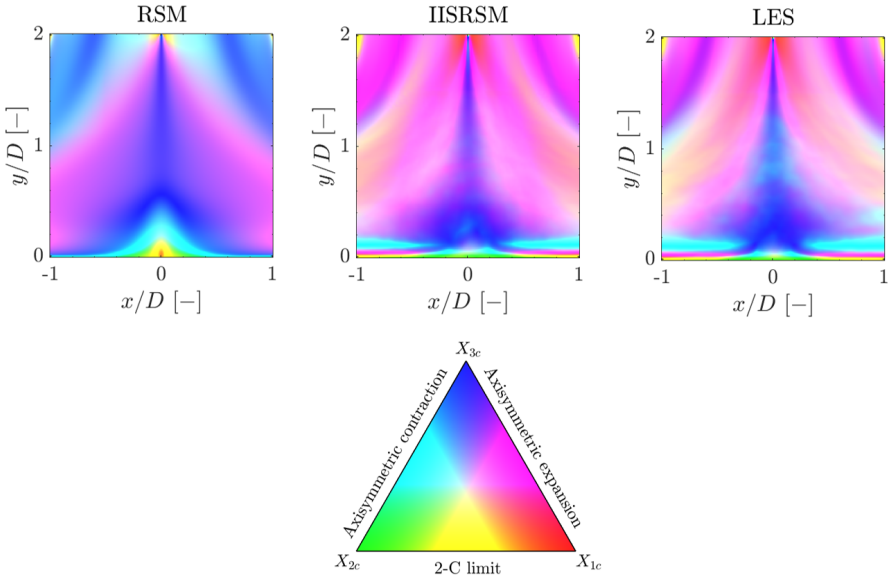

Figure 5.36.: Coloring of the barycentric coordinates $x_B(a_{ij})$ and $y_B(a_{ij})$ for every data point ($-1 \leq x/D \leq 1$ and $0 \leq y/D \leq 2$) of the computational double-slot impinging jet configuration domain obtained by the LES, scale-resolving IISRSM and baseline RSM.

within the double slot jet impingement configuration. Following the vertical mixing layer at $x/D = 0$ from the separating wall of the two incoming channels at $y/D = 2$ to the bottom wall, the mixing layer undergoes a deceleration, characterized by an axisymmetric near-wall compression, characterized by a color shift from blue (indicative of three componental isotropic turbulence X_{c3}) to green (indicative of axisymmetric two-componental turbulence X_{c2}). These features are accurately captured by the scale-resolving IISRSM when compared to the reference LES data. Another noteworthy flow characteristic, correctly predicted by the scale-resolving RANS-related IISRSM, is the intense acceleration at the inner wall edge of the nozzle exit at $y/D = 2$ and $x/D = 0$, which is characterized by a color shift into dark red (indicative of one-componental turbulence - X_{c1}). Evaluating the intricate barycentric coloring of the underlying anisotropic turbulent states, an convincing agreement between the scale-resolving IISRSM and the corresponding reference DNS results is evident.

To perform a comprehensive evaluation of the color-coded barycentric coordinates x_B and y_B, the corresponding method is applied along the previously selected horizontal lines at the dimensionless positions $y/D = 2.0$, 1.5, 1.0, and 0.5 within

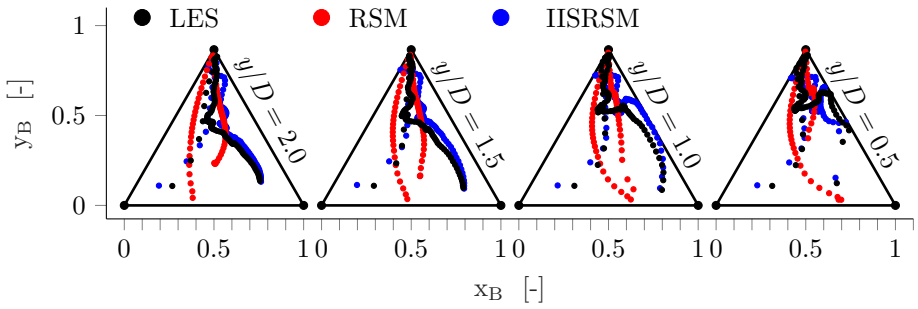

Figure 5.37.: Trajectories of the barycentric coordinates ($x_B(a_{ij})$, $y_B(a_{ij})$) at $z/D = 2.0$, 1.5, 1.0, 0.5 obtained by the LES, scale-resolving IISRSM and baseline RSM for the double slot-jet impingement configuration at $0 \leq x/D \leq 1$.

the impinging double-slot-jet configuration. The comparative assessment aims to quantify the predictive capabilities in terms of anisotropic turbulent behavior along the horizontal (parallel to the wall) direction of the double-slot jet impingement (DSIJ), employing the barycentric map as a tool. The results of this evaluation are illustrated in Figure 5.37, showcasing the evolution of barycentric coordinates as obtained from the reference LES, IISRSM, and RSM. In this assessment, the scale-resolving IISRSM demonstrates a high degree of agreement with the LES data across all four vertical positions evaluated. However, the baseline RSM exhibits considerable deviations from the reference LES results. It's important to note that despite the significant discrepancy between the RSM-related turbulent kinetic energy and the associated Reynolds stress components, as observed in Figures 5.33 and 5.34, the mean flow velocity closely matches the LES data. This discrepancy arises mainly due to the substantial influence of the mean pressure gradient within the deflected jets, which here dominates the momentum transport equation and significantly outweighs the impact of gradients of turbulent stresses $\overline{u\prime_i u\prime_j}$.

Figure 5.38 portrays the mean species field normalized by the maximum species fraction ($\overline{C}/\overline{C}_1$) around the stagnation point within the region $-1 \leq x/D \leq 1$ and $0 \leq y/D \leq 2$ of the double slot-jet impingement configuration. The portrayed data is obtained using LES, IISRSM, and RSM along with the Simple Gradient Diffusion Hypothesis (SGDH) for modeling the turbulent species flux $\overline{u\prime_i \theta\prime}$, as introduced in Sec. 2.4.3. The differences in performance among the tested turbulence models are evident within the resulting species fields. Notably, the species distribution obtained from the baseline RSM and IISRSM combined with the SGDH model closely matches the corresponding distribution obtained from LES. However, the scale-resolving and baseline RANS models become do show a slight difference

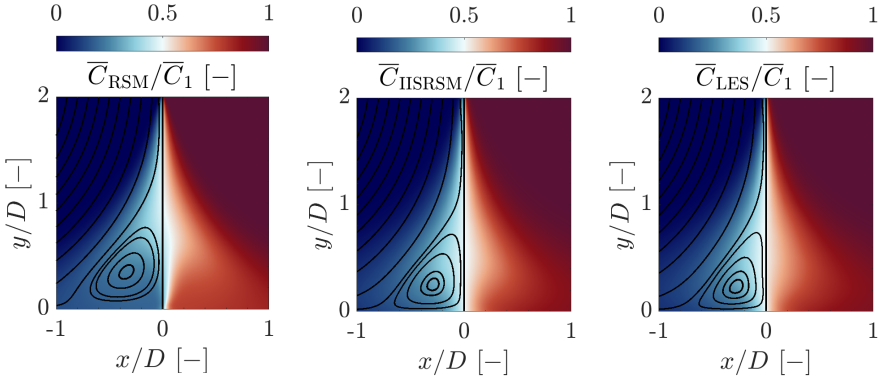

Figure 5.38.: Mean species field ($\overline{C}/\overline{C}_1$) around the stagnation point $-1 \leq x/D \leq 1$ and $0 \leq y/D \leq 2$ of the double slot-jet impingement configuration obtained by LES, IISRSM and RSM in conjunction with the simple gradient diffusion hypothesis (Sec. 2.4.3) for the modeling of the turbulent species flux $\overline{u\prime_i \theta\prime}$.

within the upper shear layer located at $x/D = 0$ and $y/D = 1.5$ and in the outer region around $x/D = ||1||$. In this region, the RSM-derived results exhibit an enhanced and more diffuse mixing process compared to the scale-resolving IISRSM and LES outcomes. This difference underscores the ability of the scale-resolving IISRSM to capture finer details in the mixing process, particularly in comparison to the fully time-averaged RSM.

Since the above qualitative comparison does not provide detailed insight into the predicted mixing processes, Fig. 5.39 portrays the normalized mean species concentration $\overline{C}/\overline{C}_1$ in horizontal, wall-parallel x-direction at different characteristic distances to the inlet nozzles ($y/D = 2.0, 1.5, 1.0, 0.5$). The comparative assessment contains the numerically predicted dimensionless species concentration $\overline{C}/\overline{C}_1$, obtained by the time-accurate, scale-resolving LES and IISRSM in conjunction with the SGDH modeling approach for the turbulent species flux $\overline{u_i\theta}$ plotted against the RANS-RSM-related, predicted species concentration in conjunction with the SGDH (Sec. 2.30), GGDH (Sec. 2.31) and HOGGDH (Sec. 2.32) modeling approach. To emphasize mixing processes within the vicinity of the main mixing shear layer at $x/D = 0$ The non-dimensionalized y-axis y/D is plotted semilogarithmically. Since the evaluated, IISRSM-related species concentrations are in almost perfect agreement with the reference LES data, the further comparative assessment emphasizes the predictive capabilities of the RSM-related results. The performance difference among the tested species-flux models is clearly visible for the comparative evaluation at $y/D = 2.0$, as the mixing processes in the wall-

normal mixing layer predicted by RSM-related GGDH and HOGGDH modeling approaches show a slightly better accordance to the reference LES data. However, the enhancing influence of the strengthened species transport, which is beneficial in the direct mixing layer, leads to an overestimation of species transport at the outer, evaluated regions around $x/D = ||1||$.

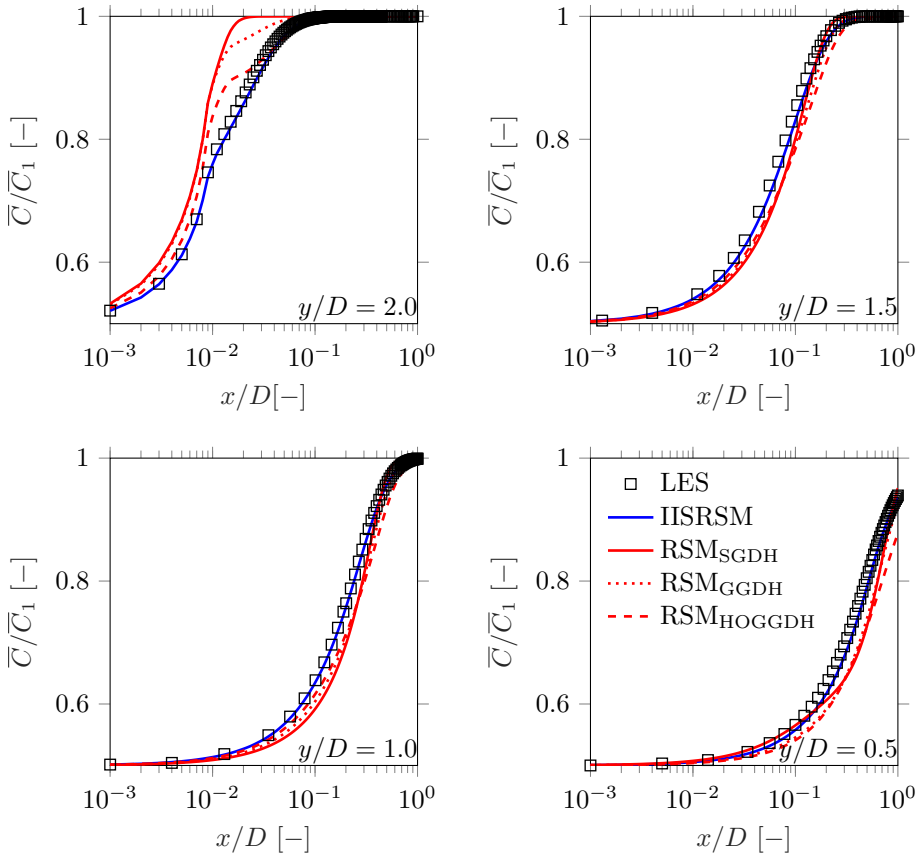

Figure 5.39.: Mean species concentration $\overline{C}/\overline{C}_1$ in x-direction ($0 \leq x/D \leq 1$) at four characteristic distances to the inlet nozzles ($y/D = 2.0$, 1.5, 1.0, 0.5), obtained by LES, IISRSM and RSM in conjunction with the SGDH, GGDH and HOGGDH species flux modeling approach for the double slot-jet impingement configuration.

Concluding this chapter, the primary goal was to assess the predictive performance of the baseline Reynolds-Averaged Navier-Stokes Reynolds-Stress Model (RANS-RSM) and its scale-resolving extension, known as the Improved Instability-Sensitive

Reynolds-Stress Model (IISRSM), within the Sensitized-RANS concept. This assessment was carried out by comparing these models against a reference LES database in the context of a turbulent double-slot jet impinging on a smooth wall. The focus of the comparison was on evaluating the models' abilities to accurately predict anisotropic momentum and heat transport processes. Both RANS-related modeling approaches demonstrated strong agreement with LES data when predicting the mean velocity field. However, the scale-resolving IISRSM displayed a notably higher level of agreement with LES when it came to predicting Reynolds stress components compared to the baseline RSM. Additionally, while the baseline RSM, in combination with the considered SGDH, GGDH, and HOGGDH species flux models, showed reasonable alignment with the reference LES data, it tended to over-predict turbulent species transport while under-predicting turbulent stress components. In contrast, the scale-resolving IISRSM provided improved predictions for velocity, Reynolds stress, and species profiles, closely matching the LES database.

In summary, several important insights were gained from this chapter. To accurately predict near-wall species fields using RANS-based models, whether in conventional or sensitized RANS frameworks, it's essential not only to capture the velocity field but also to accurately model the anisotropic turbulent stress tensor. This is particularly crucial within the impingement region and the subsequently generated wall-jet, which is characterized by flow straining in varying directions. On the other hand, sensitizing a second-order Reynolds stress model to effectively resolve unsteady turbulence fluctuations can significantly enhance the prediction of flow structure across various dependent flow properties, including velocity, Reynolds stress, and species fields. This improvement is particularly pronounced in inherently highly unsteady flow regions where a significant portion of turbulence is resolved.

6. Conclusions and outlook

The main objective of the present work was to evaluate the predictive performance of the basic RANS-Reynolds-Averaged Navier-Stokes Reynolds stress model (RANS-RSM) (Sec. 2.4.2) and its scale-resolved extension, the Improved Instability-Sensitive Reynolds stress model (IISRSM) (Sec. 2.4.2), in the context of the Sensitized RANS concept in conjunction with various closure approaches for the turbulent heat and species flux. In this context, the presently simulated flow cases represent configurations that are outside the flow classes computed in the original model development. The assessments were carried out by comparing the predictive capabilities of the RANS-RSM-based models against reference DNS of a turbulent channel flow, slot-jet impingement, asymmetric jet impingement subjected to heat transfer and a reference LES of double-slot jet impingement in conjunction with species transport, with the latter LES database contributing to the present work. Finally, a highly turbulent inflow into a complex IC engine geometry was used to help critically evaluate the model. The focus of the comparison was on evaluating the models' abilities to accurately predict anisotropic momentum and heat and species transport processes in wall-parallel and more importantly, wall-normal flow configurations. A key contribution for an improved assessment of RANS-related as well as DNS-/LES-related computational results was the utilization of barycentric coloring, transferring information about Reynolds stress anisotropy directly back to the physical domain and therefore, drastically improve the understanding of its evolution in immediate wall vicinity. Both RANS-related modeling approaches demonstrated strong agreement with the respective reference DNS and LES data when predicting the mean velocity field. However, the scale-resolving IISRSM displayed a notably higher level of agreement with corresponding reference data sets when it came to predicting Reynolds stress components and their combined anisotropic behaviour, compared to the baseline RSM. In addition, the baseline RSM in combination with the considered SGDH (Sec. 2.30), GGDH (Sec. 2.31), and HOGGDH (Sec. 2.32) species flux models showed a significant deviation from the reference DNS/LES data, as it significantly over-predicted the turbulent heat and species transport. In contrast, the scale-resolving IISRSM provided improved predictions for velocity, Reynolds stress, and species profiles, closely matching the respective corresponding reference databases.

In summary, several important insights were gained from this thesis. To accurately predict near-wall species fields using RANS-based models, whether in conventional or sensitized RANS frameworks, it is essential not only to capture the velocity field but also to accurately model the anisotropic turbulent stress tensor. This is particularly important in the region of impact and the resulting wall jet in flows perpendicular to the wall, which is characterized by variably oriented flow straining with respect to a fully populated deformation velocity tensor. On the other hand, sensitizing a second-order Reynolds stress model to effectively resolve unsteady turbulence fluctuations can significantly enhance the prediction of flow structure across various dependent flow properties, including velocity, Reynolds stress, and species fields. The resolution of fluctuating pressure and velocity fields which can be obtained by the scale-resolving IISRSM significantly improves the numerical prediction of redistribution and transport processes in immediate wall-vicinity. This improvement is particularly pronounced in inherently highly unsteady flow regions where a significant portion of turbulence is resolved.

New specific contributions of the present thesis

The numerical investigation and anisotropy characterization of the IC engine intake flow into the TUDa Flowbench utilizing an, in this scope newly generated reference LES database expands the understanding of critical mesh and simulation parameter when applying time-accurate scale-resolving RANS-based Reynolds-stress models in highly complex geometries. The present IC intake flow analysis further proves the validity of scale-resolving RANS-based Reynolds-stress models for the simulation of future application-oriented non-generic flow configurations.

A new generic double-slot impinging jet (DSIJ) flow configuration in conjunction with a novel corresponding LES database has been created. The present simulations of the DSIJ configuration serves as a comprehensive preliminary investigation for an intended experimental investigation and DNS analysis as a part of collaborative work within the DFG CRC TRR 150 of the German Research Foundation.

An extensive elaboration and extended application of characterization techniques for anisotropy of the second-order Reynolds-stress tensor delivers a full insight into the advantages and disadvantages of well-established, common and recently developed methodologies. The corresponding, in scope of this work developed routines can be utilized for equal anisotropy visualization of steady and scale-resolving numerical simulations as well as appropriate experimental data sets.

Last but foremost an extensive investigation of first- and second-order closure-approaches for the turbulent heat and species flux in conjunction with conventional and scale-resolving second-moment RANS models has been created for a variety of wall-parallel, wall-perpendicular, as well as complex IC-engine-related flow

conditions. The present thesis demonstrates that the predictive accuracy of heat, species and mass transfer in turbulent flows can be significantly and reliably enhanced through the sensitivation of second-moment RANS models.

Bibliography

[1] K. Abe and K. Suga. "Towards the development of a Reynolds-averaged algebraic turbulent scalar-flux model". In: *International Journal of Heat and Fluid Flow* 22.1 (2001), pp. 19–29. DOI: https://doi.org/10.1016/s0142-727x(00)00062-x.

[2] A. Avcı, M. Can, and A. B. Etemoğlu. "A theoretical approach to the drying process of thin film layers". In: *Applied thermal engineering* 21.4 (2001), pp. 465–479. DOI: https://doi.org/10.1016/s1359-4311(00)00060-0.

[3] S. Banerjee, R. Krahl, F. Durst, and C. Zenger. "Presentation of anisotropy properties of turbulence, invariants versus eigenvalue approaches". In: *Journal of Turbulence* 8 (2007), N32. DOI: https://doi.org/10.1080/14685240701506896.

[4] B. Basara and S. Jakirlic. "A new hybrid turbulence modelling strategy for industrial CFD". In: *International journal for numerical methods in fluids* 42.1 (2003), pp. 89–116. DOI: https://doi.org/10.1002/fld.492.

[5] M. Behnia, S. Parneix, Y. Shabany, and P. Durbin. "Numerical study of turbulent heat transfer in confined and unconfined impinging jets". In: *International Journal of Heat and Fluid Flow* 20.1 (1999), pp. 1–9. DOI: https://doi.org/10.1016/s0142-727x(98)10040-1.

[6] T. L. Bergman. *Fundamentals of heat and mass transfer*. John Wiley & Sons, 2011.

[7] M. Bopp, S. Wegt, L. Krüger, F. Secchi, B. Frohnapfel, and S. Jakirlić. "Flow and thermal fields modeling in jet impingement configurations using a Reynolds stress turbulence closure within the RANS and Sensitized-RANS framework". In: *International Journal of Heat and Fluid Flow* 105 (2024), p. 109263. DOI: https://doi.org/10.1016/j.ijheatfluidflow.2023.109264.

[8] J. Boussinesq. *Essai sur la théorie des eaux courantes*. Impr. nationale, 1877.

[9] I. Celik. *RANS/LES/DES/DNS: The future prospects of turbulence modeling*. 2005. DOI: https://doi.org/10.1115/1.2033011.

[10] K.-C. Chang and M.-J. Shyu. "Revisiting the Reynolds-averaged energy equation in near-wall turbulence models". In: *International journal of heat and mass transfer* 43.5 (2000), pp. 665–676. DOI: https://doi.org/10.1016/s0017-9310(99)00177-5.

[11] K.-S. Choi and J. L. Lumley. "The return to isotropy of homogeneous turbulence". In: *Journal of Fluid Mechanics* 436 (2001), pp. 59–84. DOI: https://doi.org/10.1017/s002211200100386x.

[12] D. P. Combest, P. A. Ramachandran, and M. P. Dudukovic. "On the gradient diffusion hypothesis and passive scalar transport in turbulent flows". In: *Industrial & Engineering Chemistry Research* 50.15 (2011), pp. 8817–8823. DOI: https://doi.org/10.1021/ie200055s.

[13] T. Craft, L. Graham, and B. E. Launder. "Impinging jet studies for turbulence model assessment—II. An examination of the performance of four turbulence models". In: *International Journal of Heat and Mass Transfer* 36.10 (1993), pp. 2685–2697. DOI: https://doi.org/10.1016/s0017-9310(05)80205-4.

[14] T. Dakos and M. Gibson. "On modelling the pressure terms of the scalar flux equations". In: *Turbulent Shear Flows 5: Selected Papers from the Fifth International Symposium on Turbulent Shear Flows, Cornell University, Ithaca, New York, USA, August 7–9, 1985*. Springer. 1987, pp. 7–18. DOI: https://doi.org/10.1007/978-3-642-71435-1_2.

[15] B. J. Daly and F. H. Harlow. "Transport equations in turbulence". In: *The physics of fluids* 13.11 (1970), pp. 2634–2649.

[16] M. Emory and G. Iaccarino. "Visualizing turbulence anisotropy in the spatial domain with componentality contours". In: *Center for Turbulence Research Annual Research Briefs* (2014), pp. 123–138.

[17] C. R. Ferguson and A. T. Kirkpatrick. *Internal combustion engines: applied thermosciences*. John Wiley & Sons, 2015.

[18] J. H. Ferziger, M. Perić, and R. L. Street. *Computational methods for fluid dynamics*. Vol. 3. Springer, 2002.

[19] D. Freudenhammer, E. Baum, B. Peterson, B. Böhm, B. Jung, and S. Grundmann. "Volumetric intake flow measurements of an IC engine using magnetic resonance velocimetry". In: *Experiments in Fluids* 55 (2014), pp. 1–18. DOI: https://doi.org/10.1007/s00348-014-1724-6.

[20] M. Hadžiabdić and K. Hanjalić. "Vortical structures and heat transfer in a round impinging jet". In: *Journal of Fluid Mechanics* 596 (2008), pp. 221–260. DOI: https://doi.org/10.1017/s002211200700955x.

[21] J.-C. Han, S. Dutta, and S. Ekkad. *Gas turbine heat transfer and cooling technology*. CRC press, 2012. DOI: https://doi.org/10.1201/b13616-6.

[22] K. Hanjalić and B. E. Launder. "Contribution towards a Reynolds-stress closure for low-Reynolds-number turbulence". In: *Journal of Fluid Mechanics* 74.4 (1976), pp. 593–610. DOI: https://doi.org/10.1017/s0022112076001961.

[23] Y. M. Hashash, J. I.-C. Yao, and D. C. Wotring. “Glyph and hyperstreamline representation of stress and strain tensors and material constitutive response”. In: *International journal for numerical and analytical methods in geomechanics* 27.7 (2003), pp. 603–626. DOI: https://doi.org/10.1002/nag.288.

[24] C. Hasse. “Scale-resolving simulations in engine combustion process design based on a systematic approach for model development”. In: *International Journal of Engine Research* 17.1 (2016), pp. 44–62. DOI: https://doi.org/10.1177/1468087415597842.

[25] H. Hattori and Y. Nagano. “Direct numerical simulation of turbulent heat transfer in plane impinging jet”. In: *International Journal of Heat and Fluid Flow* 25.5 (2004), pp. 749–758. DOI: https://doi.org/10.1016/j.ijheatfluidflow.2004.05.004.

[26] M. Haussmann, F. Ries, J. B. Jeppener-Haltenhoff, Y. Li, M. Schmidt, C. Welch, L. Illmann, B. Böhm, H. Nirschl, M. J. Krause, et al. “Evaluation of a near-wall-modeled large eddy lattice Boltzmann method for the analysis of complex flows relevant to IC engines”. In: *Computation* 8.2 (2020), p. 43. DOI: https://doi.org/10.3390/computation8020043.

[27] P. Hill and D. Zhang. “The effects of swirl and tumble on combustion in spark-ignition engines”. In: *Progress in energy and combustion science* 20.5 (1994), pp. 373–429. DOI: https://doi.org/10.1016/0360-1285(94)90010-8.

[28] C. Hirsch. *Numerical computation of internal & external flows: fundamentals of numerical discretization*. John Wiley & Sons, Inc., 1988.

[29] C.-M. Ho and N. S. Nosseir. “Dynamics of an impinging jet. Part 1. The feedback phenomenon”. In: *Journal of Fluid Mechanics* 105 (1981), pp. 119–142.

[30] K. Horiuti. “Assessment of two-equation models of turbulent passive-scalar diffusion in channel flow”. In: *Journal of Fluid Mechanics* 238 (1992), pp. 405–433. DOI: https://doi.org/10.1017/s0022112092001769.

[31] S. Jakirlić and K. Hanjalić. “A new approach to modelling near-wall turbulence energy and stress dissipation”. In: *Journal of fluid mechanics* 459 (2002), pp. 139–166. DOI: https://doi.org/10.1017/s0022112002007905.

[32] S. Jakirlić and R. Maduta. “Extending the bounds of ‘steady’RANS closures: Toward an instability-sensitive Reynolds stress model”. In: *International Journal of Heat and fluid flow* 51 (2015), pp. 175–194. DOI: https://doi.org/10.1016/j.ijheatfluidflow.2014.09.003.

[33] S. Jakirlić. *Reynolds-spannungs-modellierung komplexer turbulenter Stroemungen*. Herbert Utz Verlag, 1997.

[34] K. Jambunathan, E. Lai, M. Moss, and B. Button. "A review of heat transfer data for single circular jet impingement". In: *International journal of heat and fluid flow* 13.2 (1992), pp. 106–115. DOI: https://doi.org/10.1016/0142-727x(92)90017-4.

[35] J. Jovanovic. *The statistical dynamics of turbulence*. Springer Science & Business Media, 2004. DOI: https://doi.org/10.1007/978-3-662-10411-8.

[36] H.-J. Kaltenbach, T. Gerz, and U. Schumann. "Large-eddy simulation of homogeneous turbulence and diffusion in stably stratified shear flow". In: *Journal of Fluid Mechanics* 280 (1994), pp. 1–40. DOI: https://doi.org/10.1017/s0022112094002831.

[37] N. Kasagi, Y. Tomita, and A. Kuroda. "Direct numerical simulation of passive scalar field in a turbulent channel flow". In: (1992). DOI: https://doi.org/10.1115/1.2911323.

[38] K. Keskinen, J. Koch, Y. M. Wright, M. Schmitt, M. Nuutinen, O. Kaario, V. Vuorinen, M. Larmi, and K. Boulouchos. "Numerical assessment of wall modelling approaches in scale-resolving in-cylinder simulations". In: *International Journal of Heat and Fluid Flow* 74 (2018), pp. 154–172. DOI: https://doi.org/10.1016/j.ijheatfluidflow.2018.09.016.

[39] A. N. Kolmogorov. "The local structure of turbulence in incompressible viscous fluid for very large Reynolds number". In: *Dokl. Akad. Nauk. SSSR*. Vol. 30. 1941, pp. 301–303. DOI: https://doi.org/10.1070/pu1968v010n06abeh003710.

[40] P.-Å. Krogstad and L. E. Torbergsen. "Invariant analysis of turbulent pipe flow". In: *Flow, turbulence and combustion* 64 (2000), pp. 161–181.

[41] B. E. Launder. "On the computation of convective heat transfer in complex turbulent flows". In: (1988). DOI: https://doi.org/10.1115/1.3250614.

[42] J. L. Lumley. "Computational modeling of turbulent flows". In: *Advances in applied mechanics* 18 (1979), pp. 123–176.

[43] J. L. Lumley and G. R. Newman. "The return to isotropy of homogeneous turbulence". In: *Journal of Fluid Mechanics* 82.1 (1977), pp. 161–178. DOI: https://doi.org/10.1017/s0022112077000585.

[44] R. Maduta and S. Jakirlic. "Improved RANS Computations of Flow over the 25 [degrees]-Slant-Angle Ahmed Body". In: *SAE International Journal of Passenger Cars-Mechanical Systems* 10.2 (2017). DOI: https://doi.org/10.4271/2017-01-1523.

[45] H. Martin. "Heat and mass transfer between impinging gas jets and solid surfaces". In: *Advances in heat transfer*. Vol. 13. Elsevier, 1977, pp. 1–60. DOI: https://doi.org/10.1016/s0065-2717(08)70221-1.

[46] R. D. Moser, J. Kim, and N. N. Mansour. “Direct numerical simulation of turbulent channel flow up to Re τ= 590”. In: *Physics of fluids* 11.4 (1999), pp. 943–945.

[47] F. Nicoud and F. Ducros. “Subgrid-scale stress modelling based on the square of the velocity gradient tensor”. In: *Flow, turbulence and Combustion* 62.3 (1999), pp. 183–200.

[48] A. Pati. “Numerical investigation of the in-cylinder flow-spray-wall interactions in direct injection engines”. In: (2022).

[49] S. B. Pope. *Turbulent flows*. Cambridge university press, 2000. DOI: https://doi.org/10.1017/cbo9780511840531.

[50] O. Reynolds. “IV. On the dynamical theory of incompressible viscous fluids and the determination of the criterion”. In: *Philosophical transactions of the royal society of london.(a.)* 186 (1895), pp. 123–164. DOI: https://doi.org/10.1098/rsta.1895.0004.

[51] C. Rutland. “Large-eddy simulations for internal combustion engines–a review”. In: *International Journal of Engine Research* 12.5 (2011), pp. 421–451. DOI: https://doi.org/10.1177/1468087411407248.

[52] S. Šarić and B. Basara. “A near-wall model for heat transfer at high Prandtl numbers”. In: *at 10th Int. Conference on CFD (ICCFD10), Barcelona, Spain*. 2018.

[53] M. Schäfer. *Computational engineering: Introduction to numerical methods*. Vol. 321. Springer, 2006. DOI: https://doi.org/10.1007/3-540-30686-2.

[54] M. Schmitt, C. E. Frouzakis, Y. M. Wright, A. Tomboulides, and K. Boulouchos. “Direct numerical simulation of the compression stroke under engine relevant conditions: Local wall heat flux distribution”. In: *International Journal of Heat and Mass Transfer* 92 (2016), pp. 718–731. DOI: https://doi.org/10.1016/j.ijheatmasstransfer.2015.08.074.

[55] M. Schmitt, C. E. Frouzakis, Y. M. Wright, A. G. Tomboulides, and K. Boulouchos. “Direct numerical simulation of the compression stroke under engine-relevant conditions: Evolution of the velocity and thermal boundary layers”. In: *International Journal of Heat and Mass Transfer* 91 (2015), pp. 948–960. DOI: https://doi.org/10.1016/j.ijheatmasstransfer.2015.08.031.

[56] F. Secchi, D. Gatti, and B. Frohnapfel. “The Wall-Jet Region of a Turbulent Jet Impinging on Smooth and Rough Plates”. In: *Flow, Turbulence and Combustion* 110.2 (2023), pp. 275–299. DOI: https://doi.org/10.1007/s10494-022-00387-x.

[57] F. Secchi, T. Häber, D. Gatti, S. Schulz, D. Trimis, R. Suntz, and B. Frohnapfel. "Turbulent impinging jets on rough surfaces". In: *GAMM-Mitteilungen* 45.1 (2022), e202200005. DOI: https://doi.org/10.1002/gamm.202200005.

[58] C. G. Speziale. "Turbulence modeling for time-dependent RANS and VLES: a review". In: *AIAA journal* 36.2 (1998), pp. 173–184. DOI: https://doi.org/10.2514/6.1997-2051.

[59] J. H. Spurk and N. Aksel. *Strömungslehre*. Vol. 4. Springer, 1989. DOI: https://doi.org/10.1007/978-3-662-10098-1.

[60] K. Stephan and F. Mayinger. *Thermodynamik: Band 1: Einstoffsysteme. Grundlagen und technische Anwendungen*. Springer-Verlag, 2013.

[61] R. Stone. *Introduction to internal combustion engines*. Vol. 3. Springer, 1999.

[62] K. Suga, M. Nagaoka, and N. Horinouchi. "Application of a higher order GGDH heat flux model to three-dimensional turbulent U-bend duct heat transfer". In: *J. Heat Transfer* 125.1 (2003), pp. 200–203. DOI: https://doi.org/10.1115/1.1532018.

[63] K. Suga. "Improvement of second moment closure for turbulent obstacle flow and heat transfer". In: *International journal of heat and fluid flow* 25.5 (2004), pp. 776–784. DOI: https://doi.org/10.1016/j.ijheatfluidflow.2004.03.007.

[64] K. Suga. "Predicting turbulence and heat transfer in 3-D curved ducts by near-wall second moment closures". In: *International Journal of Heat and Mass Transfer* 46.1 (2003), pp. 161–173. DOI: https://doi.org/10.1016/s0017-9310(02)00249-1.

[65] B. Vreman, B. Geurts, and H. Kuerten. "Large-eddy simulation of the turbulent mixing layer". In: *Journal of fluid mechanics* 339 (1997), pp. 357–390. DOI: https://doi.org/10.3990/1.9789090088846.

[66] S. Wegt. "Computational characterization of flow and turbulence in IC engine-relevant cooling channels: An LES-and Reynolds-stress-modeling study". In: (2022).

[67] B. A. Younis, C. G. Speziale, and T. T. Clark. "A rational model for the turbulent scalar fluxes". In: *Proceedings of the Royal Society A: Mathematical, Physical and Engineering Sciences* 461.2054 (2005), pp. 575–594. DOI: https://doi.org/10.1098/rspa.2004.1380.

A. Appendix

A.1. Reynolds stress model

Transport equation for the Reynolds stress tensor $\overline{u_i' u_j'}$:

$$\frac{D\overline{u_i' u_j'}}{Dt} = \frac{\partial}{\partial x_k}\left[\left(\frac{1}{2}\nu + \frac{\nu_t}{\sigma_{\overline{u_i' u_j'}}}\right)\frac{\partial \overline{u_i' u_j'}}{\partial x_k}\right] - \left(\overline{u_i' u_k'}\frac{\partial \overline{u_j}}{\partial x_k} - \overline{u_j' u_k'}\frac{\partial \overline{u_i}}{\partial x_k}\right) - \epsilon_{ij}^h + \Phi_{ij} + \Phi_{ij}^w \tag{A.1}$$

Modelling of the homogeneous dissipation rate ϵ_{ij}^h in transport equation of Reynolds Stress:

$$\epsilon_{ij}^h = \epsilon^h\left[(1-f_s)\frac{2}{3}\delta_{ij} + \frac{\overline{u_i' u_j'}}{k} f_s\right] \qquad \text{with} \qquad f_s = 1 - E^2\sqrt{A} \qquad \text{and} \qquad \epsilon^h = \omega^h k \tag{A.2}$$

Modelling of the redistribution term Φ_{ij} in the transport equation of the Reynolds Stress:

$$\begin{aligned}\Phi_{ij} = -\epsilon^h C_1 a_{ij} + C_3 k S_{ij} + C_4 k\left(a_{ip}S_{pj} + a_{jp}S_{pi} - \frac{2}{3}a_{pq}S_{pq}\delta_{ij}\right) \\ - C_5 k\left(a_{ip}W_{jp} + a_{jp}W_{ip}\right)\end{aligned} \tag{A.3}$$

Representation of the Reynolds stress a_{ij} and dissipation anisotropy tensor e_{ij} from the modelling of the redistribution term Φ_{ij}:

$$A = 1 - \frac{9}{8}\left(A_2 - A_3\right) \tag{A.4}$$

$$\text{with} \qquad A_2 = a_{ij}a_{ji} \qquad \text{and} \qquad A_3 = a_{ij}a_{jk}a_{ki} \qquad \text{and} \qquad a_{ij} = \frac{\overline{u_i' u_j'}}{k} - \frac{2}{3}\delta_{ij} \tag{A.5}$$

$$E = 1 - \frac{9}{8}\left(E_2 - E_3\right) \tag{A.6}$$

$$\text{with} \qquad E_2 = e_{ij}e_{ji} \qquad \text{and} \qquad E_3 = e_{ij}e_{jk}e_{ki} \qquad \text{and} \qquad e_{ij} = \frac{\epsilon_{ij}^h}{\epsilon^h} - \frac{2}{3}\delta_{ij} \tag{A.7}$$

Modelling of the wall reflection term Φ_{ij}^w in transport equation of Reynolds Stress:

$$\begin{aligned}\Phi_{ij}^h = C_1^w f_w \frac{\epsilon^h}{k}\left(\overline{u_k' u_m'} n_k n_m \delta_{ij} - \frac{3}{2}\overline{u_i' u_k'} n_k n_j - \frac{3}{2}\overline{u_k' u_j'} n_k n_i\right) \\ + C_2^w f_w \left(\Phi_{km,2}^{IP} n_k n_m \delta_{ij} - \frac{3}{2}\Phi_{ik,2}^{IP} n_k n_j - \frac{3}{2}\Phi_{kj,2}^{IP} n_k n_i\right)\end{aligned} \tag{A.8}$$

$$\text{with} \qquad \Phi_{ij,2}^{IP} = -C_2\left(P_{ij} - \frac{2}{3\delta_{ij}P_k}\right) \tag{A.9}$$

$$\text{with} \qquad S_{ij} = \frac{1}{2}\left(\frac{\partial \overline{u_i}}{\partial x_j} + \frac{\partial \overline{u_j}}{\partial x_i}\right) \tag{A.10}$$

$$\text{with} \qquad W_{ij} = \frac{1}{2}\left(\frac{\partial \overline{u_i}}{\partial x_j} - \frac{\overline{u_j}}{\partial x_i}\right) \tag{A.11}$$

Transport equation of the homogenius, specific dissipation rate ω^h:

$$\begin{aligned}\frac{D\omega^h}{Dt} = \frac{\partial}{\partial x_k}\left[\left(\frac{1}{2}\nu + \frac{\nu_t}{\sigma_\omega}\right)\frac{\partial \omega^h}{\partial x_k}\right] + C_{\omega,1}\frac{\omega^h}{k}P_k - C_{\omega,2}\left(\omega^h\right)^2 + \\ \frac{2}{k}\left(C_{cr,1}\frac{1}{2}\nu + C_{cr,2}\frac{\nu_t}{\sigma_\omega}\right)\frac{\partial \omega^h}{\partial x_k}\frac{\partial k}{\partial x_k} + \frac{2}{k}C_{\omega,3}\nu\nu_t\frac{\partial^2 U_i}{\partial x_j \partial x_l}\frac{\partial^2 U_i}{\partial x_j \partial x_l} + S_l\end{aligned} \tag{A.12}$$

Production of the kinetic turbulent energy k in transport equation of the homoopposite, specific dissipation rate:

$$P_k = -\overline{u_i' u_j'}\frac{\partial \overline{u_i}}{\partial x_j} \tag{A.13}$$

Modelling of the turbulent viscosity transport equation in the homo counter, specific dissipation rate:

$$\nu_t = 0.144 A k^{1/2} \max\left[10\left(\frac{\nu^3}{k\omega^h}\right)^{1/4}, \frac{k^{1/2}}{\omega^h}\right] \tag{A.14}$$

Length scale correction term S_l:

$$S_l = max\left\{\left[\left(\frac{1}{C_l}\frac{\partial L}{\partial x_n}\right)^2 - 1\right]\left(\frac{1}{C_l}\frac{\partial L}{\partial x_n}\right)^2, 0\right\} A\omega^h\omega^h \tag{A.15}$$

Model functions, coefficients and constants:

$$\begin{gathered} C_1 = 2.5AF^{1/4}f + \sqrt{A}E^2, \qquad C_2 = 0.8A^{1/2}, \\ C_3 = \frac{4}{3}C_2, \qquad C_4 = C_2, \qquad C_5 = C_2 \end{gathered} \tag{A.16}$$

$$F = \min\left[0.6, A_2\right], \qquad f = \min\left[\left(\frac{Re_t}{150}\right)^{3/2}, 1\right], \qquad Re_t = \frac{k^2}{\nu\epsilon^h} \tag{A.17}$$

$$C_1^w = \max\left[1.0 - 1.75AF^{1/4}f, 0.3\right], \qquad C_2^w = \min\left[A, 0.3\right] \tag{A.18}$$

$$f_w = \max\left[\frac{k^{3/2}}{C_l\epsilon^h x_n}, 1.4\right], \qquad C_l = 2.5 \tag{A.19}$$

$$C_{\omega,1} = 0.44, \qquad C_{\omega,2} = 0.8, \qquad C_{\omega,3} = 1.0, \sigma_\omega = 1.1, \sigma_{\overline{u_i' u_j'}} = 1.1 \tag{A.20}$$

A.2. Improved-Instability-Sensitive-Reynolds stress model

The equations required to describe the IISRSM are largely identical. In the following, only the deviating modelling approaches are listed.

The transport equation of the specific, homogeneous dissipation rate ω^h:

$$\left(\frac{D\omega^h}{Dt}\right)_{\text{IISRSM}} = \left(\frac{D\omega^h}{Dt}\right)_{\text{RSM}} + P_{\text{IISRSM}} \tag{A.21}$$

Additional production term P_{IISRSM}:

$$P_{\text{ISRSM}} = 0.12\ max\left[1.755\kappa|\frac{\partial^2\overline{U_i}}{\partial x_j^2}|\sqrt{k} - T_2,\ 0\right] \tag{A.22}$$

$$\text{with} \qquad T_2 = 3kmax\left[\frac{1}{k^2}\frac{\partial k}{\partial x_j}\frac{\partial k}{\partial x_j}, \frac{1}{\omega^h\omega^h}\frac{\partial\omega^h}{\partial x_j}\frac{\partial\omega^h}{\partial x_j}\right] \tag{A.23}$$

Personal information

Name:	Maximilian Christof Bopp
Date of birth:	20.09.1991

Education

02/2019 - 07/2023	PhD student, TU Darmstadt, Institute for Fluid Mechanics and Aerodynamics, Modelling and Simulation of Turbulent Flows
10/2015 - 10/2018	Master of Science, TU Darmstadt, Mechanical Engineering
10/2011 - 10/2015	Bachelor of Science, TU Darmstadt, Mechanical Engineering

Professional experience

02/2019 - 07/2023	Research Assistant, TU Darmstadt, Institute of Fluid Mechanics and Aerodynamics, Modelling and Simulation of Turbulent Flows

List of Figures

2.1. Schematic illustration of the turbulence energy spectrum and eddy decay with the eddy energy $E(\kappa)$ plotted over the eddy wavenumber κ. 12
2.2. Schematic illustration of a generic two-dimensional finite volume grid with homogeneous control volume (CV) arrangement. 27

3.1. Anisotropy-Invariant Map (AIM) for the invariant-related functional relationships $\mathrm{II_a}$ and $\mathrm{III_a}$ of the Reynolds stress anisotropy tensor a_{ij}, as proposed by Lumley and Newman (1977). 33
3.2. Wall-normal evolution of the invariant tuples ($\mathrm{II_a}$, $\mathrm{III_a}$) and (ξ, η) of the Reynolds stress anisotropy tensor a_{ij} for a fully developed channel flow at a friction Reynolds number $Re_\tau = 180$, obtained by a DNS of Moser, Kim, and Mansour (1999). 34
3.3. Wall-normal evolution of the eigenvalue (λ_1, λ_2) and barycentric tuples (x_B, y_B) of the Reynolds stress anisotopy tensor a_{ij} for a fully developed channel flow at a friction Reynolds number $Re_\tau = 180$, obtained by a DNS of Moser, Kim, and Mansour (1999). 36
3.4. Barycentric color map for the standard Red-Green-Blue (RGB) color model (left) and for the adapted Cyan-Magenta-Yellow-Black (CMYK) color model (right). 38
3.5. Barycentric color map for the adjusted RGB (left) and CMYK color model (right) with modified barycentric weights $C^*_{ic} = (C_{ic}+C_{off})^{C_{exp}}$. 39

4.1. Schematic representation of the solution domain considered for the fully-developed channel flow at a friction Reynolds number of $\mathrm{Re}_\tau = 180$. 42
4.2. Instantaneous velocity and temperature fields in a fully developed turbulent channel flow at a friction Reynolds number $\mathrm{Re}_\tau = 180$ with fixed iso-flux temperature boundary condition, obtained by the scale resolving IISRSM. 43
4.3. Mean velocity (left) and Reynolds-stress component profiles (right) of the fully-developed channel flow of Horiuti (1992) and Kasagi, Tomita, and Kuroda (1992). 44

4.4. Turbulent anisotropy trajectories calculated form the Reynolds-stress tensor fields of the IISRSM (△), RSM (△) and reference DNS (□) of Horiuti (1992) and Kasagi, Tomita, and Kuroda (1992), displayed in a nonlinear $\xi\eta$-based anisotropy invariant map (left) and a corresponding barycentric map (right). 45

4.5. Comparison of the dimensionless mean temperature profiles $\overline{\Theta}^{+}$ across the half channel height for the RSM (left), IISRSM(right) against the DNS of Horiuti (1992) and Kasagi, Tomita, and Kuroda (1992) and the theoretical temperature evolution $\overline{\Theta}^{+}_{Theory} = Pry^{+}$, $2.78\ln y^{+} + C^{+}_{\theta}$. 46

4.6. Schematic representation of the solution domain for the slot-jet impingement configuration with an inflow Reynolds number of $\mathrm{Re_b} = 10000$ and a heated bottom wall according to Hattori and Nagano (2004). 47

4.7. Flow visualization by the Q-criterion, colored by the non-dimensionalized instantaneous temperature field ($\Theta/\Theta_{\mathrm{max}}$) obtained by the IISRSM in slot-jet impingement configuration at a nozzle-height of H/D = 2.0 with constant temperature gradient at the wall. 49

4.8. Iso-contours of the instantaneous velocity field, colored by its magnitude, and corresponding mean streamlines obtained by the baseline RSM (left) and the scale-resolving IISRSM (right) at three nozzle-to-wall distances $H/D = 0.5$, $H/D = 1.0$, $H/D = 2.0$. 50

4.9. Profile development of the mean axial flow velocity in x direction in the slot-jet impingement configuration for all three nozzle-to-plate distances $H/D = 0.5, 1.0, 2.0$. 52

4.10. Distribution of surface friction coefficient at lower wall C_f determined by RSM and IISRSM compared to DNS data for all three nozzle-to-plate distances $H/D = 0.5, 1.0, 2.0$. 53

4.11. Profile development of the streamwise ($\sqrt{\overline{u'u'}}/U_\tau$) Reynolds stress intensity in the slot-jet impingement configuration for all three nozzle-to-plate distances $H/D = 0.5, 1.0, 2.0$. 54

4.12. Profile development of the normal-to-wall ($\sqrt{\overline{v'v'}}/U_\tau$) Reynolds stress intensity in the slot-jet impingement configuration for all three nozzle-to-plate distances $H/D = 0.5, 1.0, 2.0, 3.0, 4.0$. 55

4.13. Profile development of the temperature $\overline{\Theta}$ in x direction in the slot-jet impingement configuration obtained by the steady RSM for all three nozzle-to-plate distances $H/D = 0.5, 1.0$ and 2.0. 57

4.14. Profile development of the temperature $\overline{\Theta}$ in x direction in the slot-jet impingement configuration obtained by the scale resolving IISRSM for all three nozzle-to-plate distances $H/D = 0.5, 1.0$ and 2.0. 58

4.15. Distribution of the Nusselt number Nu at the bottom impingement wall for the nozzle-to-plate distance $H/D = 0.5$ for the single-slot-jet impingement configuration at a bulk Reynolds number of $\mathrm{Re_b} = 10000$. 59

4.16. Distribution of the Nusselt number Nu at the bottom impingement wall for the nozzle-to-plate distance $H/D = 1.0$ for the single-slot-jet impingement configuration at a bulk Reynolds number of $\mathrm{Re_b} = 10000$. 60

4.17. Distribution of the Nusselt number Nu at the bottom impingement wall for the nozzle-to-plate distance $H/D = 2.0$ for the single-slot-jet impingement configuration at a bulk Reynolds number of $\mathrm{Re_b} = 10000$. 61

5.1. Stereolithography of the considered TU Da Flowbench configuration for the reference experimental investigation of Freudenhammer, Baum, Peterson, Böhm, Jung, and Grundmann (2014) and all numerical LES- and scale resolving RANS-based computational simulations. 64

5.2. Preprocessed 8 million cells finite-volume mesh of the considered TUDa Flowbench configuration for the numerical LES- and scale resolving RANS-based computational simulations. 65

5.3. Comparison of the computational grid around the inlet valve for the IISRSM (a) 2.3m cells & (b) 4m cells as well as for the reference LES (a) calculations. 66

5.4. Kolmogorov Scale LES Quality Index field LES_IQ$_\eta$ withing the valve plane (left), the vertical and horizontal and collision plane (middle & right) of the TUDa Flowbench configuration for the corresponding reference LES at its 8 million finite volume cells mesh. 68

5.5. Ratio between the modeled and total turbulence kinetic energy $k_{\mathrm{mod}}/k_{\mathrm{total}}$ for the scale-resolving, RANS-RSM-related IISRSM simulations on the underlying 2.3 and 4 million cells finite volume meshes. 69

5.6. Instantaneous velocity field on the valve plane of the TUDa Flowbench configuration obtained by the scale-resolving IISRSM on the corresponding 4 million cells finite volume mesh. 70

5.7. Instantaneous, time-resolved velocity field on the valve plane of the TUDa Flowbench configuration obtained by the scale-resolving IISRSM and LES on the corresponding 2.3, 4 and 8 million cells finite volume mesh. 70

5.8. Time-averaged velocity field on the valve plane of the TUDa Flowbench configuration obtained by the scale-resolving IISRSM and LES on the corresponding 2.3, 4 and 8 million cells finite volume mesh in comparison with the experimentally obtained MRV velocity field. 71
5.9. Mean velocity field on the valve curtain obtained by the MRV, LES and scale-resolving IISRSM. 72
5.10. Time-averaged profiles of the velocity components U_x and U_y parallel to the x and z axis at the absolute position of 10 mm below the valve indicated by the white dashed line in Fig. 5.6, evaluated along the red marked lines 1 and 2. 73
5.11. Total turbulence kinetic energy k_{tot} normalized by the bulk inlet velocity $\mathrm{U_b}$ for the LES and IISRSM simulations within the valve plane of the TUDa Flowbench configuration. 74
5.12. Comparative assesment of the time-averaged two componentality parameter $A = 1 - 9/8(A_2 - A_3)$ within the valve plane of the TUDa Flowbench configuration obtained by the LES and scale-resolving IISRSM. 75
5.13. LES- (left) and the IISRSM-related cell coloring of the time-averaged barycentric coloring for the corresponding 4m (middle) and 2.3m (right) cells finite volume meshes in the valve plane of the TUDa Flowbench configuration. 75
5.14. Full rendering (left) of the TUDa Flowbench, its collision plane (bottom right) and its top plane (top right) colored by the time-resolved, fluctuating, instantaneous velocity field of the reference LES. 77
5.15. Schematic representation of the solution domain for the round-jet impingement at a bulk Reynolds number $Re_{\mathrm{b}} = 10000$ onto a heated wall with a nozzle-plate distance of H/D = 2. 79
5.16. Flow visualization by the Q-criterion, colored by the non-dimensionalized instantaneous temperature field ($\overline{\Theta}/\overline{\Theta}_{\mathrm{max}}$) obtained by the IISRSM in a round impinging jet with fixed wall temperature. 80
5.17. Time-averaged DNS- (top) and RANS-RSM-related (middle) isocontours and instantaneous IISRSM-related (bottom) velocity fields with their respective corresponding mean streamlines (right) and the corresponding time-averaged turbulence kinetic energy (left) in the central $(r - z)$ vertical plane of the round-jet impingement configuration. 81
5.18. Profile development of the horizontal velocity component (U_r/U_b) in the radial direction in the round-jet impingement configuration. 82
5.19. Profile development of the turbulence kinetic energy (k/U_b^2) in the radial direction in the round-jet impingement configuration. 83

5.20. Profile development of the radial ($\overline{u\prime_r u\prime_r}$) and shear ($\overline{u\prime_r u\prime_z}$) Reynolds stress components in the radial direction in the round-jet impingement configuration. 84
5.21. Profile development of the wall-normal ($\overline{u\prime_z u\prime_z}$) Reynolds stress component in the radial direction in the round-jet impingement configuration. 85
5.22. Comparative assessment of the anisotropy tensors second and third invariant ($\mathrm{II_a}$ & $\mathrm{III_a}$) for every data point of the computational axisymmetric impinging jet configuration domain obtained by the reference DNS, scale-resolving IISRSM and baseline RSM. 86
5.23. Comparative assessment of the barycentric coordinated $x_B(a_{ij})$ and $y_B(a_{ij})$ for every data point of the computational axisymmetric impinging jet configuration domain obtained by the reference DNS, scale-resolving IISRSM and baseline RSM. 86
5.24. DNS- (top) and RANS-RSM-related (middle) and IISRSM-related (bottom) iso-contours of the time-averaged two componentality parameter A (left) and time averaged barycentric coloring (right) in the central ($r-z$) vertical plane in the round-jet impingement configuration. 87
5.25. Profile evolution of the 1-A (two-componantality parameter) in different radial positions $r/D = 0.5$, 1.0, 2.0, 3.0 and 4.0 within the r-z-plane of the round-jet impingement configuration. 89
5.26. Trajectory evolution of the barycentric coordinates obtained by the reference DNS, IISRSM and RSM at the radial positions $r/D = 0.5$, 1.0, 2.0, 3.0 and 4.0 within the r-z-plane of the round-jet impingement configuration. 90
5.27. Friction coefficient C_f (left) and Nusselt number distribution (right) at the impingement wall over the dimensionless radius r/D within the r-z-plane of the round-jet impingement configuration. 91
5.28. Profile development of the temperature $\overline{\Theta}$ non-dimensionalized by the inlet and wall temperature $\overline{\Theta}_{\mathrm{inlet}}$ and $\overline{\Theta}_{\mathrm{wall}}$ in radial direction of the round-jet impingement configuration. 92
5.29. Schematic drawing of the solution domain for the double slot impingement configuration with species transfer at a bulk Reynolds number of $Re_b = 10000$. 94
5.30. Flow visualization by the Q-criterion, colored by the non-dimensionalized instantaneous velocity ($U/\overline{U}_b$), pressure (p/p_{inlet}) and species field ($C/\overline{C}_1$) obtained by the IISRSM in a double slot impingement configuration. 98
5.31. Instantaneous and mean velocity fields normalized by the bulk velocity $\mathrm{U_b}$ with its corresponding stream lines obtained by the IISRSM for the present double-slot impingement configuration. . . 99

5.32. Mean velocity field ($U/\overline{U}_b$) around the stagnation point $-1 \leq x/D \leq 1$ and $0 \leq y/D \leq 2$ of the double slot-jet impingement configuration obtained by LES, IISRSM and RSM. 100
5.33. Mean turbulence kinetic energy ($k/\overline{U}_b^2$) around the stagnation point $-1 \leq x/D \leq 1$ and $0 \leq y/D \leq 2$ of the double slot-jet impingement configuration obtained by LES, IISRSM and RSM. 101
5.34. Vertical, wall-normal profile development of the mean velocity magnitude $\overline{U}$, the wall normal Reynolds stress component $\overline{u\prime u\prime}$ and the wall parallel Reynolds stress component $\overline{v\prime v\prime}$ normalized by the mean bulk velocity U_b of the the double-slot-jet impingement configuration at $-1 \leq x/D \leq 1$ and $0 \leq y/D \leq 2$. 102
5.35. Point cloud of the barycentric coordinates ($x_B(a_{ij})$, $y_B(a_{ij})$) at $-1 \leq x/D \leq 1$ and $0 \leq y/D \leq 2$ obtained by the LES, scale-resolving IISRSM and baseline RSM for the double slot-jet impingement configuration. 104
5.36. Coloring of the barycentric coordinates $x_B(a_{ij})$ and $y_B(a_{ij})$ for every data point ($-1 \leq x/D \leq 1$ and $0 \leq y/D \leq 2$) of the computational double-slot impinging jet configuration domain obtained by the LES, scale-resolving IISRSM and baseline RSM. 105
5.37. Trajectories of the barycentric coordinates ($x_B(a_{ij})$, $y_B(a_{ij})$) at $z/D = 2.0, 1.5, 1.0, 0.5$ obtained by the LES, scale-resolving IISRSM and baseline RSM for the double slot-jet impingement configuration at $0 \leq x/D \leq 1$. 106
5.38. Mean species field ($\overline{C}/\overline{C}_1$) around the stagnation point $-1 \leq x/D \leq 1$ and $0 \leq y/D \leq 2$ of the double slot-jet impingement configuration obtained by LES, IISRSM and RSM in conjunction with the simple gradient diffusion hypothesis (Sec. 2.4.3) for the modeling of the turbulent species flux $\overline{u\prime_i \theta\prime}$. 107
5.39. Mean species concentration $\overline{C}/\overline{C}_1$ in x-direction ($0 \leq x/D \leq 1$) at four characteristic distances to the inlet nozzles ($y/D = 2.0$, 1.5, 1.0, 0.5), obtained by LES, IISRSM and RSM in conjunction with the SGDH, GGDH and HOGGDH species flux modeling approach for the double slot-jet impingement configuration. 108

List of Tables

2.1. Model coefficients for an appropriate weighting of the contributing, respective heat fluxes, determined by Younis, Speziale, and Clark (2005) & Kaltenbach, Gerz, and Schumann (1994) 23

3.1. Limiting states and boundaries of the η, ξ- and eigenvalue-related turbulence anisotropy map, suggested by Lumley (1979). 35

4.1. Arrangement of numerical cells and dimensions of the solution area for three nozzle-to-plate distances for the calculations with the conventional RSM. 48
4.2. Arrangement of numerical cells and dimensions of the solution area for three nozzle-to-plate distances for the simulations with the IISRSM. 48

5.1. Dimensions, segmentation, numerical cells and resulting mesh size for the solution domain of the RSM, IISRSM and LES for the DSIJ configuration. 95

Nomenclature

Acronyms

AIM	Anisotropy Invariant Map
ANSA	Automatic Net generation for Structural Analysis
ASIJ	Axisymmetric Impining Jet
BS	Bassam Speciale - Diffusion Hypothesis
bTDC	Before The Dead Center
CA	Crank Angle
CFD	Computational Fluid Dynamics
CMYK	Cyan-Magenta-Yellow-Black Color Schmeme
CV	Control Volume
DNS	Direct Numerical Simulation
DSIJ	Double Square Impining Jet
FVM	Finite Volume Method
GGDH	Generalized Gradient Diffusion Hypothesis
HOGGDH	Higher Order Gradient Diffusion Hypothesis
IC	Internal Combustion
IISRSM	Improved Instability Reynolds Stress Model
LES	Large Eddy Simulation
NSE	Navier-Stokes Equations
RANS	Reynolds-Averaged Navier Stokes methodology
RGB	Red-Green-Blue Color Scheme

RSM	Reynolds Stress Model	
SAS	Scale-Adaptive Simulation	
SGDH	Simple Gradient Diffusion Hypothesis	
SGS	Subgrid-Scale	
SLA	Institut for Fluid Mechanics and Aerodynamics	
SMC	Second-Moment Closure	
TUDa	Technical University of Darmstadt	

Greek letters

$(.)\prime$	Residual Operator	–
$(.)_W$	Wall Value	–
α	Convective heat transfer coefficient	$\mathrm{W\,m^{-2}\,K^{-1}}$
Δx^+,Δy^+,Δz^+	Grid Spacing in Wall Units	–
Δ	Grid Size	m
δ_{ij}	Kronecker Delta	–
ϵ^h_{ij}	Homogeneous Reynolds stress dissipation rate	$\mathrm{m^2\,s^{-2}}$
ϵ_{ij}	Reynolds stress dissipation rate	$\mathrm{m^2\,s^{-2}}$
Γ_Θ	Turbulent Diffusivity of a thermal field	$\mathrm{m^2\,s^{-1}}$
Γ_{C}	Turbulent Diffusivity of a species field	$\mathrm{m^2\,s^{-1}}$
κ	Wave Number	–
λ	Thermal conductivity of a fluid	$\mathrm{W\,m^{-1}\,K}$
ν	Kinematic viscosity	$\mathrm{m^2\,s^{-1}}$
ν_{SGS}	Subgrid-scale viscosity	$\mathrm{m^2\,s^{-1}}$
ν_{t}	Eddy viscosity	$\mathrm{m^2\,s^{-1}}$
Ω_{ij}	Rate of Vorticiy tensor	$\mathrm{m^{-1}}$
$\overline{(.)}$	Mean Operator	–
$\Phi^R_{\mathrm{ij},1}$	Slow term	$\mathrm{m^2\,s^{-2}}$

$\Phi^R_{ij,2}$	Rapid term	$m^2\,s^{-2}$
$\Phi^R_{ij,3}$	Volume-related Reynolds stress Redistribution	$m^2\,s^{-2}$
Φ^R_{ij}	Reynolds Stress Redistribution	$m^2\,s^{-2}$
Φ^w_{ij}	wall reflection term	$m^2\,s^{-2}$
Φ_{ij}	Arbitrary physical Quantity	–
τ_{SGS}	Subgrid-scale stress tensor	$N\,m^{-2}$
τ_{ij}	Stress tensor	$N\,m^{-2}$
Θ	Temperature	K
$\tilde{\Omega}_{ij}$	Filtered Rate of Vorticity tensor	m^{-1}
$\tilde{(.)}$	Filtering Operator	–
$\xi - \eta$	Modified Invariants of a_{ij}	–
f_s	Weighting function	–

Latin letters

$\dot{m}$	Mass flux	–
$\dot{q}$	Heat Flux Density	$W\,m^2$
$\mathcal{L}$	Characteristic Length	m
$\mathcal{U}$	Characteristic Velocity	$m\,s^{-1}$
I_a ,II_a, III_a	Reynolds Stress Anisotropy Tensor invariants	–
Pr_t	Turbulent Prandtl Numberumber	–
$\overline{I}_i$	Reynolds-averaged Momentum balance	–
$\overline{u\prime_i\theta\prime}$	Turbulent Heat Flux	$m\,K\,s^{-1}$
$\overline{u\prime_i c\prime}$	Turbulent Species Flux	$kg\,m^{-2}\,s^{-1}$
$\overline{u\prime_i u\prime_j}$	Reynolds Stress Tensor	$m^2\,s^{-2}$
a_{ij}	Reynolds Stress Anisotropy tensor	–
$a_{P,N,E,S,W}$	Finite Volume Prefactors	–
C^*_{ic}	Modified Barycentric Weights	–

$C_{\mathrm{SGS},1}$	SAS constant 1	–
$C_{\mathrm{SGS},2}$	SAS constant 2	–
$C_{\mathrm{w},1}$	Production constant of specific homogeneous dissipation rate	–
$C_{\mathrm{w},2}$	Dissipation constant of specific homogeneous dissipation rate	–
$C_{\mathrm{w},2}$	Gradient production constant of specific homogeneous dissipation rate	–
c_p	Specific Heat at Constant Pressure	$\mathrm{J\,kg^{-1}\,K}$
C_W	WALE Constant	–
$C_{\Theta i}$	Turbulent Heat Flux Modeling Constant	–
C_{exp}	Exponential Barycentric Weights Modification Coefficient	–
C_f	Friction Coefficient	–
C_{ic}	Barycentric Weights	–
C_{off}	Linear Barycentric Weights Modification Coefficient	–
C_s	Smagorinsky constant	–
D	Diameter	m
D^{ν}_{ij}	Molecular Diffusion of Reynolds Stress	$\mathrm{m^2\,s^{-2}}$
D^{p}_{ij}	Pressure Diffusion of Reynolds Stress	$\mathrm{m^2\,s^{-2}}$
D^{t}_{ij}	Turbulent Diffusion of Reynolds Stress	$\mathrm{m^2\,s^{-2}}$
D_{Θ}	Thermal Diffusion Coefficient	$\mathrm{m^2\,s^{-1}}$
D_{C}	Species Diffusion Coefficient	$\mathrm{m^2\,s^{-1}}$
D_{ij}	Reynolds Stress Diffusion	$\mathrm{m^2\,s^{-2}}$
$E(\kappa)$	Energy of turbulent eddies with wavenumber	$\mathrm{m^2\,s^{-2}}$
G_{ij}	Reynolds Stress Production from fluctuating Volume Forces	$\mathrm{m^2\,s^{-2}}$
H	Domain Height	m
I_{i}	Momentum balance	–
k	Turbulence Kinetic Energy	$\mathrm{m^2\,s^{-2}}$
k_{mod}	Modeled Turbulent Kinetic Energy	$\mathrm{m^2\,s^{-2}}$

k_{res}	Resolved Turbulent Kinetic Energy	$\mathrm{m^2\,s^{-2}}$
k_{total}	Total Turbulent Kinetic Energy	$\mathrm{m^2\,s^{-2}}$
$L_{x,y,z}$	Domain Length	m
n	Northern Finite Volume cell midpoint	–
n_{c}	Normal vectors (Finite Volume cell)	–
n_{i}	Normal vectors (Wall normal)	–
$N_{x,y,z}$	Node Number	–
P_{ij}	Reynolds Stress Production from Mean Flow Deformation	$\mathrm{m^2\,s^{-2}}$
R_{ij}	Reynolds Stress Production from Rotation	$\mathrm{m^2\,s^{-2}}$
Re_τ	Friction Reynolds Number	–
Re_b	Bulk Reynolds Number	–
S_{ij}	Strain Rate Tensor	$\mathrm{s^{-1}}$
t	Time	s
U_τ	Friction Velocity	–
U_b	Bulk Velocity	–
x_B, y_B	Barycentric Coordinates	–
x_i	Cartesian Coordinates	m
X_{ic}	Limiting States of the Barycentric Triangle	–
y^+	Dimensionless Wall Wistance	–
1-C	One componental	–
2-C	One componental	–
3-C	One componental	–
N,E,S,W	North, East, South, West Computational Note	–
Nu	Nusselt number	–
Pr	Prandtl number	–
Re	Reynolds number	–
Sc	Schmidt number	–